The Dissertation Committee for Son Thanh Hoang Certifies that this is the approved version of the following dissertation:

Nanostructured Materials for Solar Energy Conversion

Committee:

Charles Buddie Mullins, Supervisor

Allen J. Bard

Brian A. Korgel

Gyeong S. Hwang

Keith J. Stevenson

Nanostructured Materials for Solar Energy Conversion

by

Son Thanh Hoang, B. Chemistry

Dissertation

Presented to the Faculty of the Graduate School of

The University of Texas at Austin

in Partial Fulfillment

of the Requirements

for the Degree of

Doctor of Philosophy

The University of Texas at Austin

May 2013

Dedication

To Thanh and my parents for their loving support

Acknowledgements

First, I would like to express my sincere appreciation to my advisor, Professor C. Buddie Mullins, for his guidance, encouragement, and patience over the last five years. I joined to Buddie's research group with very little experience. I have learned a lot from Buddie regarding work ethics, the design and maintenance of high quality instruments and experiments, and inspiration to become a better scientist, and for that I am thankful. I would like to thank Prof. Allen J. Bard for his invaluable comments and discussion.

I was also lucky to interact with a number of talented and friendly people in Buddie's group, especially photocatalyst subgroup. Sean Berglund has always been supportive, encouraging, and willing to listen when I have vented my frustration. Nathan Hahn made significant contributions to the work contained in chapter 2 and 3, and tolerated my 'silly' questions when I first switched to the new research area. I have always enjoyed talking with Hoang Dang, Alex Rettie, Will Chemelewski, Ting Yan, and Ming Pan. I also acknowledge several UT facility scientists and technical specialists, especially Danny, Butch Cunningham, Jim Smitherman, Dr. Dwight Romanovicz, and Dr. Hugo Celio, whose invaluable help with equipment fabrication and experimentation over the years made this work possible.

I would also like to express my gratitude to my friends outside of the lab who made my graduate school experience in the US memorable. I thank Hieu Le, Trang Dinh, Chi Hoang, Thong Ngo, Thuy Nguyen, Anh Nguyen, Khoa Do, and Tuyen Huynh for their friendship and encouragement.

Finally, I would like to express my deepest appreciation for Thanh, and my parents whose love, encouragement, and unfailing support made it possible to complete

my grad school. I would not have been able to accomplish what I have today without your unconditional support.

Nanostructured Materials for Solar Energy Conversion

Son Thanh Hoang, PhD

The University of Texas at Austin, 2013

Supervisor: Charles Buddie Mullins

The energy requirements of our planet will continue to grow with increasing world population and the modernization of currently underdeveloped countries. This will force us to search for environmental friendly alternative energy resources. Solar energy by far provides the largest of all renewable energy resources with an average power of 120 000 TW irradiated from the sun which can be exploited through solar electricity, solar fuel, and biomass. Nanostructured materials have been the subject of extensive research as the building block for construction of solar energy conversion devices for the past decades. The nanostructured materials sometimes have peculiar electrical and optical properties that are often shape and size dependent and are not expected in the bulk phase. Recent research has focused on new strategies to control nanostructured morphologies and compositions of semiconductor materials to optimize their solar conversion efficiency. In this dissertation, we discuss the synthesis and characterizations of one dimensional nanostructured TiO_2 based materials and their solar energy conversion applications.

We have developed a solvothermal synthesis method for growing densely packed, vertical, single crystalline TiO_2 rutile nanowire arrays with unprecedented small feature sizes of 5 nm and lengths up to 4.4 μm. Because of TiO_2's large band gap, the working spectrum of TiO_2 is limited to the ultra violet region with photons shorter than 420 nm.

We demonstrate that the active spectrum of TiO_2 can be shifted to ~ 520 nm with incorporation of N via nitridation of TiO_2 nanowires in NH_3 flow. In addition, we demonstrate a synergistic effect involving hydrogenation and nitridation cotreatment of TiO_2 nanowires that further redshift the active spectrum of TiO_2 to 570 nm. The Ta and N co-incorporated TiO_2 nanowires were also prepared and showed significant enhancement in photoelectrochemical performance compared to mono-incorporation of Ta or N. This enhancement is due to fewer recombination centers from charge compensation effects and suppression of the formation of an amorphous layer on the nanowires during the nitridation process. Finally, we have developed hydrothermal synthesis of single crystalline TiO_2 nanoplatelet arrays on virtually all substrates and demonstrated their applications in water photo-oxidation and dye sensitized solar cells.

Table of Contents

List of Tables

List of Figures

Chapter 1: Introduction

THE ENERGY CHALLENGE

The world energy demand continues to increase due to population growth and industrialization and modernization of the developing countries. The energy use in China was estimated to surpass in 2009 and is projected to be 68 % higher in 2035 than that for the United States (Figure 1.1).[1]

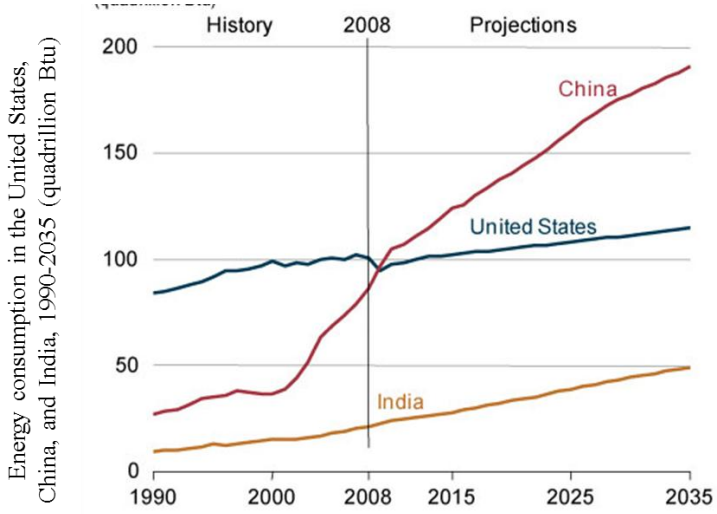

Figure 1.1. Energy consumption in the United States, China, and India, 1990-2035. [1]

In 2001, the global power consumption rate was 13 tetrawatts (TW), equivalent to 4.1 x 10^{20} joules/year of which 86% comes from fossil fuels.[2,3] The energy demand is projected to more than double (30 TW) by 2050 and more than triple (46 TW) by 2100.[3] In the short term, fossil fuels will still be extensively employed, but the production will attain the peak and decline eventually given a finite reserve.[4] In addition to the increase in the scarcity of fossil fuels, the geographical distribution of fossil fuel reserves has become more and more apparent in global politics since the largest oil reserves are

located in the politically unstable regions, such as the Middle East (Figure 1.2). Moreover, the over-consumption of fossil fuels leads to the emission of a number greenhouse gases and pollutants causing global climate changes. Finding alternative sustainable and environmental friendly energy resources to fill in the huge energy gap (17 TW by 2050 and 33 TW by 2100) is still the most daunting challenge for all human society.

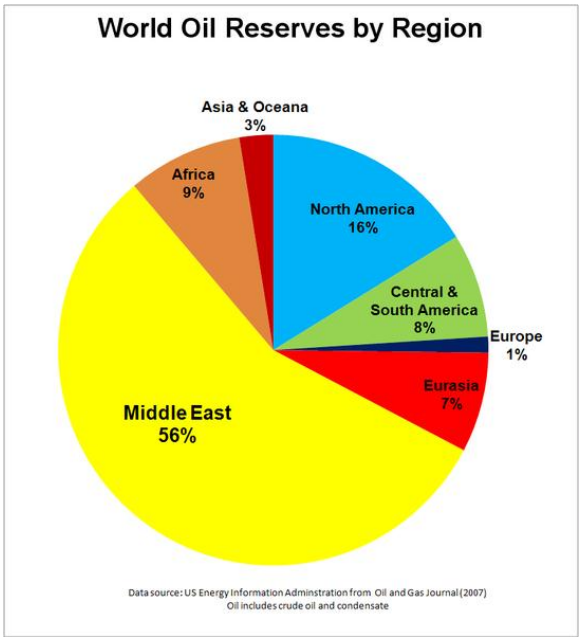

Figure 1.2. World oil proved reserves by region[5]

ALTERNATIVE ENERGY

In order to maintain our current lifestyle, it is obvious that we will need to seek environmentally friendly alternative energy resources to fill the energy gap. A number of options exist such as carbon neutral energy, nuclear power, and renewable energy. Carbon neutral energy refers to technology that employs fossil fuels in conjunction with carbon sequestration to achieve a net zero carbon footprint or zero carbon emissions. The

challenge now is not only doubling fossil fuel production (which is already at the peak) but also finding a secure storage for ~ 30 billion metric tons of CO_2 produced annually to obtain the additional 13 TW of energy. If nuclear power is entirely used to fill the energy gap, it will require construction of ~13,000 1 GW-electric nuclear power plans by 2050, i.e. it will require construction of a new nuclear power plan every day for the next 50 years.

The renewable energy resources include hydroelectric resources (0.5 TW), tides and ocean currents (2 TW), geothermal (12 TW), wind power (2-4 TW), and solar energy (120 000 TW) which can be exploited through solar electricity, solar fuel, and biomass. Clearly, the potential capacity of solar energy outperforms other options although the contribution of energy produced from solar to the total energy demand is still quite modest. Solar electricity contributes less than 0.1 % of the world electricity and biomass contributed less than 1.5 % of the world's energy.[3,4]

The sun irradiates the earth's surface with ~ 120 000 TW of power, i.e. more energy from the sunlight striking the earth in one hour than the global energy consumed in one year. It means that by covering 0.16 % of the earth surface with 10 % solar conversion efficiency devices, we could generate 20 TW to meet global demands for carbon-neutral energy in the second half of the 21st century.[3] The solar cell market is one of fastest growing markets with growing rate of 35-40 %. Providing a total capacity of 1200 MW reported for 2004, it would reach 20 TW in 2036 with a sustained 35 % annual growth rate.[6] In addition, solar energy is decentralized on a global scale, thus minimizing national security dependence.

Although solar energy is ideal to meet the projected demand, significant advances in science and technology are required to attain higher solar conversion efficiency and cheaper devices. Figure 1.3 shows the best solar cell (photovoltaic, PV) efficiency in

research. The multi-junction cells demonstrate the highest efficiency, the most dominant direct solar conversion technology, however, is still the single-crystal silicon based photovoltaic devices which are commercially available with a 15 % efficiency.[3] However, these devices suffer from high cost of manufacturing and installation. Therefore extensive research is needed to develop more cost-effective strategies to convert solar energy. Thin film technology using polycrystalline semiconductors such as $CuInGaSe_2$, CdTe, Si or amorphous Si-H can bring the cost down significantly due to smaller raw materials required for manufacturing. Dye sensitized solar cells have also gained considerable interest since their main compounds consisting of earth-abundant elements (TiO_2) which are necessary to enlarge installation scale to the TW-scale.

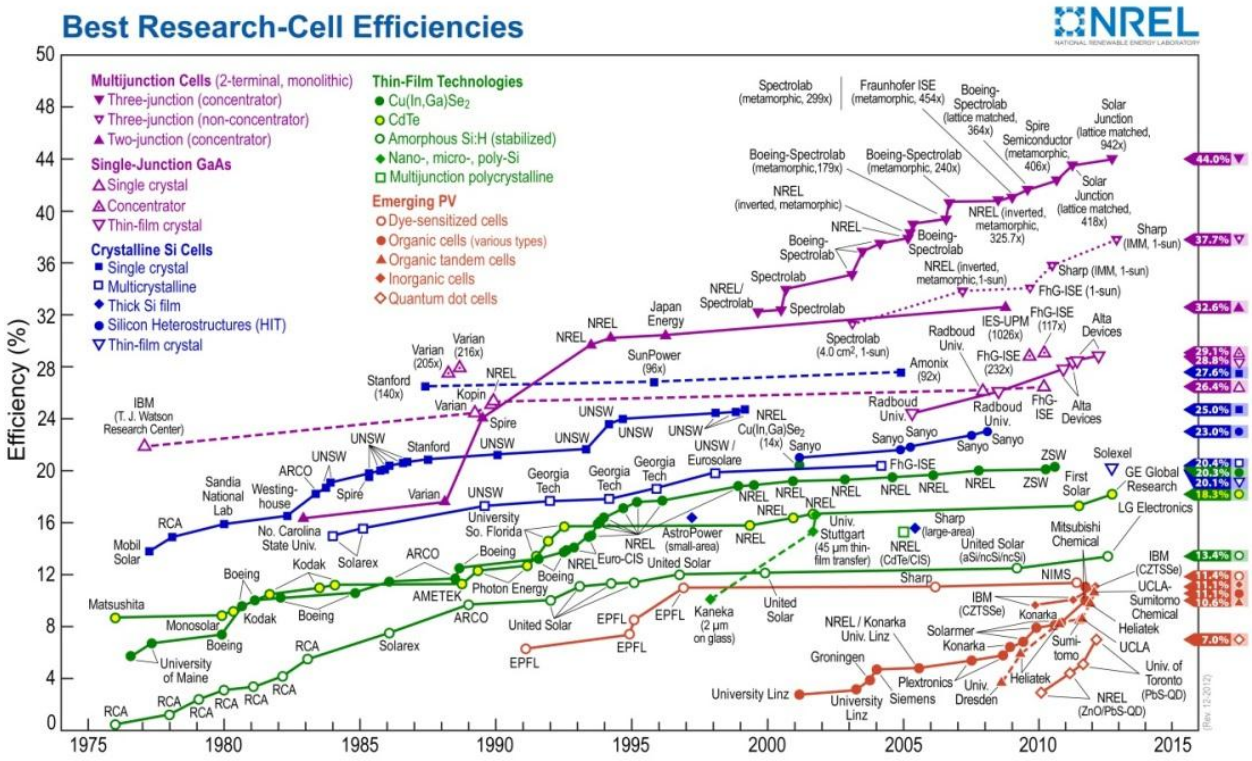

Figure 1.3. Reported timeline of solar cell energy conversion efficiencies

One of the challenges for solar cells technology is the intermittent and time variant nature of sunlight. Local, seasonal, and diurnal weather patterns introduce difficulty in matching the electricity energy supply and demand. More importantly, the solar cell can only generate electricity during daytime. Therefore, efficient energy storage strategies are needed for solar energy utilization in large-scale. There are number of options existed such as electrochemical systems such as batteries, and chemical energy carriers, i.e. fuels such as hydrogen. Hydrogen is one of the most promising candidates due to its high energy and power densities and its flexibility regarding conversion to other forms of energy such as heat via combustion or electricity via fuel cells. In addition, consumption of H_2 either via combustion or reaction in fuel cells produces only H_2O which is harmfulness to the environment, therefore bringing up interest in the future prospect of a so-called "Hydrogen Economy" - a proposed system of delivering energy using hydrogen as the fuel. Numerous research efforts are currently focusing on developing strategies for the efficient production, storage, transportation, and utilization of hydrogen.

Hydrogen is also a valuable basic chemical feedstock itself, used with large quantities in ammonia synthesis (mostly for fertilizer market) and petroleum refining. The current primary source of hydrogen is the steam reforming of hydrocarbons (e.g. methane). This method requires consumption of fossil fuel feedstock associated with production of CO_2 (5.5 tons of CO_2 are made for every ton of H_2), thus is not a sustainable strategy for long-term hydrogen production. Alternative H_2 production methods exist such as electrolysis of water using electricity and water, biological production methods via fermentative conversion of organics to bio-hydrogen, and thermochemical water splitting etc. Beside steam reforming, electrolysis of water is still

the most developed technology to produce hydrogen which contributes to roughly 4% of hydrogen produced in US despite the high cost of electricity (consuming approximately 50 kilowatt-hours of electricity per kilogram of hydrogen produced) and electrolyzer systems.

The straightforward method to utilize sunlight and water for sustainable production of H_2 is by coupling solar cells with electrolyzer systems. However, a large current density of ~ 1A m^{-2}, thus a high cell voltage (1.9 V) required for this system sets the limit of the electricity-to-hydrogen efficiency at around 65% since the thermodynamic potential required for water splitting is 1.23 eV.[6] The fusion of two systems, solar cells and electrolyzers, into a single device namely photo-electro-chemical cells is much more attractive since it reduces the capital costs and allows relatively low current densities and overpotentials for water splitting reaction, thus higher overall energy conversion efficiencies.

SOLAR HYDROGEN PRODUCTION FROM PHOTOELECTROCHEMICAL (PEC) WATER SPLITTING

Solar hydrogen production via the photoelectrolysis of water using semiconductors is considered as the "Holy Grail" of chemistry.[7] The Gibbs free energy for the conversion of one mole of H_2O (liquid) to 1 mole of H_2 (gas) and ½ mole of O_2 (gas) is 237.2 kJ, corresponding to ΔE^o = 1.23 V per electron transferred.[8] It means that for electrochemical decomposition of water, a potential difference of 1.23 V or more is thermodynamically required between anode and cathode. This potential difference is equivalent to the energy of photon with a wavelength of 1008 nm or shorter, indicating that water can be decomposed using visible light. Since water does not absorb visible light, water can only be decomposed directly under irradiation of wavelengths shorter

than 190 nm. In 1972, Fujishiima and Honda first reported electrochemical photolysis of water on a TiO_2 rutile photoanode under ultra violet irradiation.[9]

Figure 1.4 shows the operation principle for a photo-electrochemical water splitting cell using an n-type semiconductor as the photoanode and a metal cathode (usually Pt). Upon absorption of a photon having energy equal or higher than the band gap energy, an electron is promoted from the valence band into the conduction band of the semiconductor, leaving a positive charge called "hole" in the valence band. The photogenerated electrons and holes are then separated by an electric field close to the interface between the semiconductor and the electrolyte. This electric field is formed during the formation of a Schottky-type contact between the semiconductor and the electrolyte. The photogenerated electrons travel to the back contact and are then transported to the counter electrode where they reduce water, forming hydrogen. The positive charge 'holes' migrate to the interface, where they oxide water to produce oxygen.

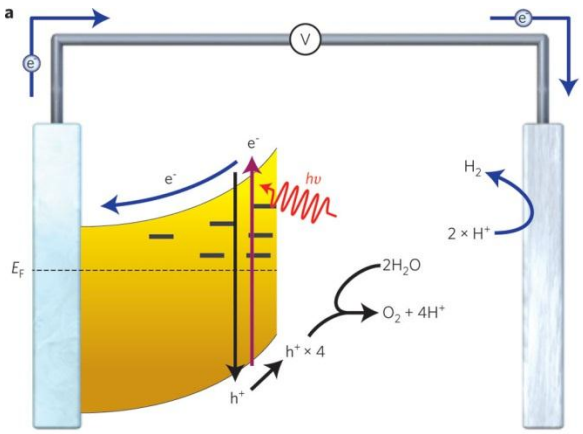

Figure 1.4. A PEC cell for photo water splitting using an n-type semiconductor photoanode.[10]

Solar-to-hydrogen (STH) efficiencies are determined as the chemical energy stored in hydrogen molecules divided by the solar energy input. In a PEC cell, assuming that all the current flows through the outer circuit corresponds to the water splitting reaction, the STH efficiency can be obtained using Equation (1):[6,11]

$$\eta_{STH} = \frac{j(V_{redox} - V_B)}{P_{light}} \quad (1)$$

where j is the photocurrent density (mA cm^{-2}), V_{redox} is the potential required for water splitting (1.23 V), V_B (V) is the bias voltage applied between the oxygen-evolving photoanode and the hydrogen-evolving photocathode, and P_{light} is the incident light intensity (mW cm^{-2}).

In order to compete with the current industrial hydrogen production technology, the common target STH efficiency required for a PEC cell is 10% with a lifetime of at least 10 years.[7] The world-record STH efficiency of 12.4 % cell using GaAs/GaInP2 photocathode wired to a Pt anode was reported by Turner et al. in 1998,[12] however, the materials were expensive and unstable in aqueous environments under illumination. Significant research efforts have focused on discovering and developing efficient photoactive materials. For efficient solar hydrogen production, the photoactive materials have to satisfy the following requirements:

1. Abundance and low-cost
2. High chemical stability in aqueous solution under illumination
3. Suitable band edge positions to enable reduction/oxidation of water: the conduction band minimum (CBM) and the valence band maximum (VBM) should straddle the oxygen and hydrogen evolution potentials.
4. High visible light absorption
5. Efficient charge transport
6. Low overpotentials for the reduction/oxidation reactions of water

Despite enormous research effort during past 4 decades, there is still no known material that satisfies all the requirements mentioned above. Materials showing high activity tend to be not photo-stable in aqueous solution, such as materials used for solar cells. Vice versa, those demonstrating good stability tend to show poor solar conversion properties, such as TiO_2, a-Fe_2O_3, and $BiVO_4$ etc. Besides discovering new materials, strategies to develop efficient PEC materials include improving solar conversion properties of stable materials and stabilizing active materials. In our research, we focus on optimizing PEC performance of TiO_2 – a stable but wide band gap material via improving charge transport properties and visible light absorption properties.

TiO_2 AS THE PHOTOCATALYST FOR WATER SPLITTING

Since the first demonstration of its application in photoeletrolysis of water, TiO_2 has been the subject of extensive research, which has led to not only PEC water splitting but also many other applications such as photo-assisted oxidation of oil and organics, gas sensors, catalyst supports, the Li-ion battery, etc.[13-15] In fact, TiO_2 is still the most studied material for water splitting application due to its abundance, photo-stability in aqueous solution, high photocatalytic activity, and electronic band structures with the band edges straddling the water redox potentials.[13,16,17] However, due to its large band gap (~3.2 eV), TiO_2 can only utilize ultraviolet (UV) photons that contribute ~ 5% of the total energy of the solar spectrum.[18-21] There have been numerous investigations regarding the band structure engineering and band gap narrowing of TiO_2 in order to shift its absorption spectrum to visible light, which represents a greater portion of the energy in the solar spectrum.[17,22-26] For spontaneous photoelectrochemical (PEC) splitting of water without an applied bias, the band edges of the semiconductors must straddle the thermodynamic water redox potentials.[17,25] The band edge alignments of TiO_2 satisfy this requirement in

which the conduction band minimum (CBM) is ~ 0.3 – 0.4 eV more negative than the hydrogen production potential, whereas the valence band maximum (VBM) is far below (~ 1.6 eV more positive) the oxygen production potential.[17] Ideally, for efficient solar water splitting without bias, the CBM of TiO_2 should remain as is or slightly shift closer to the vacuum level (more negative on the electrochemical scale) and the valence band maximum should also shift in the same direction so that the band gap reduces to ~ 2 eV accordingly.[17,23,25]

Monodoping TiO_2 with 3d transitional metals (V[13, 14] and Cr[13]) has gained some success in extending the absorption spectrum to the visible region by introducing a donor level under the conduction band,[27,28] however the decrease in carrier mobility due to the formation of strongly localized d states within the band gap and the existence of a carrier recombination center significantly reduce the photo-induced current.[27-33] Monodoping with anions such as N,[23,34] C,[35] and S[36] has been of interest because the p states of incorporated anions (N, C, or S) normally create an impurity band above the VBM or hybridization with O 2p states, thus narrowing the band gap and keeping the CBM the same. Coincorporation of both metal cations and non-metal anions into TiO_2 has been proposed as a new approach for engineering the band structure.[17,25,37-40] The neutralization of positive and negative charges in the TiO_2 lattice created by coincorporation reduces the charge recombination centers, thus enhancing the photocatalytic activity. Moreover, co-incorporation of metal ions and nonmetal ions can help overcome solubility limits, improve material quality, and enhance optical absorption.[25]

Besides engineering the band structure, it is also very important to enhance the charge transport characteristics of materials. Vertically oriented one dimensional (1D) nanostructures such as nanowires, nanorods, nanotubes *etc*., have been demonstrated to

be advantageous over planar geometries because these 1D structures provide comparable penetration depth while still decreasing the diffusion distance of the minority charge carrier (holes for n-type and electrons for p-type semiconductors) to the electrolyte.[6,41-44]

This thesis is divided into six chapters. Chapter 1 provides general background regarding the motivation and strategies to develop solar energy conversion and storage solutions. Background on photoelectrochemical water splitting cell and TiO_2 as one of the PEC materials is also discussed on this chapter. The following four chapters provide more details on studies regarding synthesis and characterizations of nanostructured TiO_2 materials for the PEC energy conversion applications. These studies have been submitted to or published in peer-reviewed journals. In the final chapter, chapter 6, we present several conclusions from studies in chapter 2-5 and recommendations for future research along these lines.

In chapter 2, we present a solvothermal synthesis of single crystalline TiO_2 nanowire arrays with unprecedented small feature sizes of ~ 5 nm and lengths up to 4.4 μm. A substantial amount of nitrogen (up to 1.08 atomic %) can be incorporated into the TiO_2 lattice *via* nitridation in NH_3 flow at relatively low temperature (500 ^oC) because of the small cross-section of the nanowires, leading to a significant redshift in the active spectra of N-modified TiO_2 with the low-energy threshold of the incident-photon to current efficiency located at ~520 nm (2.4 eV). We also report a simple cobalt treatment for improving the PEC performance of our N-modified TiO_2 nanowire arrays.

In chapter 3, we demonstrate a strategy to further improve the PEC performance of our TiO_2 materials under visible light illumination via a synergistic effect involving hydrogenation and nitridation co-treatment of TiO_2 nanowire arrays. The active spectra of the cotreated-TiO_2 nanowires extend to 570 nm, compared to ~ 550 nm for the TiO_2

nanowires solely nitrided. We speculate that the interactions between substitutional N and Ti^{3+} are responsible for this enhancement.

In chapter 4, we demonstrate the synthesis of N and Ta-coincorporated TiO_2 (N, Ta:TiO_2) and Ta-incorporated TiO_2 (Ta:TiO_2) nanowire (NW) arrays and their application as photoanodes for water photo-oxidation. Tantalum is incorporated into TiO_2 NWs with concentrations ranging from 0.11 to 3.47 atomic % by a simple solvothermal synthesis. N, Ta:TiO_2 nanowires are prepared *via* nitridation of Ta:TiO_2 nanowires in NH_3 flow at a relatively low temperature. N, Ta:TiO_2 NWs with the optimum Ta concentration of 0.29 at. % also demonstrate significant enhancement in PEC performance with the photocurrent reaching 0.52 mA/cm^2 and 0.18 mA/cm^2 under AM 1.5 G and visible light (>420 nm) illumination, compared with 0.26 mA/cm^2 and 0.13 mA/cm^2 for that of N:TiO_2 NWs, although the active spectrum of the N, Ta:TiO_2 NW sample only extends to ~ 520 nm (2.38 eV), compared to ~ 540 nm (2.30 eV) for N:TiO_2 NWs. We believe that the enhancement shown by the N, Ta-coincorporated sample is due to less recombination centers from charge compensation effects and suppression of the formation of an amorphous layer on the nanowires during the nitridation process.

In chapter 5, we report a facile, scalable, low cost, and low temperature (80 ^oC) hydrothermal synthesis of vertically aligned TiO_2 nanoplatelet arrays on various substrates including fluorine-doped tin oxide coated glass substrates and their applications for PEC water splitting and dye sensitized solar cells. The TiO_2 arrays consisting of single crystal rutile nanoplatelets with heights (film thicknesses) of up to 1 μm, lengths of up to 130 nm, and widths of ~ 5 nm were grown via controlling oxidation and hydrolysis of $TiCl_3$ at low pH (0.71-0.85) and low $TiCl_3$ concentration (8-40 mM). As a photoanode for water oxidation in a PEC water splitting cell, the TiO_2 nanoplatelets show excellent charge separation characteristics with a saturated photocurrent in 1 M

KOH electrolyte under AM 1.5 G illumination of ~ 0.4 mA/cm^2 reached at an exceptionally low bias of -0.6 V vs Ag/AgCl (0.4 V vs. reversible hydrogen electrode). Dye sensitized solar cells assembled using N719 dye sensitized-TiO_2 nanoplatelet arrays also show promising performance with photoconversion efficiencies of 1.28 % for as-synthesized (no thermal post-treatment) and 3.7 % for annealed TiO_2 nanoplatelets.

REFERENCES

(1) US Energy Information Administration, International Energy Outlook **2011**.

(2) Lewis, N. S.; Nocera, D. G. *PNAS* **2006**, *103*, 15729.

(3) Lewis, N. S.; Crabtree, G. W. "Basic Research Needs for Solar Energy Utilization: Report on the Basic Energy Sciences Workshop on Solar Energy Utilization," 2005.

(4) Kamat, P. V. *J. Phys. Chem. C* **2007**, *111*, 2834.

(5) Administration, U. S. E. I. **2007**.

(6) van de Krol, R.; Liang, Y. Q.; Schoonman, J. *J. Mater. Chem.* **2008**, *18*, 2311.

(7) Bard, A. J.; Fox, M. A. *Acc. Chem. Res.* **1995**, *28*, 141.

(8) Walter, M. G.; Warren, E. L.; McKone, J. R.; Boettcher, S. W.; Mi, Q.; Santori, E. A.; Lewis, N. S. *Chem. Rev.* **2010**, *110*, 6446.

(9) Fujishima, A.; Honda, K. *Nature* **1972**, *238*, 37.

(10) Tachibana, Y.; Vayssieres, L.; Durrant, J. R. *Nature Photonics* **2012**, *6*, 511.

(11) Chen, Z. B.; Jaramillo, T. F.; Deutsch, T. G.; Kleiman-Shwarsctein, A.; Forman, A. J.; Gaillard, N.; Garland, R.; Takanabe, K.; Heske, C.; Sunkara, M.; McFarland, E. W.; Domen, K.; Miller, E. L.; Turner, J. A.; Dinh, H. N. *J. Mater. Res.* **2010**, *25*, 3.

(12) Khaselev, O.; Turner, J. A. *Science* **1998**, *280*, 425.

(13) Chen, X.; Mao, S. S. *Chem. Rev.* **2007**, *107*, 2891.

(14) Pishko, M. V.; Cook, J. P.; Heller, E.; Schwitzgebel, J.; Gunawan, G.; Ekerdt, J. G.; Heller, A. *Abstracts of Papers of the American Chemical Society* **1994**, *207*, 208.

(15) Lin, Y.-M.; Abel, P. R.; Flaherty, D. W.; Wu, J.; Stevenson, K. J.; Heller, A.; Mullins, C. B. *J. Phys. Chem. C* **2011**, *115*, 2585.

(16) Leary, R.; Westwood, A. *Carbon* **2011**, *49*, 741.

(17) Gai, Y.; Li, J.; Li, S.-S.; Xia, J.-B.; Wei, S.-H. *Phys. Rev. Lett.* **2009**, *102*, 036402.

(18) Linsebigler, A. L.; Lu, G.; Yates, J. T. *Chem. Rev.* **1995**, *95*, 735.

(19) Bolton, J. R. *Solar Energy* **1996**, *57*, 37.

(20) Bolton, J. R.; Strickler, S. J.; Connolly, J. S. *Nature* **1985**, *316*, 495.

(21) Murphy, A. B.; Barnes, P. R. F.; Randeniya, L. K.; Plumb, I. C.; Grey, I. E.; Horne, M. D.; Glasscock, J. A. *Int. J. Hydrogen Energy* **2006**, *31*, 1999.

(22) Chen, X.; Liu, L.; Yu, P. Y.; Mao, S. S. *Science* **2011**, *331*, 746.

(23) Asahi, R.; Morikawa, T.; Ohwaki, T.; Aoki, K.; Taga, Y. *Science* **2001**, *293*, 269.

(24) Khan, S. U. M.; Al-Shahry, M.; Ingler, W. B. *Science* **2002**, *297*, 2243.

(25) Yin, W.-J.; Tang, H.; Wei, S.-H.; Al-Jassim, M. M.; Turner, J.; Yan, Y. *Phys. Rev. B* **2010**, *82*, 045106.

(26) Choi, J.; Park, H.; Hoffmann, M. R. *J. Mater. Res.* **2010**, *25*, 149.

(27) Umebayashi, T.; Yamaki, T.; Itoh, H.; Asai, K. *J. Phys. Chem. Solids* **2002**, *63*, 1909.

(28) Ohno, T.; Tanigawa, F.; Fujihara, K.; Izumi, S.; Matsumura, M. *J. Photochem. Photobiol.* **1998**, *118*, 41.

(29) Chen, X. B.; Lou, Y. B.; Dayal, S.; Qiu, X. F.; Krolicki, R.; Burda, C.; Zhao, C. F.; Becker, J. *J. Nanosci. Nanotechnol.* **2005**, *5*, 1408.

(30) Choi, W. Y.; Termin, A.; Hoffmann, M. R. *J. Phys. Chem.* **1994**, *98*, 13669.

(31) Janisch, R.; Gopal, P.; Spaldin, N. A. *J. Phys.: Condens. Matter* **2005**, *17*, R657.

(32) Litter, M. I.; Navio, J. A. *J. Photochem. Photobiol.* **1996**, *98*, 171.

(33) Dvoranova, D.; Brezova, V.; Mazur, M.; Malati, M. A. *Appl. Cat. B* **2002**, *37*, 91.

(34) Hoang, S.; Guo, S.; Hahn, N. T.; Bard, A. J.; Mullins, C. B. *Nano Lett.* **2012**, *12*, 26.

(35) Park, J. H.; Kim, S.; Bard, A. J. *Nano Lett.* **2005**, *6*, 24.

(36) Umebayashi, T.; Yamaki, T.; Itoh, H.; Asai, K. *Appl. Phys. Lett.* **2002**, *81*, 454.

(37) Long, R.; English, N. J. *Chem. Phys. Lett.* **2009**, *478*, 175.

(38) Zhu, W.; Qiu, X.; Iancu, V.; Chen, X.-Q.; Pan, H.; Wang, W.; Dimitrijevic, N. M.; Rajh, T.; Meyer, H. M.; Paranthaman, M. P.; Stocks, G. M.; Weitering, H. H.; Gu, B.; Eres, G.; Zhang, Z. *Phys. Rev. Lett.* **2009**, *103*, 226401.

(39) Breault, T. M.; Bartlett, B. M. *J. Phys. Chem. C*, *116*, 5986.

(40) Gai, Y. Q.; Li, J. B.; Li, S. S.; Xia, J. B.; Yan, Y. F.; Wei, S. H. *Phys. Rev. B* **2009**, *80*, 153201.

(41) Hahn, N. T.; Ye, H.; Flaherty, D. W.; Bard, A. J.; Mullins, C. B. *ACS Nano* **2010**, *4*, 1977.

(42) Mor, G. K.; Prakasam, H. E.; Varghese, O. K.; Shankar, K.; Grimes, C. A. *Nano Lett.* **2007**, *7*, 2356.

(43) Cho, I. S.; Chen, Z.; Forman, A. J.; Kim, D. R.; Rao, P. M.; Jaramillo, T. F.; Zheng, X. *Nano Lett.* **2011**, *11*, 4978.

(44) Feng, X.; Shankar, K.; Varghese, O. K.; Paulose, M.; Latempa, T. J.; Grimes, C. A. *Nano Lett.* **2008**, *8*, 3781.

Chapter 2: Visible Light Driven Photoelectrochemical Water Oxidation on Nitrogen-Modified TiO2 Nanowires

INTRODUCTION

Titanium dioxide (TiO_2) is well known as a candidate for water photo-oxidation as it is abundant, stable in aqueous solution under irradiation, and it has strong photocatalytic activity.[1, 2] However, due to its large band gap (~3.0 eV for rutile and 3.2 eV for anatase), TiO_2 is only active in the ultraviolet (UV) region which contributes less than 5% of the total energy of the solar spectrum.[3] Shifting the absorption of TiO_2 to include visible light, which composes a greater portion of the solar spectrum (45%), is one of the prerequisites to enhancing the solar energy conversion efficiency of titania.[4-7] Another requirement of an effective photomaterial is good electron-hole separation characteristics, which can be improved by increasing charge transfer (normally *via* nanostructuring the morphology and doping with foreign ions) and increasing the kinetics of water oxidation by holes and water reduction by electrons (*via* loading of co-catalysts). TiO_2 has short a hole diffusion length (about 10 nm for the rutile single crystal),[8] therefore it is necessary to reduce the TiO_2 characteristic size to decrease the diffusion pathway of photoholes to the electrode/electrolyte interface. Moreover, in a photoelectrochemical (PEC) cell, electrons generated in the TiO_2 photoanode film have to travel within the TiO_2 film to the back contact, and then transfer to the cathode. Therefore the optimum morphology is a one-dimensional single crystalline structure to enable electrons to travel to the back contact and holes to diffuse to the electrode/electrolyte interface in the easiest manner without scattering at a grain boundary. Co-catalysts such as IrO_2,[9] Co based materials,[10] and Co-Pi[11] for water oxidation are also needed to increase the kinetics of the reactions, thus reducing the charge recombination rate.

Incorporating nitrogen has been said to narrow the band gap of TiO_2 for water splitting applications since substitutional N 2p states hybridize with O 2p states, upshifting the valence band edge while almost keeping the conduction band edge in the same position.[4, 12, 13] However, there is an on-going debate regarding the red-shift of the absorption edge of N-modified TiO_2. Some researchers believe substitutional N forms isolated N 2p midgap states slightly above the top of the O 2p valence, instead of mixing with O 2p to form a continuous valence band as proposed above.[14-16] In this case, photogenerated holes may be trapped in these localized states leading to a high recombination rate, thus decreasing the quantum yields of N-modified TiO_2. Some other researchers suggest that high doping of nitrogen in TiO_2 produces color centers with a different local chemical composition and electronic structure.[17, 18] In this picture, the color centers, including Ti^{3+}, are responsible for visible light absorption in the N-modified TiO_2 material.

Nitrogen incorporation can be accomplished by calcining TiO_2 under NH_3. However, due to the low solubility of N in the TiO_2 lattice, the reactions normally have to be conducted at high temperatures (above 550 ^oC) to yield sufficient N-dopant incorporation for better visible light absorption. However, annealing in NH_3 at such high temperatures leads to unwanted side-effects such as defect formation within the TiO_2 lattice, degradation of the transparent conductive substrate (FTO), and sintering of the nanostructure.

In this letter, we report a simple hydrothermal synthesis route for growing densely packed, vertical, single crystalline TiO_2 rutile nanowire arrays on FTO substrates of unprecedented small cross-section with a characteristic dimension of ~5 nm and lengths up to 4.4 μm. A significant amount of nitrogen (up to 1.08 atomic %) can be incorporated into the TiO_2 by annealing the films under NH_3 flow at a relatively low temperature (500

^{o}C) because of the exceptionally small nanowire cross-section. Furthermore, we report a simple surface treatment employing cobalt as a co-catalyst that we believe has not been investigated previously with TiO_2, in order to improve the water oxidation performance of N-modified TiO_2. N-modified TiO_2 films without a cobalt co-catalyst yielded a lower photocurrent under a full spectrum and lower quantum yields in the UV region than similar unmodified TiO_2 samples although the N-modified samples had higher visible light photocurrents. A cobalt co-catalyst not only enhances the quantum yield in the visible light region but also restores the quantum yield in the UV region compared to the equivalent values of the unmodified samples.

EXPERIMENTAL METHODS

Material Characterization

Scanning electron microscopy (SEM) was performed on a Zeiss field-emission SEM using a 10 kV focus voltage and on a Hitachi S-5500 scanning transmission electron microscope (STEM) using a 30 kV focus voltage. Transmission electron microscopy (TEM) was performed on a JEOL 2010F field-emission TEM. The JEOL 2010F was also used to collect energy dispersive x-ray spectroscopy (EDX) spectra for elemental analysis. Grazing incidence X-ray diffraction (GIXRD) patterns were collected with a Bruker D8 diffractometer. UV−vis absorbance spectra were taken with a Cary 5000 spectrophotometer using a blank FTO substrate as a baseline standard. The transmittance spectra were collected using a Cary 500 UV-vis-NIR spectrophotometer attached to a Labsphere DRA-CA-5500 integrating sphere. X-ray photoelectron spectroscopy (XPS) was performed on a Kratos Axis X-ray photoelectron spectrometer. The binding energy was calibrated using the C 1s photoelectron peak at 284.6 eV as a reference. The elemental percentages were calculated from XPS spectra using the

CasaXPS computer program with specific relative sensitivity factors for the Kratos Axis XPS (Ti 2p: 2.001, O 1s: 0.78, and N 1s: 0.47). CasaXPS was also used for peak fitting on XPS spectra. Ultraviolet photoemission spectroscopy (UPS) measurements were performed on the same Kratos Axis in XPS measurements. UPS spectra were collected using the He (I) line (21.2 eV) with a negative bias voltage of -8.7 V applied to the samples in order to shift the spectra from the spectrometer threshold. The UPS spectrum for each sample was scanned 5 times to ensure that the uncertainty is smaller than the scan resolution (0.05 eV). The spectra were calibrated versus the Fermi edge of a polycrystalline Au foil.

Electrochemical and Photoelectrochemical (PEC) Characterization

The PEC measurements were performed using a three-electrode electrochemical cell with the FTO supported nanowire arrays as the working electrode, a Ag/AgCl (saturated KCl) reference electrode, a platinum wire counter electrode, and 1 M KOH electrolyte (pH = 13.5). The working electrode with exposed area of 0.16 cm^2 was illuminated from the back side (through the FTO substrate – TiO_2 nanowire interface) by a 100 W xenon lamp (Newport) through a UV/IR filter (Schott, KG3) to remove infrared (>800 nm) and short wavelength UV light (<300 nm). Using a Scientech calorimeter (Model 38-0101), the light intensity of the spectrum from 400 nm to 1.2 μm was measured as 37 mW/cm^2. The fraction of the total energy of the spectrum from 400 nm to 800 nm for our lamp is estimated to be 85% - 90 % of the total light energy, therefore, we estimate the energy flux in our PEC measurements to be ~ 41 – 43 mW/cm^2. A CHI 832 electrochemical station was used for linear sweep voltammetry (I-V) and amperometry (I-t) measurements. Incident photon to current conversion efficiencies (IPCEs) were calculated from amperometry measurements using a monochromator (Newport) in conjunction with a power meter and photodiode (Newport), given by:

$$IPCE = \frac{1240 \times j_{ph}}{\lambda \times I} \times 100\ \%$$

Where j_{ph} is the steady-state photocurrent density at a specific wavelength, λ is the wavelength of the incident light. I is the light power intensity of the wavelength at the film surface, I ranges from 80-300 $\mu W/cm^2$ over the spectrum of wavelengths studied (320 nm-550 nm). .

The measured potentials *vs.* the Ag/AgCl were converted to the reversible hydrogen electrode (RHE) scale *via* the Nernst equation

$$E_{RHE} = E_{Ag/AgCl} + 0.059\ pH + E^{o}_{Ag/AgCl}$$

where E_{RHE} is the converted potential vs. RHE, $E_{Ag/AgCl}$ is the experimental potential measured against Ag/AgCl reference electrode, and $E^{o}_{Ag/AgCl}$ is the standard potential of Ag/AgCl at 25 ^{o}C (0.1976 V).

RESULTS AND DISCUSSION

Synthesis of TiO_2 nanowire arrays.

FTO coated glass substrates were first cleaned by sonication in a mixture of ethanol and water for 30 minutes, subsequently rinsed by deionized (DI) water, and finally dried in an air stream. In order to enhance the sample integrity and shorten the growing time, FTO substrates were also seeded with a thin layer of TiO_2 before growing the nanowire arrays. For seeding, clean FTO substrates were first soaked in 0.025M $TiCl_4$ in n-hexane for 30 minutes. They were then taken out, rinsed by ethanol, and finally annealed in air at 500 ^{o}C for 30 minutes. In a typical hydrothermal growth procedure, the seeded FTO substrates were placed on the bottom of a Teflon lined autoclave (125 mL,

Parr Instrument), containing 50 mL n-hexane (Extra dry, 96+%, Acros Organics), 5 mL HCl (ACS Reagent Grade 36.5-38%, MP), and 2.5 - 5 mL of titanium (IV) isopropoxide (98+%, Acros Organics). The hydrothermal synthesis was conducted at 150 ^{o} C for certain amount of time in a box oven. After the reaction was completed and the autoclave naturally cooled down to room temperature, the TiO_2 nanowire films were taken out and cleaned by rinsing with copious amount of ethanol and water.

The hydrothermal growth of vertical TiO_2 nanowire arrays on FTO with feature sizes of ~ 20 nm *via* a nonpolar solvent/hydrophilic solid substrate interfacial reaction was first reported by Grimes and co-workers.[19] Using a similar strategy, we developed the recipe (*i.e.*, titanium precursors, nonpolar solvents) and hydrothermal reaction conditions (*i.e.*, reaction time and temperature) described above that enable the synthesis of high quality rutile TiO_2 single crystalline nanowire arrays with smaller feature sizes (~ 5 nm). As proposed by Grimes *et al.*,[19] at room temperature, titanium precursors (*e.g.*, TTIP) and water (from hydrochloric acid solution) are separated since the precursors are soluble and water is immiscible in the nonpolar solvents (*e.g.*, n-hexane). Under hydrothermal conditions, to minimize system energy, water diffuses to the hydrophilic FTO surface where it hydrolyzes with TTIP to form TiO_2 nuclei on the FTO surface. As the newly-formed TiO_2 nuclei are also hydrophilic, water continues to diffuse to the nuclei resulting in further hydrolysis and crystal growth. The Cl^- ions play an important role in the hydrothermal growth as they promote anisotropic growth of one dimensional nanocrystals. The Cl^- ions are inclined to absorb on the rutile (110) plane, thus retarding further growth of this plane. We did not observe nanowire array formations when HCl was replaced by HNO_3 or H_2SO_4.

Characterization of TiO_2 nanowire arrays.

Shown in figure 2.1a and b are cross-sectional-view and top-view scanning electron microscope (SEM) images of a typical as-synthesized (with no further heat treatment) nanowire film. The nanowire arrays consisting of vertically-aligned and tetragonal shaped nanowires are highly uniform and densely packed with exceptionally small feature sizes (average characteristic cross-sectional dimension is ~ 5nm). The grazing incidence X-ray diffraction (GIXRD) pattern in figure 2.1d shows that the as-synthesized nanowire arrays are rutile TiO_2 with an enhancement in the (101) facet exposure relative to the standard rutile powder pattern (JCPDS #88-1175). The high resolution transmission electron microscope (HRTEM) image in figure 2.1c further confirms that the nanowires are single crystalline with an interplanar d-spacing of 0.327 nm, corresponding to (110) planes of rutile TiO_2. The atomic ratio of Ti to O was found to be ~ 1:2 using energy dispersive x-ray analysis (EDX) (the expected stoichiometric values).

The length of the nanowire arrays is a function of the TTIP to n-hexane volume ratio, the reaction conditions (*i.e.,* temperature and time), and seeding layer. The thicknesses of nanowire arrays versus reaction conditions, determined from cross-sectional view SEM, are shown in table 1. We are able to grow nanowires with lengths varying from ~ 500 nm up to 4.4 μm with no significant change in feature sizes. Moreover, if the FTO substrates are coated with a thick TiO_2 layer (~ 5 μm) prior to hydrothermal reaction, we can grow nanowire arrays with lengths up to 17 μm. Optimization of the thickness of a photoelectrode for PEC applications involves balancing the charge carrier mobility and the absorbance of photons. The photoanode should be as thin as possible to allow electrons to travel to the back contact in the shortest time while still being thick enough to absorb the majority of the photons from sunlight. In our study, the highest photocurrents were from samples with thicknesses of ~1.5 μm.

Therefore, we focused on the PEC characterization of TiO_2 nanowire films with thicknesses of 1.59 ± 0.26 μm grown at 150 ^oC for 5 hours with TTIP/n-hexane ratios of 1/20.

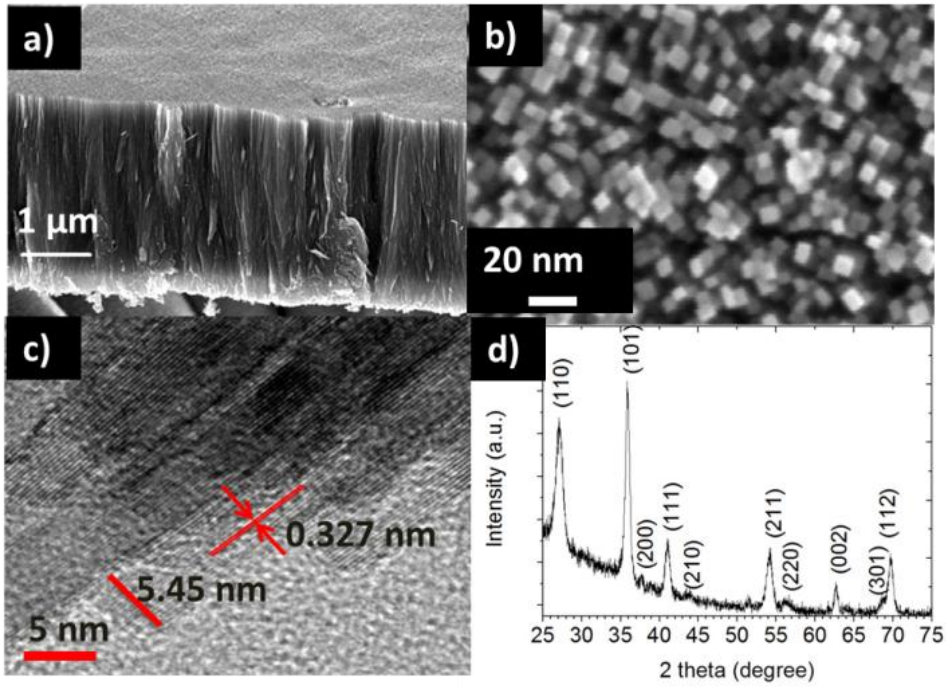

Figure 2.1. Vertically aligned single crystalline TiO_2 rutile nanowire arrays on FTO glass: (a) cross-sectional and (b) top view SEM images, (c) HRTEM image, and (d) Grazing incidence angle x-ray diffraction (GIXRD) pattern

The seeding layer enhances both the nanowire arrays' adherence to the FTO substrate and the growth rate. For example, the thickness of TiO_2 nanowire arrays grown with the ratio TTIP/n-hexane of 1/10 at 150 ^{o} C for 5 hours with and without the seeding layer are 2.60 ± 0.27 μm and 1.2 ± 0.15 μm, respectively. As mentioned above, when FTO was coated with a thick TiO_2 seeding layer of ~ 5 μm, the same reaction conditions resulted in a nanowire length of ~ 17 μm.

Table 2.1. Thicknesses of some TiO_2 nanowire arrays grown at 150 ^oC as a function of TTIP/n-hexane ratio, reaction time, and seeding layer.

TTIP/n-hexane volume ratio	*Reaction time (hour)*	*Seeding*	*Number of sample(s)*	***Length of nanowires***
1/20	5	No	1	500 nm
1/20	5	Yes	20	1.59 ± 0.26 μm
1/10	5	No	4	1.2 ± 0.26 μm
1/10	5	Yes	22	2.6 ± 0.27 μm
1/10	10	Yes	4	4.4 ± 0.27 μm

We found that the combination of titanium precursor and nonpolar solvent strongly affects the morphology of the nanowire arrays. Using a combination of titanium (IV) tetra-n-butoxide (TNBT) (Ti^{4+} precursor) and n-hexane or a combination of TTIP and toluene (nonpolar solvent) resulted in un-oriented, wire bundle formation. We further investigated nanowire array growth using a combination of TNBT and toluene which resulted in oriented but shorter nanowire arrays (~1.3 μm) with bigger feature sizes (~ 15 nm) (Figure 2.2).

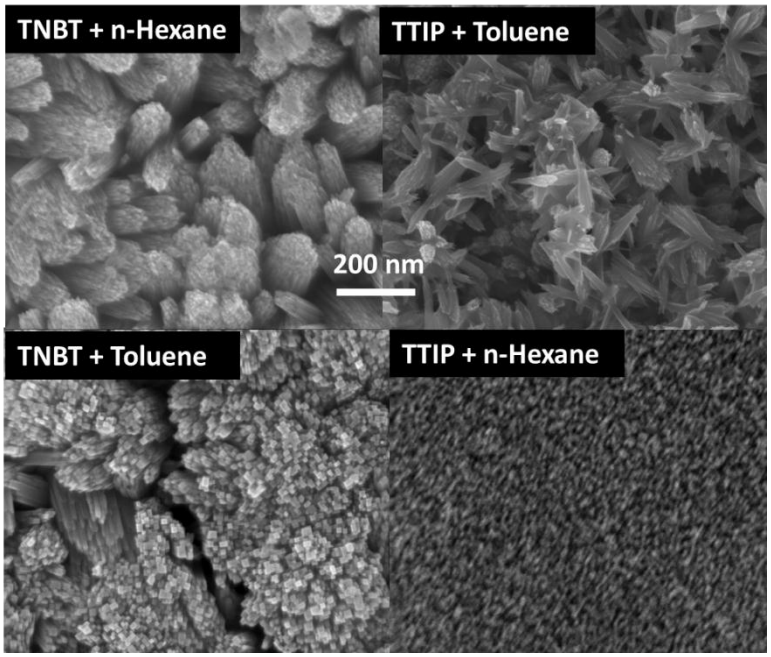

Figure 2.2. Morphology dependence of nanowire arrays on combinations of titanium precursors (*i.e.,* titanium tetra-isopropoxide (TTIP) and titanium (IV) tetra-n-butoxide (TNBT)) and non-polar solvents (*i.e.,* n-hexane and toluene). The scale bar applies to all the micrographs.

PEC properties of TiO_2 nanowire arrays.

The PEC characterization of TiO_2 nanowire samples was performed using a three-electrode electrochemical cell with the FTO supported nanowire arrays as the working electrode, a Ag/AgCl (saturated KCl) reference electrode, a platinum wire counter electrode, and 1 M KOH electrolyte (pH = 13.5). The working electrode with exposed area of 0.16 cm^2 was illuminated from the back side (through the FTO substrate – TiO_2 nanowire interface) by a 100 W xenon lamp (Newport) through a UV/IR filter (Schott, KG3) to remove infrared (>800 nm) and short wavelength UV light (<300 nm). Using a Scientech calorimeter (Model 38-0101), the light intensity of the spectrum from 400 nm to 1.2 μm was measured as 37 mW/cm^2. The fraction of the total energy of the spectrum from 400 nm to 800 nm for our lamp is estimated to be 85% - 90 % of the total light

energy, therefore, we estimate the energy flux in our PEC measurements to be ~ 41 – 43 mW/cm^2. Incident photon to current conversion efficiencies (IPCEs) were calculated from amperometry measurements using a monochromator (Newport) with a bandwidth of 7.4 nm in conjunction with a power meter and photodiode (Newport), given by:

$$IPCE = \frac{1240 \times j_{ph}}{\lambda \times I} \times 100\ \% \qquad (1)$$

where j_{ph} is the steady-state photocurrent density at a specific wavelength, and λ is the wavelength of the incident light. *I* is the light intensity for wavelength λ at the film surface, *I* ranges from 80-300 μW/cm^2 over the spectrum of wavelengths studied (320 nm-550 nm).

The measured potentials *versus* the Ag/AgCl reference electrode were converted to the reversible hydrogen electrode (RHE) scale *via* the Nernst equation

$$E_{RHE} = E_{Ag/AgCl} + 0.059\ pH + E^{o}_{Ag/AgCl} \quad (2)$$

where E_{RHE} is the converted potential vs. RHE, $E_{Ag/AgCl}$ is the experimental potential measured against the Ag/AgCl reference electrode, and $E^{o}_{Ag/AgCl}$ is the standard potential of Ag/AgCl at 25 ^{o}C (0.1976 V). We also used the same testing conditions for other samples throughout this study.

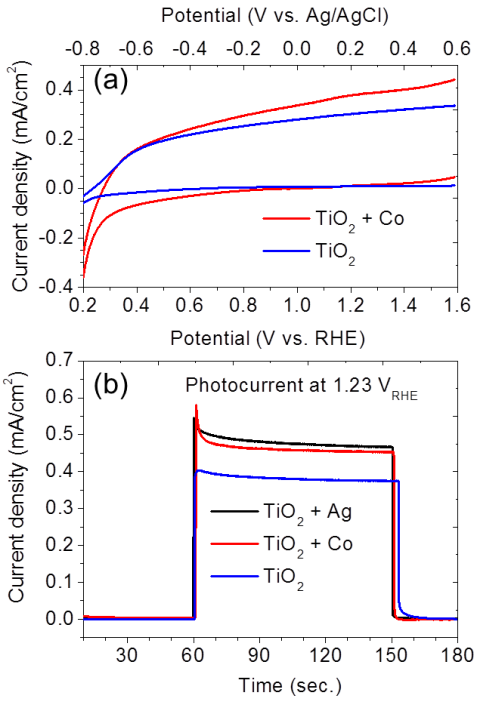

Figure 2.3. (a) Linear sweep voltammetry (LSV) measurements of TiO_2 nanowire arrays (1.6 μm) and the same film after cobalt treatment and (b) chronoamperometry measurement (at 1.23 V_{RHE}) of TiO_2 nanowire arrays and the same film after cobalt treatment and silver treatment (cobalt treatment and silver treatment were performed on two different areas on the same TiO_2 nanowire sample). All experiments were performed with 1 M KOH electrolyte (pH=13.5) and a 100 W Xenon lamp coupled with a UV/IR filter as the light source as described in the text.

Before testing, the as-synthesized films were annealed in air at 500 ^oC for one hour to remove contaminants and increase the adherence of the TiO_2 arrays to the SnO_2 layer. Figure 2.3a shows the linear sweep voltammetry of the TiO_2 nanowire sample. The onset potential of our TiO_2 nanowire arrays is ~ 0.2 V_{RHE}, around 0.2 V more negative compared to a TiO_2 nanotube sample.[5] In order to improve the PEC performance, we also applied a cobalt treatment technique similar to that reported by Grätzel *et al.*[10] in which the TiO_2 nanowire arrays were soaked in 0.1 M $Co(NO_3)_2$ for one minute, followed by

rinsing with a copious amount of water. The photocurrent measured at 1.23 V_{RHE} was improved by ~ 20 % due to the cobalt treatment, from 0.38 mA/cm^2 [without treatment] to 0.46 mA/cm^2. Cobalt based materials such as Co-Pi are well-known catalysts for the water oxidation reaction.[11] However, to our knowledge, there have not been any reports on PEC enhancement of TiO_2 due to loading cobalt as a co-catalyst, probably due to the high intrinsic oxidative power of the holes photogenerated within the valence band of TiO_2. We speculate that in this case the cobalt treatment improves the PEC performance mainly via the saturation of dangling bonds on the TiO_2 surface, thus passivating the surface states which act as charge recombination centers. Employing a silver treatment (similar to cobalt treatment), in which 0.05 M $AgNO_3$ replaced 0.1 M $Co(NO_3)_2$, leads to a similar improvement (figure 2.3b), supporting our speculation.

We have also noticed that the orientation of the FTO placed in the reactor, *i.e.*, whether it 'faces up' or 'faces down' during the nanowire growth affects the PEC performance although it does not affect the growth rate of the nanowire arrays. The films grown with the FTO 'facing up' yielded a photocurrent ~ 10- 15% higher than films grown with the FTO 'facing down'. The samples grown with the FTO 'facing up' have some flower-like micro-size particles on top (Figure 2.4) which have been reported to enhance light harvesting, thus improving the PEC performance.[20, 21]

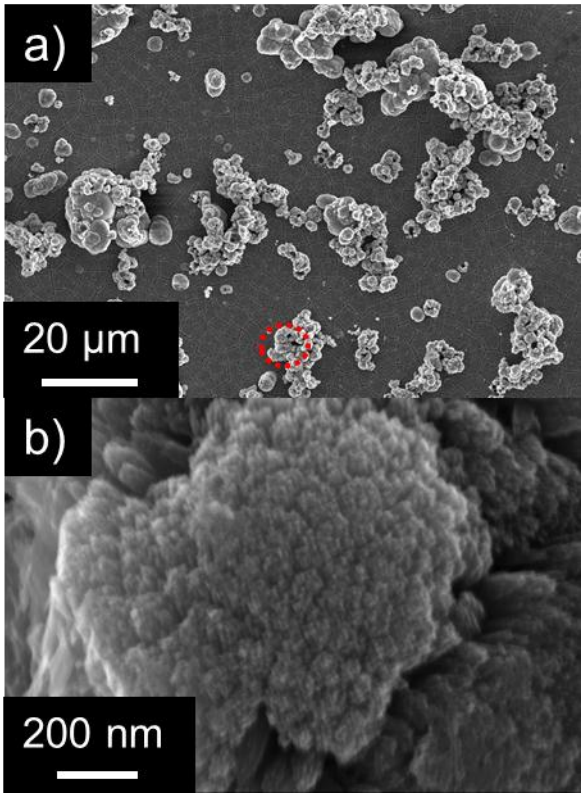

Figure 2.4. (a) Top-view SEM images of flower-like microparticles on top of the TiO_2 nanowire arrays and (b) the nanostructure of the flower-like particles (zoom-in view of the dotted circle in S2-a)

Synthesis of N-modified TiO_2 nanowire arrays. Nitrogen modified TiO_2 films were prepared by annealing TiO_2 nanowire films in an NH_3 flow (100 mL/min) at temperatures from 400 ^oC to 650 ^oC. The color of all films changed from cloudy white to bright yellow, indicating successful N incorporation. The average feature size of N-modified TiO_2 nanowires is around 15 nm, larger than that of the as-synthesized sample, probably due to sintering of the nanowires at elevated temperatures (Figure 2.5). At calcination temperatures higher than 500 ^oC (*i.e.,* 550 ^oC, 600 ^oC, and 650 ^oC), FTO substrates were damaged and not electrically conductive. Wang et al. reported that at

temperatures higher than 550 ^{o}C, NH_3 decomposes, releasing H_2 and causing partial reduction of TiO_2.[22] The appearance of Sn signals in the XRD patterns of these films suggests that the SnO_2 layer was also reduced (data not shown). Compared with films annealed at lower temperatures (*i.e.,* 400 ^{o}C and 450 ^{o}C), films nitrided at 500 ^{o}C showed the highest photocurrent. Therefore, we focused on characterizing films annealed in NH_3 at 500 ^{o}C.

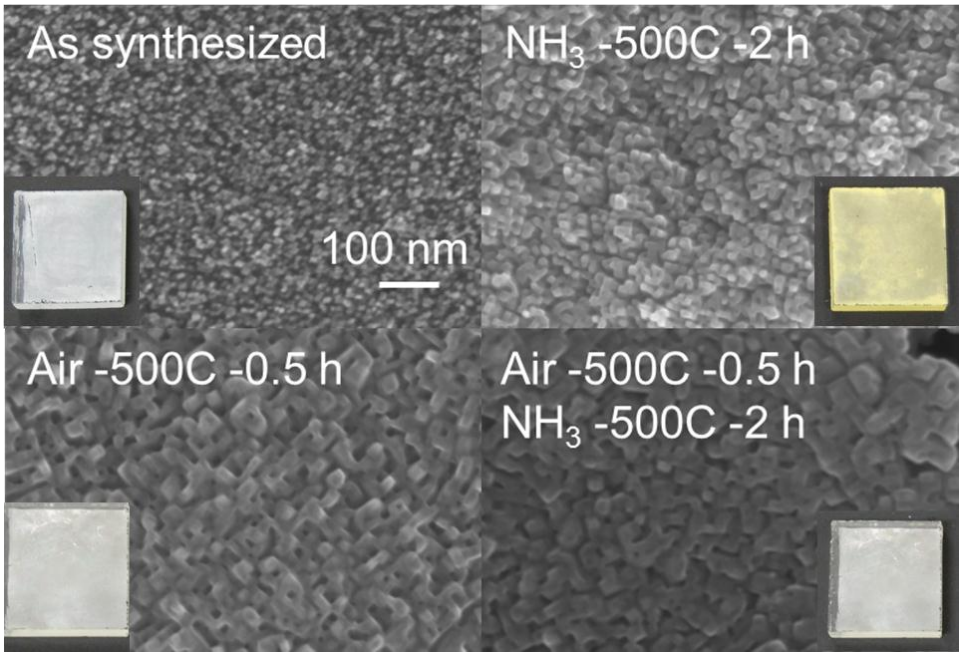

Figure 2.5. Top-view SEM image of TiO_2 nanowire arrays: as-synthesized film, film annealed in NH_3 at 500 ^{o}C for 2 hours, film annealed in air at 500 ^{o}C for 0.5 hours, and film annealed in air at 500 ^{o}C for 0.5 hours, followed by nitridation at 500 ^{o}C for 2 hours. The scale bar applies for all micrographs. The insets show the digital images of the corresponding films on FTO substrates (1.5 cm x 1.5 cm).

Chemical characterization of N-modified TiO_2 nanowire arrays. The N 1s XPS spectra of TiO_2 nanowire films annealed at 500 ^oC in NH_3 flow both for 1 hour and 2 hours are shown in figure 2.6a-3 and figure 2.6a-4, respectively. Two N 1 s binding energy peaks around 400 eV and 394 eV in the films annealed in NH_3 clearly indicate that N has been successfully incorporated into the TiO_2 lattice. The N 1s peak at ~ 400 eV can be attributed to either interstitial N[23, 24] atoms or chemisorbed N-containing gas such as NH_3 or N_2.[4, 25, 26] However, its origin and contribution to visible light absorption are still under debate. According to early XPS investigations on N-modified TiO_2,[12, 22, 24-26] the N 1s peak at 392 - 396 eV was assigned to β-N in the Ti-N bond or N substituted at oxygen sites (substitutional N). There is no TiN formation indicated in the XRD and also no Ti^{3+} in the XPS spectra (a typical one is shown in figure 2.6b-2) of these films suggesting that the N 1s peak at 394 eV in our N-modified TiO_2 samples may be assigned as substitutional N, resulting in a composition that can be described as $TiO_{2-x}N_x$. The substitutional N species is commonly recognized as a contributor to visible light absortion and changes in photocatalytic activity. For example, Irie *et al.*[25] reported a monotonic increase in visible light absorption, yet a monotonic decrease in photocatalytic activity with an increase in the substitutional N concentration. In addition, we did not observe formation of Ti^{3+} (figure 2.6b), one of the most important types of color centers. Therefore we believe that the substitutional N species found at 394 eV is likely the main contributor to visible light absorption and changes in the water photo-oxidation performance in the TiO_2 nanowire films as shown in the next section.

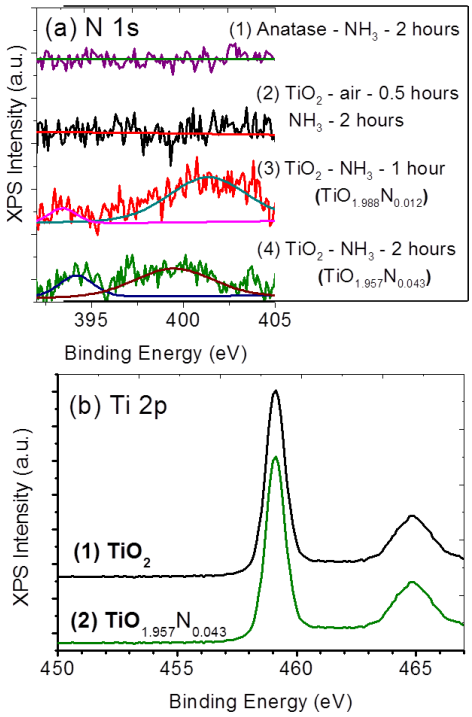

Figure 2.6. (a) Core N 1s XPS spectra of (1) anatase powder annealed in NH_3 for two hours, (2) TiO_2 nanowire film annealed in air for 30 minutes and then annealed in NH_3 for two hours, (3) and (4) TiO_2 nanowire films annealed in NH_3 at 500 ^oC for one hour and two hours, respectively and (b) core Ti 2p XPS spectra of (1) as-synthesized TiO_2 nanowire film and (2) a TiO_2 nanowire film annealed in NH_3 at 500 ^oC for two hours.

Shown in table 2.2 are our XPS analysis with atomic percentages of substitutional N in films annealed for one hour and two hours of 0.35% and 1.08 % respectively. Since the surface is rich in oxygen, probably due to the adsorption of oxygen-containing species on the surface, we calculate the values of x in $TiO_{2-x}N_x$ as x = atomic percentage of N divided by the atomic percentage of Ti, resulting in x value of 0.012 and 0.043 for samples annealed in NH_3 for 1 hour and 2 hours, respectively. Compared with other N-modified TiO_2 materials synthesized *via* nitridation of TiO_2 in NH_3 such as a rutile TiO_2 (110) single crystal,[27] anatase powder,[25] anatase films,[28, 29] and

anatase nanobelts,[22] the substitutional N concentrations in the present films are significantly higher despite lower nitridation temperatures and/or shorter times. We believe that the small feature size of the nanowire arrays allows better nitrogen diffusion into the TiO_2 lattice and that this is likely the key to the enhancement in the N-incorporation level. We performed control tests in which a TiO_2 nanowire sample with larger average characteristic size (of ~ 25 nm) prepared by pre-annealing the as-synthesized TiO_2 nanowire sample in air at 500 ^oC in 30 minutes (Figure 2.6a-2) and a commercial TiO_2 anatase nanoparticle powder with average size of 32 nm (Alfa Aesar – Figure 2.6a-1) were annealed in NH_3 under the same conditions as our as-synthesized TiO_2 nanowire films (500 ^oC for two hours). No N was detected in the XPS spectra, indicating the N uptake is very small - below the detection limit of the XPS instrument (0.1%), thus supporting our hypothesis.

Table 2.2. N-dopant concentration in TiO_2 nanowire films annealed at 500 ^oC in NH_3

Annealing conditions	**N content/ peak position (atomic %/eV)**	**x in $TiO_{2-x}N_x$**
500 ^oC- NH_3 – 1 hour	0.35 %/ 393.4 eV 3.41 %/ 401.3 eV	0.012
500 ^oC- NH_3 – 2 hours	1.08 %/ 394.2 eV 3.04 %/ 399.3 eV	0.043

PEC Properties of N-modified TiO_2 nanowire films. Figure 2.7a shows current-voltage characteristics in the dark (blue dotted line) and in white light (solid blue line) for the $TiO_{1.988}N_{0.012}$ film. Compared with unmodified TiO_2 films (Figure 2.3a), there is a positive shift in the onset potential, E_{on} from 0.2 V_{RHE} to 0.5 V_{RHE}. Indeed, the transient photocurrent onset potentials for the two samples are almost the same, at around -0.15 V_{RHE}, indicating that the flat-band potential does not shift with the inclution of N. In this case, [30] even if the band gap is reduced, the apparent photocurrent onset potential relative to the reference electrode (in a 3-electrode cell) should theoretically remain the same. We, therefore, believe that the shift in E_{on} may be due to either a larger band banding requirement for separating electrons and holes because of the material's likely possession of poorer charge-transport properties than pure TiO_2 or slower water oxidation kinetics at the surface of N-modified TiO_2 sample. Moreover, compared to an unmodified sample of the same thickness (1.6 μm), the N-modified sample shows a noticeably lower photocurrent, reaching 0.23 mA/cm^2 at 1.23 V_{RHE}, compared to 0.38 mA/cm^2 for the unmodified TiO_2 nanowire film (Figure 2.3a). Although most authors report an enhancement in the visible light response for N-modified TiO_2 films, they also observe a significant decrease in quantum yields in the UV region that leads to poor PEC performance under whole spectrum (*i.e.,* white light) illumination.[13, 15, 25, 31] Poor PEC performance has often been explained as being due to the formation of isolated N 2p states above the valence band edge, which act as electron–hole recombination centers. Using time-resolved absorption spectroscopy, Tang *et al.* reported two distinct photohole populations that are trapped at the nitrogen induced states.[32] They also demonstrated that the lack of water oxidation is due to either rapid electron-hole recombination between charges trapped at the N-incorporation induced states or the reduced oxidative power of the photoholes leading to a lack of thermodynamic driving force. Additionally, Chambers

et al. reported that the hole trapping probability at the N induced states is crystallographically dependent.[33] The hole trapping probability increases if the photogenerated holes diffuse along <110> and <001> directions and the detrapping probability increases if the holes diffuse along <100> direction. As other authors have suggested, it could be that when incorporating TiO_2 with N, substitutional N 2p states hybridize with O 2p.[4, 34] Since the N 2p state has a higher orbital energy than the O 2p state, the orbital hybridization shifts the valence band edge to more negative potentials, thus decreasing the oxidative power of photogenerated holes, which hinders hole transfer rates to oxidizable species on the film surface (H_2O or OH^-). A water oxidation electrocatalyst (WOC), therefore, may be useful in lowering the overpotential for the reaction. In the next section, we present a simple cobalt co-catalyst treatment which improves the PEC performance of our N-modified TiO_2 films.

Water Oxidation Catalyst for N-modified TiO_2 Nanowire Films. In PEC water splitting, the water oxidation half reaction is normally more challenging than water reduction and is the rate limiting step since it involves removal of a total of four electrons and four protons from two water molecules to form one oxygen molecule. There have been numerous investigations of water oxidation catalysts for photoanode materials such as Co-Pi,[11] IrO_x,[9] Pt, Co_3O_4, and IrO_x.[35] However, to our knowledge, there have not been any reports on water oxidation catalysts for N-modified TiO_2 photoanodes. We employed cobalt and silver treatments similar to that mentioned for the unmodified TiO_2 nanowire films in the previous section in which our N-modified TiO_2 films were immersed in either 0.1 M $Co(NO_3)_2$ or 0.05 M $AgNO_3$ solution for one minute followed by rinsing with a copious amount of water.

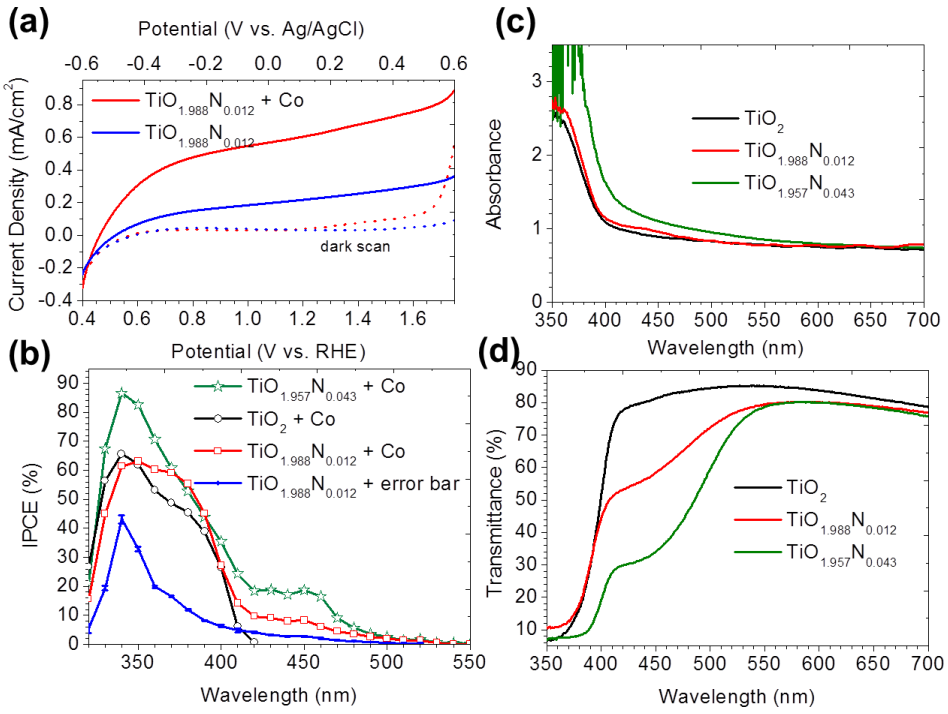

Figure 2.7. (a) Linear Sweep Voltammetry of the $TiO_{1.988}N_{0.012}$ sample and the same electrode after cobalt treatment in darkness (dotted lines) and under illumination (solid lines), (b) IPCE spectra of N-modified TiO_2 films at 1.4 V_{RHE}: blue curve and red curve are the corresponding IPCE spectra of the $TiO_{1.988}N_{0.012}$ photoelectrode in figure 4a, black curve is the IPCE of unmodified TiO_2 sample after cobalt treatment, and green curve is the IPCE of the $TiO_{1.957}N_{0.043}$ pretreated with cobalt, and (c) and (d) UV-vis absorbance spectra and UV-vis transmittance spectra of unmodified and N-modified TiO_2 nanowire samples, and an as-synthesized sample (black curve) was included as a reference

Figure 2.7a shows linear sweep voltammetry of the $TiO_{1.988}N_{0.012}$ photoanode before and after cobalt treatment. After the cobalt treatment, the photocurrent density at 1.23 V_{RHE} increases from 0.23 mA/cm^2 [without cobalt] to 0.61 mA/cm^2 (60% higher than the unmodified TiO_2 sample shown in Figure 2.3a). Compared to an unmodified sample, the cobalt treatment has a much stronger effect on N-modified TiO_2 samples with

around a 2.5 fold improvement in the photocurrent at 1.23 V_{RHE}. Silver treatment on the N-modified TiO_2 film only slightly improves the photocurrent of around 15% at 1.23 V_{RHE} (data not shown), almost the same as for the pristine TiO_2, probably because of the surface passivation effect (Ag is not known as a water oxidation co-catalyst). Therefore, we believe that in this case, the cobalt treatment plays dual roles: (1) to passivate surface states, thus increasing hole lifetime and (2) to form a cobalt-based water oxidation catalyst layer. The main PEC performance enhancement may be primarily from the water oxidation catalytic activity of the cobalt layer. We also performed a long chrono-amperometry measurement which shows no significant change in the photocurrent during 10 minutes of illumination (data not shown), suggesting good stability of N-modified TiO_2 nanowire arrays and the cobalt layer. Grätzel et al. proposed a mechanism for the electrocatalysis of water oxidation by cobalt on hematite surfaces which involves Co^{II}/Co^{III} and Co^{III}/Co^{IV} couples.[10] We believe cobalt plays a similar role on N-modified TiO_2 surfaces. Holes photogenerated within the valence band of N-modified TiO_2 have N^{3-} 2p character rather than O^{2-} 2p as in TiO_2, thus having less positive potential which results in slower kinetics for water oxidation. On cobalt modified N-modified TiO_2 surfaces, water oxidation may follow a reaction pathway that does not require the formation of energetic intermediates such as OH radicals, thus lowering the activation barrier. The photoholes generated within the valence band of pristine TiO_2 have a significant built-in overpotential for water oxidation (~ 1.6 V [30]), therefore the use of cobalt as a co-catalyst is not necessary.

Photoconversion Efficiency of N-modified TiO_2 nanowire films. IPCE tests were performed in 1 M KOH at 1.4 V_{RHE} to evaluate PEC water oxidation performance of cobalt-treated N-modified TiO_2 films (Figure 2.7b). The IPCE spectra of N-modified TiO_2 photoanodes have a low-energy threshold at a wavelength of ~ 520 nm,

corresponding to 2.4 eV (IPCE ~ 1.7 % at 520 nm for cobalt-treated $TiO_{1.957}N_{0.043}$), although they weakly responded to photons with wavelengths up to 600 nm (typical calculated IPCEs in the region from 530 nm to 600 nm were from 0.6% to ~ 0.05%). For cobalt treated unmodified TiO_2 (black curve), the PEC onset is located at around 420 nm. We note that after the cobalt treatment, the IPCE performance of N-modified TiO_2 films (green and red curves) in the UV region is restored to that of the unmodified samples. This indicates that the low water oxidation quantum yields in the UV region due to N incorporation are likely due to the lower overpotential for water oxidation of photoholes at the N-modified TiO_2 valence band edge. This lower overpotential can apparently be made up by the use of an appropriate water oxidation co-catalyst.

The IPCE spectra fit the absorbance spectra and the transmittance spectra well (figure 2.7c and figure 2.7d), which suggest that there are no major relative differences in the oxidative power of the holes photogenerated by UV and visible-light photons.[13] The conversion efficiency of visible photons appears to be limited by absorption depth. Moreover, the onset of the IPCE spectra located at ~ 550 nm confirms that the long tail at longer wavelength in the UV-vis absorbance spectra for N-modified samples is not solely due to the light scattering of the nanostructure. The plateau in the IPCE spectrum from 420 nm to 460 nm is well matched up with the plateau in the transmittance spectrum indicating that the sample absorbs photons within this range with similar efficiency. It is also interesting that the IPCE spectrum in the visible light region (greater than 420 nm) for cobalt treated $TiO_{1.9570}N_{.043}$ (Figure 2.7b, green curve) is significantly higher than that of cobalt treated $TiO_{1.988}N_{0.012}$ (Figure 2.7b, red curve). In the visible light region, the IPCE spectrum of the cobalt treated $TiO_{1.957}N_{0.043}$ film plateaus from 420 nm to 460 nm at values of ~ 18%, before decaying to ~ 0.2 % at 550 nm. The IPCE spectrum of the cobalt treated $TiO_{1.988}N_{0.012}$ film has a similar shape, but with plateau values of ~ 9%

from 420 nm to 450 nm. It is well established that more N-dopant leads to better visible light absorbance, although unfortunately this has not always lead to better water oxidation performance and photocatalytic activity.[13, 22] However, it is clear that by using a water oxidation co-catalyst, the PEC performance of cobalt treated N-modified TiO_2 can be enhanced, resulting in more than 60% higher full-spectrum photocurrent compared to unmodified TiO_2.

The UV-vis absorbance and transmittance spectra for untreated and Co-treated samples are almost identical, suggesting that the Co-catalyst does not affect the light absorption ability of the materials. Additionally, the IPCE of Co-treated TiO_2 samples does not show response to wavelength > 420 nm. Comparing with the pristine TiO2 nanowire arrays, we observed additional response from 420 nm-550 nm including the plateau from ~ 420 nm to ~ 460 nm in both of the IPCE spectra and the UV-vis transmittance spectra for all N-modified samples, suggesting that additional N-induced states are present in the range of 0 - 0.7 eV above the valence band edge of TiO_2 (or 3.0 - 2.3 eV below the conduction band edge). We believe that the density of these N-induced states is almost constant from 0 - 0.3 eV above the valence band edge. We, however, did not observe additional electronic states above the valence band edge in the valence band XPS spectra and the ultraviolet photoemission spectra (Figure 2.8) of the N-modified TiO_2 samples.

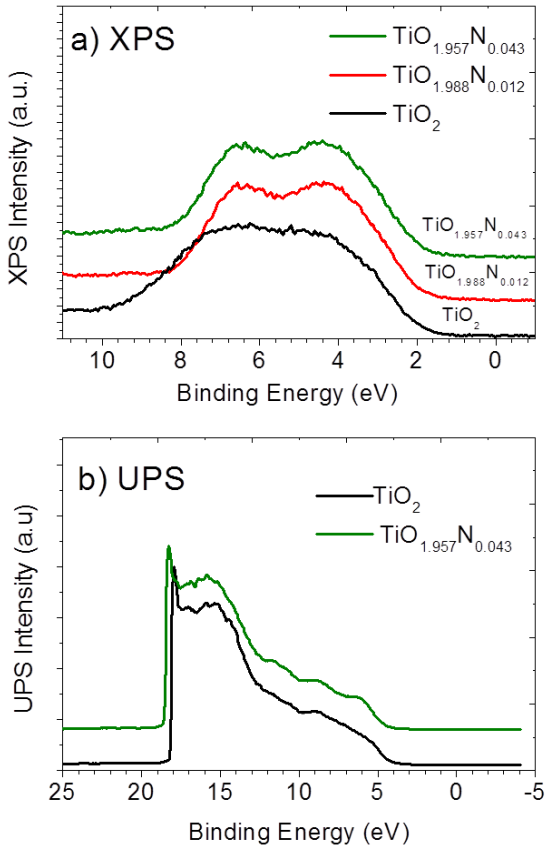

Figure 2.8. (a) XPS valence band spectra of the TiO_2, $TiO_{1.988}N_{0.012}$, and $TiO_{1.957}N_{0.043}$ samples and (b) UPS spectra of the TiO_2 and $TiO_{1.957}N_{0.043}$ samples. The UPS spectra were calibrated versus the Fermi edge of a polycrystalline Au foil.

CONCLUSIONS

In summary, we report a hydrothermal synthesis route that allows direct growth of vertically aligned, densely packed, single crystalline rutile TiO_2 nanowire arrays with exceptionally small feature sizes of ~ 5 nm and lengths up to 4.4 μm on top of FTO substrates. We also report the synthesis of visible-light-active nitrogen-modified TiO_2 photoanodes *via* the nitridation of hydrothermally synthesized TiO_2 nanowire arrays in NH_3 at relatively low temperature. We also demonstrate that utilization of a cobalt co-catalyst can significantly enhance the PEC performance of our N-modified TiO_2

nanowire arrays. With a cobalt water oxidation co-catalyst, the quantum yields of our N-modified TiO_2 samples increase with increasing substitutional nitrogen concentration, and are higher than the quantum yields of unmodified TiO_2 samples both in the UV and visible light regions.

REFERENCES

1. Fujishima, A.; Honda, K. *Nature* **1972**, 238, (5358), 37-38.
2. Linsebigler, A. L.; Lu, G.; Yates, J. T. *Chem. Rev.* **1995**, 95, (3), 735-758.
3. Chen, X.; Mao, S. S. *Chem. Rev.* **2007**, 107, (7), 2891-2959.
4. Asahi, R.; Morikawa, T.; Ohwaki, T.; Aoki, K.; Taga, Y. *Science* **2001**, 293, (5528), 269-271.
5. Park, J. H.; Kim, S.; Bard, A. J. *Nano Lett.* **2005**, 6, (1), 24-28.
6. Zhu, W.; Qiu, X.; Iancu, V.; Chen, X.-Q.; Pan, H.; Wang, W.; Dimitrijevic, N. M.; Rajh, T.; Meyer, H. M.; Paranthaman, M. P.; Stocks, G. M.; Weitering, H. H.; Gu, B.; Eres, G.; Zhang, Z. *Phys. Rev. Lett.* **2009**, 103, (22), 226401.
7. Yin, W.-J.; Tang, H.; Wei, S.-H.; Al-Jassim, M. M.; Turner, J.; Yan, Y. *Phys. Rev.* B **2010**, 82, (4), 045106.
8. Salvador, P. *J. Appl. Phys.* **1984**, 55, (8), 2977-2985.
9. Abe, R.; Higashi, M.; Domen, K. *J. Am. Chem. Soc.* **2010**, 132, (34), 11828-11829.
10. Kay, A.; Cesar, I.; GrÃ¤tzel, M. *J. Am. Chem. Soc.* **2006**, 128, (49), 15714-15721.
11. Kanan, M. W.; Nocera, D. G. *Science* **2008**, 321, (5892), 1072-1075.
12. Burda, C.; Lou, Y.; Chen, X.; Samia, A. C. S.; Stout, J.; Gole, J. L. *Nano Lett.* 2003, 3, (8), 1049-1051.
13. Beranek, R.; Neumann, B.; Sakthivel, S.; Janczarek, M.; Dittrich, T.; Tributsch, H.; Kisch, H. *Chem. Phys.* **2007**, 339, (1-3), 11-19.
14. Nakamura, R.; Tanaka, T.; Nakato, Y. *J. Phys. Chem.* B **2004**, 108, (30), 10617-10620.
15. Torres, G. R.; Lindgren, T.; Lu, J.; Granqvist, C. G.; Lindquist, S. E. J *J. Phys. Chem.* B **2004**, 108, (19), 5995-6003.
16. Batzill, M.; Morales, E. H.; Diebold, U. *Phys. Rev. Lett.* **2006**, 96, (2), 026103.
17. Serpone, N. *J. Phys. Chem.* B **2006**, 110, (48), 24287-24293.
18. Emeline, A. V.; Sheremetyeva, N. V.; Khomchenko, N. V.; Ryabchuk, V. K.; Serpone, N. *J. Phys. Chem.* C **2007**, 111, (30), 11456-11462.
19. Feng, X.; Shankar, K.; Varghese, O. K.; Paulose, M.; Latempa, T. J.; Grimes, C. A. *Nano Lett.* **2008**, 8, (11), 3781-3786.
20. Meinan, L.; Hongxia, W.; Cheng, Y.; Geoffrey, W.; John, B. *Appl. Phys. Lett.* **2011**, 98, 133113.

21. Shao, F.; Sun, J.; Gao, L.; Yang, S.; Luo, J. *ACS Appl. Mater. Interfaces* **2011**, 3, (6), 2148-2153.

22. Wang, J.; Tafen, D. N.; Lewis, J. P.; Hong, Z.; Manivannan, A.; Zhi, M.; Li, M.; Wu, N. *J. Am. Chem. Soc.* **2009**, 131, (34), 12290-12297.

23. Chen, X.; Burda, C. *J. Am. Chem. Soc.* **2008**, 130, (15), 5018-5019.

24. Fujishima, A.; Zhang, X. T.; Tryk, D. A. *Surf. Sci. Rep.* **2008**, 63, (12), 515-582.

25. Irie, H.; Watanabe, Y.; Hashimoto, K. *J. Phys. Chem.* B **2003**, 107, (23), 5483-5486.

26. Takahashi, I.; Payne, D. J.; Palgrave, R. G.; Egdell, R. G. *Chem. Phys. Lett.* **2008**, 454, (4-6), 314-317.

27. Diwald, O.; Thompson, T. L.; Zubkov, T.; Walck, S. D.; Yates, J. T. *J. Phys. Chem.* B **2004**, 108, (19), 6004-6008.

28. Miyauchi, M.; Ikezawa, A.; Tobimatsu, H.; Irie, H.; Hashimoto, K. *Phys. Chem. Chem. Phys.* **2004**, 6, (4), 865-870.

29. Irie, H.; Washizuka, S.; Yoshino, N.; Hashimoto, K. *Chem. Commun.* **2003**, (11), 1298-1299.

30. Gai, Y.; Li, J.; Li, S.-S.; Xia, J.-B.; Wei, S.-H. *Phys. Rev. Lett.* **2009**, 102, (3), 036402.

31. Lindgren, T.; Lu, J.; Hoel, A.; Granqvist, C. G.; Torres, G. R.; Lindquist, S. E. *Sol. Energy Mater. Sol. Cells* **2004**, 84, (1-4), 145-157.

32. Tang, J.; Cowan, A. J.; Durrant, J. R.; Klug, D. R. *J. Phys. Chem.* C **2011**, 115, (7), 3143-3150.

33. Ohsawa, T.; Henderson, M. A.; Chambers, S. A. *J. Phys. Chem.* C **2010**, 114, (14), 6595-6601.

34. Asahi, R.; Taga, Y.; Mannstadt, W.; Freeman, A. J. *Phys. Rev. B* **2000**, 61, (11), 7459.

35. Ye, H.; Park, H. S.; Bard, A. J. *J. Phys. Chem.* C **2011**, 115, (25), 12464-12470.

Chapter 3: Enhancing Visible Light Photo-Oxidation of Water with TiO_2 Nanowire Arrays via Co-treatment with H_2 and NH_3: Synergistic Effects between Ti^{3+} and N

INTRODUCTION

The search for cheap, efficient, and stable photocatalysts for solar hydrogen production from water splitting has been an increasingly active field since Honda and Fujishima's discovery of water photo-oxidation on a TiO_2 photoanode under ultraviolet (UV) light.[1] To date, TiO_2 is still one of the most studied photocatalyst materials due to its abundance, low-cost, low-toxicity, superior photo-stability, and high intrinsic catalytic activity under UV illumination.[2-5] However, the photo-conversion efficiency of TiO_2 is limited to less than 2.2 % under AM 1.5 global solar illumination due to its large band gap energy (3.0 eV for rutile and 3.2 eV for anatase).[6] The generally-accepted benchmark for solar-to-hydrogen efficiency under AM 1.5 global illumination is 10% for practical implementation.[7] Therefore, extending the working spectrum of TiO_2-based materials to include more of the visible light region, which composes ~ 45% of the total energy of the solar spectrum, has been of great interest.

Recent efforts have focused on modifying the valence band of TiO_2 by incorporating nonmetal ions such as C,[8] S,[9] and N[4,10]. The p states of the nonmetal foreign ions (N, S, or C) normally form impurity states above the valence band or hybridize with O 2p states (composing most of the valence band for TiO_2) thus upshifting the valence band edge of TiO_2.[3] Among nonmetal elements, N doping has been widely investigated and some success has been achieved in extending the working spectrum of TiO_2 toward the visible light range.[4] Modifying TiO_2 by hydrogen has also received attention recently.[11,12] Wang

et al. demonstrated that annealing rutile TiO_2 NW arrays in an H_2 atmosphere creates oxygen vacancy sites thus forming donor states below the conduction band.[11] This improves light absorption and charge transport similar to n-type doping, thus enhancing water oxidation performance. Chen *et al.* reported a hydrogenation method to produce disorder in nanophase TiO_2, which significantly enhances visible light absorption.[12] Despite the interest in the effects of nitrogen doping and hydrogen modification, there are only a few studies on the synergistic effects of H and N co-doping on the photocatalytic activity of TiO_2 materials.[13-17] To our knowledge, there is no report on the enhancement of visible light water photo-oxidation of TiO_2 due to the cotreatment with H_2 and NH_3 at high temperature. Diwald *et al.* prepared H, N-codoped TiO_2 material that is photoactive for Ag deposition under irradiation by photons of 2.4 eV by annealing rutile TiO_2 (110) in NH_3 at 870 K. The treatment introduced two species of N into the TiO_2 lattice: substituitonal and interstitial N species.[17] The authors claimed that the co-doping effect between the interstitial species and hydrogen is responsible for the enhancement in the visible light activity. The authors, however, did not consider the effects of Ti^{3+} formation. In fact, under this nitridation condition, Ti^{3+} formation is expected and can be more readily detected using bulk characterization techniques such as EPR rather than by conventional surface characterization techniques such as X-ray Photoemission Spectroscopy (XPS) due to the instability of the surface Ti^{3+} in air or water.

In addition to enhancing optical absorption, it is equally important to optimize the photogenerated electron/hole separation characteristics. Vertically oriented nano-columnar structures are considered to be very effective structures for

photoelectrochemical (PEC) water splitting applications.[18,19] These structures permit significant light absorption depths while still enhancing the charge separation by providing high electrode/electrolyte interface areas and shortening the minority charge carrier transport distance to the electrolyte. We have recently reported the hydrothermal synthesis of vertically-aligned ultrafine single crystalline rutile TiO_2 NW arrays with an average cross sectional dimension of ~ 5 nm.[10] Upon nitridation in a NH_3 flow at 500 ^oC, the optical absorption and the PEC response spectrum extended from ~ 420 nm to ~ 550 nm. In the present study, we demonstrate synergistic effects of hydrogenation and nitridation that further extend the active spectrum of the TiO_2 NW arrays to ~ 570 nm. To our knowledge, we are the first to demonstrate the enhancement of visible light water photo-oxidation reactivity of TiO_2 material due to hydrogenation and nitridation co-treatment.

EXPERIMENTAL METHODS

Materials. All chemicals were purchased and used without further purification including titanium (IV) isopropoxide (TTIP) (98+ %, Acros Organics), HCl (ACS Reagent Grade 36.5-38%, MP), n-hexane (Extra dry, 96+%, Acros Organics), titanium (IV) chloride, (99.0+ %, Alfa Aesar), gas mixture of H_2 and Ar (5% H_2 in Ar, Matheson Tri-gas), and ammonia (99.99 %, Matheson Tri-gas).

Hydrothermal Synthesis. Fluorine-doped Tin Oxide (FTO) coated glass substrates were first cleaned by sonication in a mixture of ethanol and water for 30 minutes, subsequently rinsed by deionized (DI) water, and finally dried in an air stream. The FTO substrates were then seeded with a thin layer of TiO_2 before growing the

nanowire arrays by soaking in 0.025M $TiCl_4$ in n-hexane for 30 minutes. They were then taken out, rinsed by ethanol, and finally annealed in air at 500 ^oC for 30 minutes. The seeded FTO substrates were then placed on the bottom of a Teflon lined autoclave (125 mL, Parr Instrument), containing 50 mL n-hexane, 5 mL HCl, and 5 mL of titanium (IV) isopropoxide. The hydrothermal synthesis was conducted at 150 ^oC for 5 hours. After the reaction was completed and the autoclave naturally cooled down to room temperature, the TiO_2 nanowire films were taken out and cleaned by rinsing with copious amount of ethanol and water. The TiO_2 nanowire array thickness was measured as 2.6 μm ± 0.27 μm by Scanning Electron Microscopy.

Thermal treatments. To remove the contaminants and increase the crystallinity, the pristine TiO_2 nanowire sample was prepared by annealing the as-hydrothermally synthesized sample in air at 500 ^oC for 1 hour in a box oven. The hydrogen treatment and nitridation process were performed using a tube furnace (MTI, OTF-1200x-80). The tube was first evacuated until the pressure inside the tube was below 1 Torr. The tube was then filled with desired gases (H_2/Ar or NH_3) to atmospheric pressure. The flows of H_2/Ar (100 mL/minute) and NH_3 (100 mL/minute) were controlled by gas flow controllers during annealing time. The exhaust line was bubbled through a cup of water (the exhaust line was kept ~ 5 cm below the water surface). The hydrogen-treated sample (H-TiO2) and the nitrided sample (N-TiO_2) were prepared by annealing the as-synthesized samples at 500 ^oC in H_2/Ar for 1 hour and NH_3 for 2 hours respectively. The co-treated sample (H, N-TiO_2) were prepared by first annealing in H_2/Ar at 500 ^oC for 1 hour, following by annealing in NH_3 at 500 ^oC for 2 hours.

Material Characterization. Scanning electron microscopy (SEM) was performed on a Zeiss field-emission SEM using a 10 kV focus voltage. Transmission electron microscopy (TEM) was performed on a JEOL 2010F field-emission TEM using

a 200 kV focus voltage. Grazing incidence X-ray diffraction (GIXRD) patterns were collected with a Bruker D8 diffractometer. The transmittance spectra were collected using a Cary 500 UV-vis-NIR spectrophotometer attached to a Labsphere DRA-CA-5500 integrating sphere. X-ray photoelectron spectroscopy (XPS) was performed on a Kratos Axis x-ray photoelectron spectrometer with scanning step of 0.1 eV and dwell time of 4 second/step. The binding energy was calibrated using the C 1s photoelectron peak at 284.6 eV as a reference. The elemental percentages were calculated from XPS spectra using the CasaXPS computer program with specific relative sensitivity factors for the Kratos Axis XPS (Ti 2p: 2.001, O 1s: 0.78, and N 1s: 0.48). The electron paramagnetic resonance (EPR) spectra were collected at 86 K using a Bruker EMX-CW EPR spectrometer operating at the X-band frequency. The samples were first loaded in quartz glass tubes covered by aluminum foil, then baked out in an oven at 60 ^{o}C for 24 hours before EPR measurements. Five (5) scans were added for each spectrum with following scan parameters: microwave frequency = 9.47 GHz; modulation amplitude = 1 G; modulation frequency = 100 kHz; and non-saturating microwave power = 20 mW.

Electrochemical and Photoelectrochemical (PEC) Characterizations.

The PEC measurements were performed using a three-electrode electrochemical cell with the FTO supported nanowire arrays as the working electrode, a Ag/AgCl (saturated KCl) reference electrode, a platinum wire counter electrode, and 1 M KOH electrolyte (pH = 13.5). The working electrode with exposed area of 0.205 cm^2 was illuminated from the back side (through the FTO substrate – TiO_2 nanowire interface) by a solar simulator (Newport, Model 9600, 150 W xenon lamp) equipped with an AM 1.5 G filter (Newport, Model 81094). The light intensity was measured as 100 mW/cm^2 using a thermopile detector with the spectrum response from 0.19 to 10.6 μm (Newport, 818P-

020-12). A CHI 660D electrochemical station was used for linear sweep voltammetry (I-V) and chronoamperometry (I-t) measurements.

Incident photon to current conversion efficiencies (IPCEs) were calculated from chronoamperometry measurements using a motorized monochrometer (Oriel Cornerstone 130 1/8 m). The monochrometer slit size was adjusted to 0.75 mm x 2 mm providing monochromatic wavelengths with a bandwidth of ~ 5 nm and a power density which could be adjusted from 8 to 4000 $\mu W/cm^2$ for wavelengths from 320 to 600 nm. A typical light power density spectrum used for IPCE can be found in Figure 3.1.

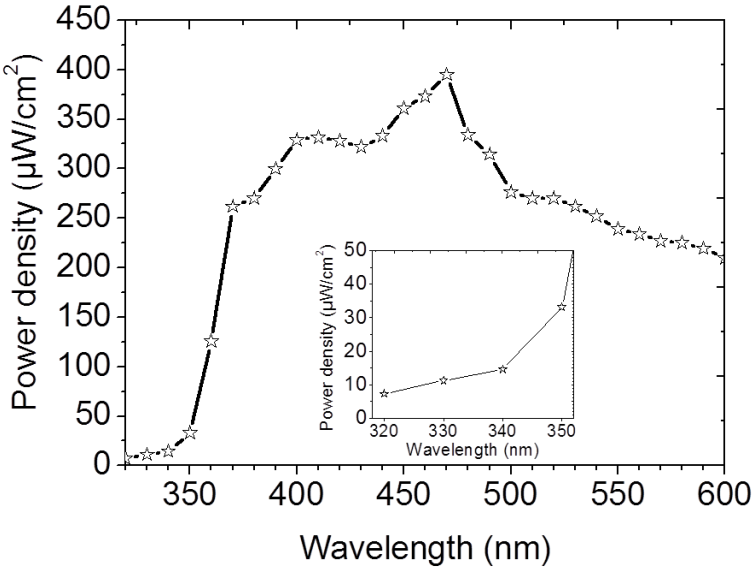

Figure 3.1. A typical incident light power density spectrum (from 320 nm - 600nm) used for the IPCE measurements. The inset shows the incidence power density spectrum from 320 nm -350nm.

Light power was measured using a handheld optical power meter with a UV enhanced silicon photo-detector (Newport). IPCE values were calculated using the following equation:

$$IPCE(\lambda) = \frac{1240\, j_p(\lambda)}{\lambda\, E_\lambda(\lambda)} \qquad (1)$$

where $j_p(\lambda)$ is the measured photocurrent density (mA/cm^2) and $E_\lambda(\lambda)$ is the incident light power density (mW/cm^2) for each wavelength, λ (nm).

The measured potentials *vs.* the Ag/AgCl were converted to the reversible hydrogen electrode (RHE) scale *via* the Nernst equation

$$E_{RHE} = E_{Ag/AgCl} + 0.059\ pH + E^o_{Ag/AgCl} \quad (2)$$

where E_{RHE} is the converted potential vs. RHE, $E_{Ag/AgCl}$ is the experimental potential measured against Ag/AgCl reference electrode, and $E^o_{Ag/AgCl}$ = 0.1976 V at 25 ^oC.

RESULTS AND DISCUSSION

The TiO_2 photoelectrodes were prepared via two steps: (1) hydrothermal synthesis followed by (2) thermal treatments. The single crystalline rutile TiO_2 NW arrays with a thickness of 2.60 ± 0.27 μm were hydrothermally prepared on Fluorine-doped Tin Oxide (FTO) substrates. The NW arrays were further modified by annealing at 500 ^oC (i) in air for 1 hour (denoted as TiO_2), (ii) in NH_3 for 2 hours (N-TiO_2), (iii) in a mixture of H_2 and Ar (5 % of H_2) for 1 hour (H-TiO_2), and (iv) in the a mixture of H_2 and Ar for 1 hour followed by annealing in NH_3 for 2 hours (H, N-TiO_2).

The X-ray diffraction data (XRD) (Figure 3.2a) confirms that all films are of rutile phase and no additional phase was detected upon thermal treatment. However, the thermal treatments have a profound effect on the visual appearance and morphology of the NW arrays. The white color of the pristine TiO_2 film did not change after hydrogen

treatment; however, it turned green after nitridation, and dark green after both treatments (Figure 3.2b).

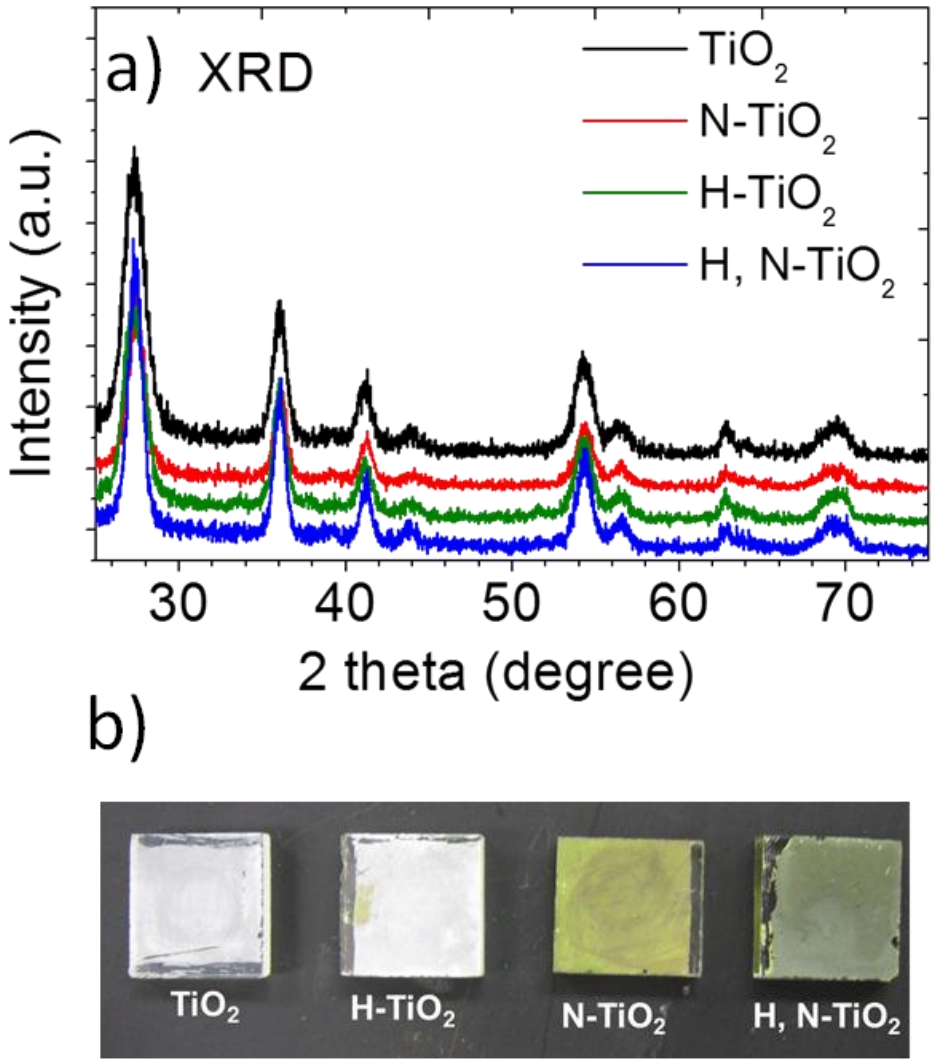

Figure 3.2. (a) Grazing incidence XRD patterns and (b) digital images of TiO_2, N-TiO_2, H-TiO_2, and H, N-TiO_2.

In addition the shape and size of the nanowires changed with each treatment as can be seen by the SEM images in Figure 3.3.

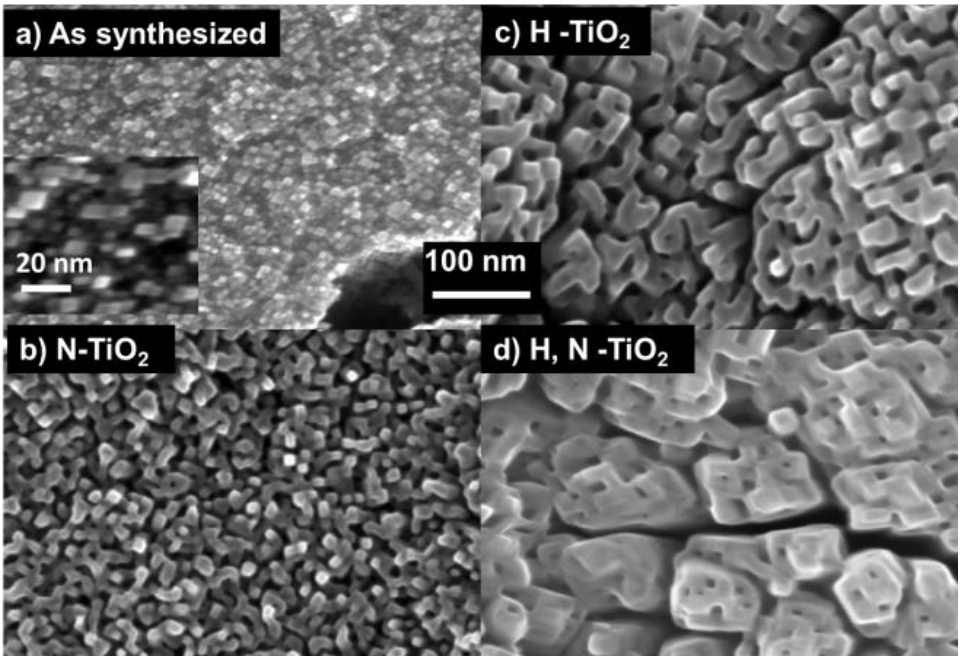

Figure 3.3. Scanning Electron Microscopy (SEM) images of (a) as-synthesized TiO_2 (inset shows higher magnification view), and films annealed at 500 ^{o}C in (b) NH_3, (c) H_2, and (d) H_2 and then NH_3.

Upon treatment, the cross-section of the NW becomes larger due to the sintering of the small wires. Increases in the interplanar d-spacing for the (101) crystal plane due to co-treatment observed by Transmission Electron Microscopy (TEM) (Figure 3.4) indicate lattice expansion as a result of N incorporation.

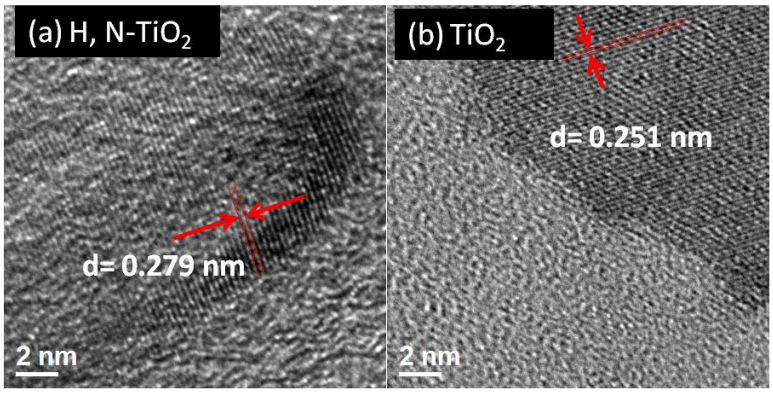

Figure 3.4. High resolution TEM images of (a) H, N-TiO_2 and (b) TiO_2 samples.

We employed X-ray Photoemission Spectroscopy (XPS) to investigate the chemical composition of the surface (Figure 3.5). The N 1s peak at 399.8 eV of the TiO_2 sample is assigned to molecular N_2 adsorbed on the surface.[4]

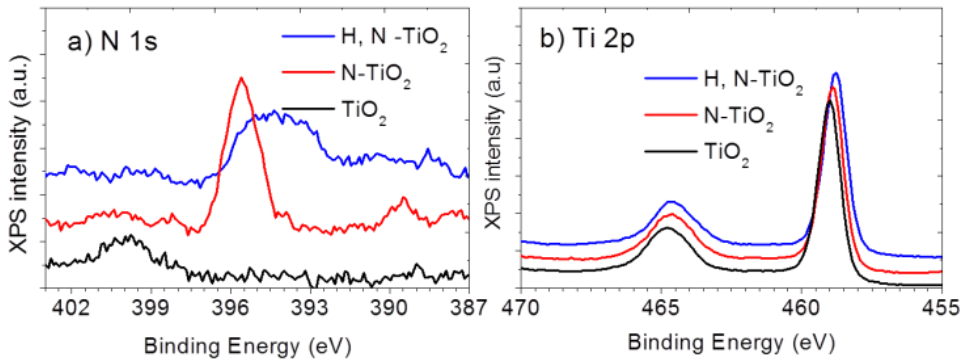

Figure3.5. XPS spectra of the TiO_2, N-TiO_2, and H, N-TiO_2 NW arrays: (a) Core N 1s and (b) Core Ti 2p.

The N 1s feature at 395.6 eV of the N-TiO_2 sample and the feature at 394.4 eV of the H, N-TiO_2 sample are assigned to substitutional β-N (N^{3-}) species which is considered

responsible for enhancing the visible light activity of the N-doped materials.[4,20] It is interesting that the N 1s feature of the H, N-TiO_2 sample is broader and shifts to a lower binding energy compared with that of the N-TiO_2. We will discuss these phenomena in more detail later. The substitutional N concentrations are calculated as 5.6 atomic % for N-TiO_2 and 3.5 atomic % for H, N-TiO_2, corresponding to x values of 0.20 and 0.12 (x in $TiO_{2-x}N_x$), respectively. The substitutional N concentration in our N-modified TiO_2 nanowires is considerably higher compared to other N-doped TiO_2 materials prepared via nitridation of TiO_2 at elevated temperature in NH_3 flow.[21] The unique morphology and the ultrafine cross-section of the NW may enhance N diffusion into the TiO_2 lattice.

The Ti 2p3/2 XPS features are observed at 459.20 eV, 458.76 eV, and 458.71 eV for TiO_2, N-TiO_2, and H, N-TiO_2 respectively. These features are all assigned to Ti^{4+}, indicating no Ti^{3+} species exist on the surface (the XPS technique characterizes the top 1 nm-10 nm layer of the material). The presence of Ti^{3+} was further investigated by low temperature electron paramagnetic resonance (EPR) (Figure 3.6). No EPR features appear for a g-value of ~ 2.02 corresponding to O_2^- produced from the reduction of adsorbed O_2 (from air) by surface Ti^{3+} further confirming the absence of surface Ti^{3+}.[22] Surface Ti^{3+} is unstable under illumination in air or in electrolyte as it is easily oxidized by air or dissolved oxygen in water.[23] The strong EPR signal for a g-value of 1.992 for the H, N-TiO_2 sample indicates the presence of Ti^{3+} in the bulk. We also observed a trace amount of Ti^{3+} in the bulk of the N-TiO_2 sample. The intensity of the feature at g-value of 1.981 for the N-TiO_2 sample is two orders of magnitude smaller than the feature at a g of 1.992 for the H, N-TiO_2 sample.

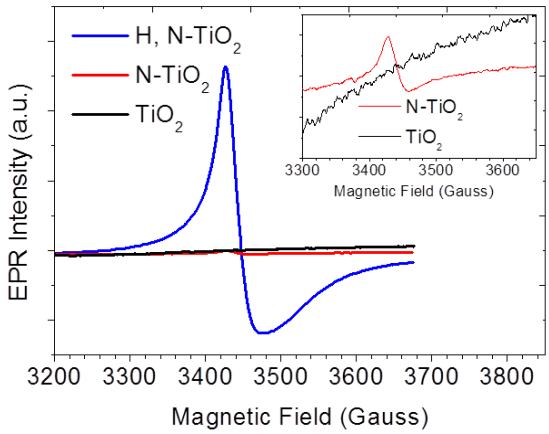

Figure 3.6. EPR spectra recorded at 86 K for TiO_2, N-TiO_2 and H, N-TiO_2 samples. The inset shows magnified view for the EPR spectra of the TiO_2 and N-TiO_2 samples.

Linear sweep voltammetry (scan rate of 5 mV/s) results for the H, N-TiO_2 nanowires are shown in Figure 3.7a. The onset potential for the H, N-TiO_2 sample positively shifts to 0.6 V vs. reversible hydrogen electrode (V_{RHE}) compared with 0.2 V_{RHE} for the pristine TiO_2 sample even though the photocurrent transient onset potentials for the two sample are almost the same, ~ -0.15 V_{RHE} (data not shown). The shift in the constant-illumination onset potential might be due to either a larger band banding requirement for separating electrons and holes because of the material's likely possession of poorer charge-transport properties than pure TiO_2 or slower surface kinetics as a result of hydrogenation and nitridation co-treatment.[10]

The H, N-TiO_2 sample shows remarkable visible light water oxidation performance. The visible light (> 420 nm) current reaches 0.159 mA/cm^2 at 1.23 V *vs.* reversible hydrogen electrode (V_{RHE}) and contributes ~ 41% of the full AM 1.5 G photocurrent. The chronoamperometry (CAM) measurement at 1.23 V_{RHE} (total time of ~ 30 minutes) in

Figure 3.7b indicates the material's high stability. After the test, we observed the formation of bubbles on the film, suggesting the oxygen production from water oxidation. We believe that the formation of oxygen bubbles decreases the electrode/electrolyte contact area, resulting in a slight decrease of 4.6% in the AM 1.5 G photocurrent after 15 minute illumination.

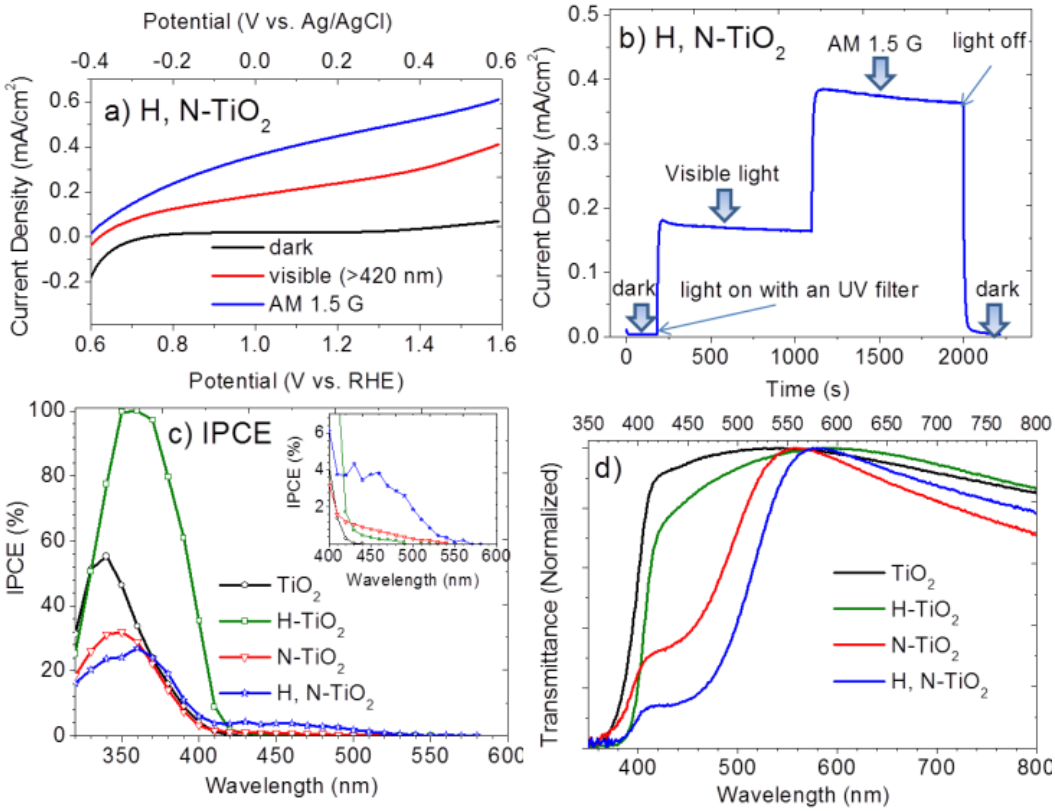

Figure 3.7. (a) and (b) Linear Sweep Voltametry (5 mV/s) and Chronoamperometry at 1.23 V_{RHE} of the H, N-TiO_2 sample, (c) IPCE spectra measured at 1.23 V_{RHE}, and (d) Normalized transmittance spectra. All PEC measurements were performed using a three-electrode electrochemical cell with a Ag/AgCl reference electrode, a Pt wire counter electrode, and 1 M KOH electrolyte. A solar simulator (Oriel 96000) with an AM 1.5 G filter was used as the light source with light intensity of 100 mW/cm^2 measured by a thermopile detector (Newport, 818P-020-12). A UV filter that blocks all wavelengths < 420 nm was used for visible light experiments.

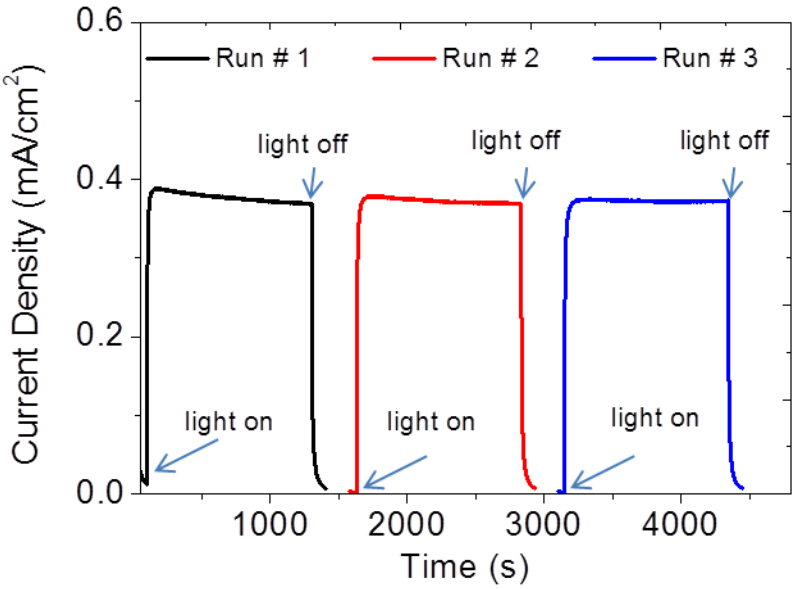

Figure 3.8. Chronoamperometry (CAM) measurement at 1.23 V_{RHE} of the H, N-TiO2 sample. The measurement was performed using a three-electrode electrochemical cell with a Ag/AgCl reference electrode, a Pt wire counter electrode, and 1 M KOH electrolyte. A solar simulator (Oriel 96000) coupling with an AM 1.5 G filter was used as the light source with light intensity of 100 mW/cm2 measured by a thermopile detector (Newport, 818P-020-12). The measurement was performed in 3 sequential runs: run #1, run #2, and run #3. After each run, we used a pipet to flush out bubbles forming on the H, N-TiO_2 photoanode.

Figure 3.8 shows 3 runs of CAM measurement between which we used a pipet to flush out bubbles on the sample. The photocurrents were almost fully restored, thus supporting our hypothesis. In fact, after repeated testing for 5 months (the sample was stored in open air) the film still retains this performance.

Figures 3.7c and 3.7d show the incident photon-to-current efficiency (IPCE) spectra and the normalized UV-vis transmittance spectra (the raw data are included in Figure

3.9). The absorption edge of the H, N-TiO_2 sample shifts ~ 20 nm to the longer wavelength region compared to the N-doped TiO_2 NW sample. The decrease in the transmittance for all samples at larger wavelengths than 570 nm is due to the light absorption of FTO substrates in this region which is confirmed by the UV-vis transmittance of FTO in Figure 3.9.

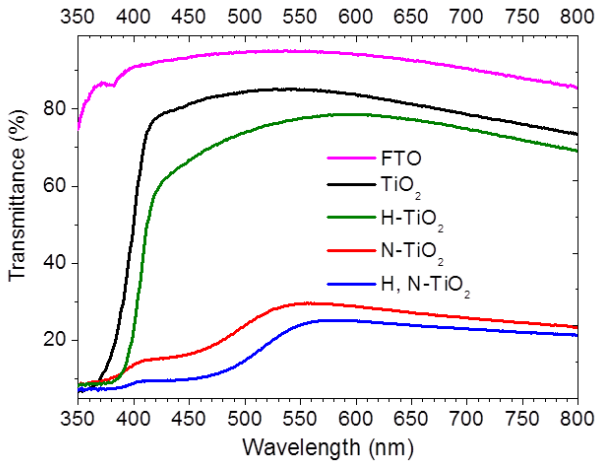

Figure 3.9. Raw data of the UV-vis transmittance spectra of FTO substrate, TiO_2, H-TiO_2, N-TiO_2, and H, N-TiO_2 samples

The IPCE spectra fit well with the transmittance spectra, confirming that the active spectra of the H, N-TiO_2 sample extends to ~ 570 nm. The photocurrent obtained by integrating the calculated IPCE multiplied by the AM 1.5 G solar energy flux[24] over the range of 420 nm-570 nm is 0.159 mA/cm^2, contributing to ~ 35% of the total integrated AM 1.5 G photocurrent (0.454 mA/cm^2). The small discrepancy between the full AM 1.5 G photocurrent obtained by the CAM measurement (0.388 mA/cm^2) and the integration method (0.454 mA/cm^2) might be due to the difference between the simulated sunlight

(Xenon lamp + AM 1.5 filter) and standard AM 1.5. The absence of a photo response in the IPCE of the untreated TiO_2 NW arrays indicates that the absorption tails from 420 nm - 500 nm in the transmittance spectra of the untreated TiO_2 sample is due to light scattering from the nanostructures. The H-TiO_2 sample shows significant improvement in the PEC performance in the UV region due to the enhancement in the electron conductivity.[11] Its IPCE spectrum, however, just shows a weak response from visible light (420 nm - ~ 500 nm), mainly due to the photoelectrochemically inactive transition from the valence band to hydrogenation-induced oxygen vacancy states.[11]

As mentioned in our previous study, incorporating N into the rutile TiO_2 NW arrays modifies the valence band structure, thus extending the working spectrum to ~ 550 nm. In the present study, we demonstrate that pre-hydrogenation significantly increases the bulk Ti^{3+} concentration and the interaction between Ti^{3+} and N-doping increase the visible light absorption and shifts the absorption edge further to the longer wavelength region (~ 570 nm) compared to individual doping with Ti^{3+} or N. Employing EPR, Livraghi *et al.* detected paramagnetic bulk species of N ($N_b^{\bullet}$) at a g-value of 2.005, which formed localized states within the band gap of their N-doped TiO_2.[25] The authors proposed a reversible electron transfer between the $N_b^{\bullet}$ and Ti^{3+} centers forming the diamagnectic bulk species of N (N_b^{-}) and Ti^{4+}. A similar phenomenon is also observed by Napoli et al. when they exposed a pre-reduced TiO_2 to a N plasma.[26] The N-induced states of N_b^{-} species are higher in energy than that of corresponding $N_b^{\bullet}$ species due to greater Coulombic repulsion. Di Valentin *et al.* prepared F, N-codoped TiO_2 samples and reported an increase in Ti^{3+} concentration with increasing F doping level. The authors

also claimed that the formation of N_b^- is more favorable with an increase in Ti^{3+} and that is the key for the improvement in the visible light photocatalytic activity.[27] We did not detect any paramagnetic species other than Ti^{3+} in our H, N-TiO_2 sample. We, however, can observe the interactions of Ti^{3+} and substitutional N in the H, N-TiO_2 sample in the core N 1s XPS spectra (Figure 3.2a). The broadening and shift to the lower binding energy of the XPS N 1s feature compared with that of the N-TiO_2 sample indicates lower oxidation states of the substitutional N in the H, N-TiO_2 sample which might be due to electron transfer from Ti^{3+}. Due to the Columbic repulsion, the lower oxidation states of N in the H, N-TiO_2 sample have higher energy than that of the N-TiO_2 sample, thus enabling excitation with photons of longer wavelengths. The proposed interaction between Ti^{3+} and N that modifies the electronic band structure of TiO_2 is illustrated in Figure 3.10.

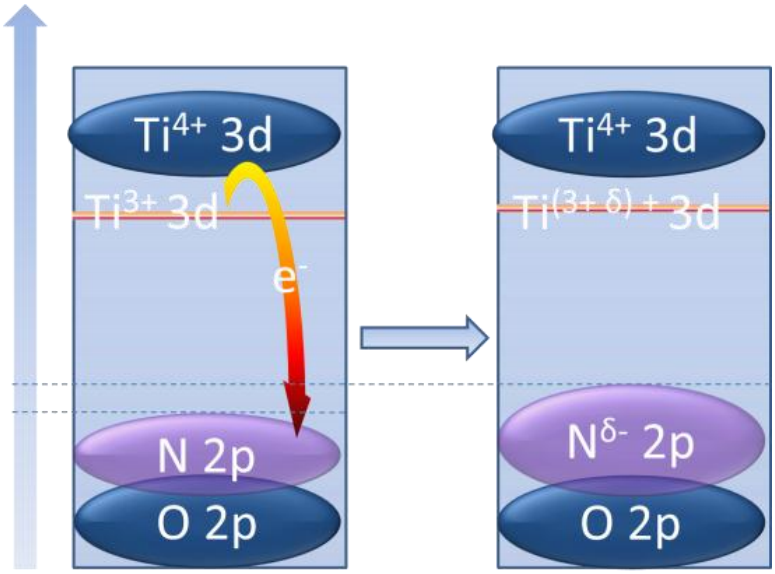

Figure 3.10. Proposed mechanism for the interaction between Ti^{3+} and substitutional N.

CONCLUSIONS

In summary, we report a synergistic effect between hydrogen and nitridation co-treatment that significantly enhances the water photo-oxidation of rutile TiO_2 NW arrays under visible light. The photocurrent of the H, N-TiO_2 sample under visible light (>420 nm) illumination contributes ~ 41 % of the simulated AM 1.5 G photocurrent. The IPCE and UV-vis transmittance spectroscopy reveal that the working spectrum of the H, N-TiO_2 sample extends to ~570 nm compared with ~ 550 nm for the N-TiO_2 and ~ 420 nm for pristine TiO_2. The hydrogenation process increases the bulk Ti^{3+} concentration in TiO_2. We speculate that the interactions between substitutional N and Ti^{3+} are responsible for the enhancement in the water oxidation performance under visible light illumination.

REFERENCES

(1) Fujishima, A.; Honda, K. *Nature* **1972**, *238*, 37-38.

(2) Linsebigler, A. L.; Lu, G.; Yates, J. T. *Chem. Rev.* **1995**, *95*, 735-758.

(3) Chen, X.; Mao, S. S. *Chem. Rev.* **2007**, *107*, 2891-2959.

(4) Asahi, R.; Morikawa, T.; Ohwaki, T.; Aoki, K.; Taga, Y. *Science* **2001**, *293*, 269-271.

(5) Leary, R.; Westwood, A. *Carbon* **2011**, *49*, 741-772.

(6) Murphy, A. B.; Barnes, P. R. F.; Randeniya, L. K.; Plumb, I. C.; Grey, I. E.; Horne, M. D.; Glasscock, J. A. *Int. J. Hydrogen Energy* **2006**, *31*, 1999-2017.

(7) Bard, A. J.; Fox, M. A. *Acc. Chem. Res.* **1995**, *28*, 141-145.

(8) Park, J. H.; Kim, S.; Bard, A. J. *Nano Lett.* **2006**, *6*, 24-28.

(9) Umebayashi, T.; Yamaki, T.; Itoh, H.; Asai, K. *Appl. Phys. Lett.* **2002**, *81*, 454-456.

(10) Hoang, S.; Guo, S.; Hahn, N. T.; Bard, A. J.; Mullins, C. B. *Nano Lett*. **2012**, *12*, 26-32.

(11) Wang, G.; Wang, H.; Ling, Y.; Tang, Y.; Yang, X.; Fitzmorris, R. C.; Wang, C.; Zhang, J. Z.; Li, Y. *Nano Lett.* **2011**, *11*, 3026-3033.

(12) Chen, X.; Liu, L.; Yu, P. Y.; Mao, S. S. *Science* **2011**, *331*, 746-750.

(13) Mi, L.; Zhang, Y.; Wang, P. N. *Chem. Phys. Lett.* **2008**, *458*, 341-345.

(14) Russo, S. P.; Grey, I. E.; Wilson, N. C. *J. Phys. Chem. C* **2008**, *112*, 7653-7664.

(15) Pan, H.; Zhang, Y.-W.; Shenoy, V. B.; Gao, H. *J. Phys. Chem. C* **2011**, *115*, 12224-12231.

(16) Lan, M.; Peng, X.; Hong, S.; Pei-Nan, W.; Weidian, S. *Applied Physics Letters* **2007**, *90*, 171909.

(17) Diwald, O.; Thompson, T. L.; Zubkov, T.; Walck, S. D.; Yates, J. T. *J. Phys. Chem. B* **2004**, *108*, 6004-6008.

(18) Hahn, N. T.; Ye, H.; Flaherty, D. W.; Bard, A. J.; Mullins, C. B. *ACS Nano* **2010**, *4*, 1977-1986.

(19) van de Krol, R.; Liang, Y. Q.; Schoonman, J. *J. Mat. Chem.* **2008**, *18*, 2311-2320.

(20) Takahashi, I.; Payne, D. J.; Palgrave, R. G.; Egdell, R. G. *Chem. Phys. Lett.* **2008**, *454*, 314-317.

(21) Wang, J.; Tafen, D. N.; Lewis, J. P.; Hong, Z.; Manivannan, A.; Zhi, M.; Li, M.; Wu, N. *J. Am. Chem. Soc.* **2009**, *131*, 12290-12297.

(22) Anpo, M.; Che, M.; Fubini, B.; Garrone, E.; Giamello, E.; Paganini, M. *Top. Catal.* **1999**, *8*, 189-198.

(23) Teleki, A.; Pratsinis, S. E. *Phys. Chem. Chem. Phys.* **2009**, *11*, 3742-3747.

(24) http://rredc.nrel.gov/solar/spectra/am1.5/

(25) Livraghi, S.; Paganini, M. C.; Giamello, E.; Selloni, A.; Di Valentin, C.; Pacchioni, G. *J. Am. Chem. Soc.* **2006**, *128*, 15666-15671.

(26) Napoli, F.; Chiesa, M.; Livraghi, S.; Giamello, E.; Agnoli, S.; Granozzi, G.; Pacchioni, G.; Di Valentin, C. *Chem. Phys. Lett.* **2009**, *477*, 135-138.

(27) Di Valentin, C.; Finazzi, E.; Pacchioni, G.; Selloni, A.; Livraghi, S.; Czoska, A. M.; Paganini, M. C.; Giamello, E. *Chem. Mat.* **2008**, *20*, 3706-3714.

Chapter 4: Co-incorporation of N and Ta into TiO_2 Nanowires for Visible-light Driven Photoelectrochemical Water Oxidation

INTRODUCTION

Titanium dioxide (TiO_2) is well known for PEC water splitting due to its abundance, photostability in aqueous solutions, and strong photocatalytic activity.[1-6] However, due to its large band gap (~3.2 eV), TiO_2 can only utilize ultraviolet (UV) photons that contribute ~ 5% of the total energy of the solar spectrum.[6-9] There have been numerous investigations regarding the band structure engineering and band gap narrowing of TiO_2 in order to shift its absorption spectrum to visible light, which represents a greater portion of the energy in the solar spectrum.[1,5,10-13] For spontaneous photoelectrochemical (PEC) splitting of water without an applied bias, the band edges of the semiconductors must straddle the thermodynamic water redox potentials.[1,12] The band edge alignments of TiO_2 satisfy this requirement in which the conduction band minimum (CBM) is ~ 0.3 – 0.4 eV more negative than the hydrogen production potential, whereas the valence band maximum (VBM) is far below (~ 1.6 eV more positive) the oxygen production potential.[1] Ideally, for efficient solar water splitting without bias, the CBM of TiO_2 should remain as is or slightly shift closer to the vacuum level (more negative on the electrochemical scale) and the valence band maximum should also shift in the same direction so that the band gap reduces to ~ 2 eV accordingly.[1,10,12]

Monodoping TiO_2 with 3d transitional metals (V[13, 14] and Cr[13]) has gained some success in extending the absorption spectrum to the visible region by introducing a donor level under the conduction band,[14,15] however the decrease in carrier mobility due to the formation of strongly localized d states within the band gap and the existence of a carrier recombination center significantly reduce the photo-induced current.[14-20] Monodoping with anions such as N,[10,21] C,[22] and S[23] has been of interest because the p states of

incorporated anions (N, C, or S) normally create an impurity band above the VBM or hybridization with O 2p states, thus narrowing the band gap and keeping the CBM the same. We have recently reported synthesis of N-modified TiO_2 rutile nanowire arrays with the water photo-oxidation spectrum extending to ~ 520 nm.[21] We also demonstrated that thermal co-treatment of H_2 and NH_3 can further extending the working spectrum of the TiO_2 nanowires to 570 nm due to the interaction of bulk Ti^{3+} and N dopants.[24]

Coincorporation of both metal cations and non-metal anions into TiO_2 has been proposed as a new approach for engineering the band structure.[1,12,25-28] The neutralization of positive and negative charges in the TiO_2 lattice created by coincorporation reduces the charge recombination centers, thus enhancing the photocatalytic activity. Moreover, co-incorporation of metal ions and nonmetal ions can help overcome solubility limits, improve material quality, and enhance optical absorption.[12] There are several theoretical studies demonstrating the enhancement in photocatalytic activity of a Ta and N coincorporation approach over monoincorporation of Ta or N, however there is lack of support from experimental studies [12,25,29-31] which is partly is due to the difficulty in preparing co-incorporated TiO_2 materials. Obata *et al.* reported visible light active Ta, N co-doped TiO_2 thin films prepared *via* radio-frequency magnetron sputtering Ti and mixture of TiO_2 and Ta_2O_5 target, however the quantum yields are quite low (smaller than 0.15% in the visible light spectrum (420-500 nm)) and the enhancement in PEC performance due to codoping effects is not clear since PEC performance is compared between samples with different thicknesses (the Ta, N codoped samples are almost two times thicker than the undoped samples).[30] Additionally, Wang et al. reported preparation of N, F, and Ta tri-doped TiO_2 nanoparticle which are visible light active for photodegradation of Rhodamine B and phenol.[32]

Besides engineering the band structure, it is also very important to enhance the charge transport characteristics of materials. Vertically oriented one dimensional (1D) nanostructures such as nanowires, nanorods, nanotubes *etc*., have been demonstrated to be advantageous over planar geometries because these 1D structures provide comparable penetration depth while still decreasing the diffusion distance of the minority charge carrier (holes for n-type and electrons for p-type semiconductors) to the electrolyte.[33-37]

In the present study, we report the synthesis of Ta-incorporated and N, Ta-coincorporated rutile TiO_2 nanowire arrays and their application for water photo-oxidation. Ta-incorporated TiO_2 nanowire arrays with controllable Ta incorporation levels (from 0.11 to 3.5 atomic %) were prepared *via* a facile solvothermal synthesis. The N, Ta-coincorporated TiO_2 NWs were prepared *via* nitridation of the Ta:TiO_2 NWs under NH_3 flow at a relatively low temperature (500 ^oC). N, Ta:TiO_2 NW samples with the optimum Ta concentration of 0.29 at. % demonstrate significant enhancement in PEC performance with the photocurrent reaching 0.52 mA/cm^2 and 0.18 mA/cm^2 under AM 1.5 G and visible light (>420 nm) illumination, respectively. This compares with 0.26 mA/cm^2 and 0.13 mA/cm^2 for that of N:TiO_2 nanowires, although the active spectrum of the N, Ta:TiO_2 NW sample only extends to ~ 520 nm (2.38 eV), compared to ~ 540 nm (2.30 eV) for that of the N:TiO_2 NW sample. We believe that the enhancement of the N, Ta-coincorporated sample is likely because of fewer recombination centers due to charge compensation effects and suppression of the formation of an amorphous layer on the nanowires during the nitridation process.

EXPERIMENTAL METHODS

Materials. All chemicals were purchased and used without further purification including titanium (IV) isopropoxide (TTIP) (98+ %, Acros Organics), HCl (ACS Reagent Grade 36.5-38%, MP), n-hexane (Extra dry, 96+%, Acros Organics), titanium (IV) chloride, (99.0+ %, Alfa Aesar), Ta precursor solution-Ta (V) isopropoxide (99.9%, 10% w/v in isopropanol/n-hexane, Alfa Aesar), and ammonia (99.99 %, Matheson Tri-gas).

Solvothermal Synthesis. Fluorine-doped Tin Oxide (FTO) coated glass substrates were first cleaned by sonication in a mixture of ethanol and water for 30 minutes, subsequently rinsed by deionized (DI) water, and finally dried in an air stream. The FTO substrates were then seeded with a thin layer of TiO_2 before growing the nanowire arrays by soaking in 0.025M $TiCl_4$ in n-hexane for 30 minutes. They were then taken out, rinsed by ethanol, and finally annealed in air at 500 ^oC for 30 minutes. The seeded FTO substrates were then placed on the bottom of a Teflon lined autoclave (125 mL, Parr Instrument), containing 50 mL n-hexane, 5 mL HCl, 0.5 mL of 0.1 M $TiCl_4$ in n-hexane, 5 mL of titanium (IV) isopropoxide, and various amounts of Ta precursor solution (from 0.25-2.5 mL). The solvothermal synthesis was conducted at 150 ^oC for 10 hours. After the reaction was completed and the autoclave naturally cooled down to room temperature, the TiO_2 and Ta:TiO_2 nanowire films were taken out and cleaned by rinsing with copious amounts of ethanol and water.

Thermal treatments. To remove the contaminants and increase the crystallinity, the pristine TiO_2 and Ta:TiO_2 nanowire samples were prepared by annealing the as-solvothermally synthesized sample in air at 500 ^oC for 2 hours in a box oven. The nitridation process was performed using a tube furnace (MTI, OTF-1200x-80). The tube was first evacuated until the pressure inside the tube was below 1 Torr, and then filled

with NH_3 to atmospheric pressure. The flow of NH_3 (30 mL/minute) was controlled by a gas flow controller during the annealing period. The exhaust line was bubbled through a cup of water (the exhaust line exit was kept ~ 5 cm below the water surface).

Material Characterizations. SEM was performed on a Zeiss field-emission SEM using a 10 kV focus voltage. TEM and HRTEM were performed on a JEOL 2010F field-emission TEM using a 200 kV focus voltage. STEM, EDX line scan profile, and elemental mapping were performed on a Hitachi S-5500 equipped with STEM using 30 kV focus voltage. Grazing incidence X-ray diffraction (GIXRD) patterns were collected with a Bruker D8 diffractometer. The transmittance spectra were collected using a Cary 500 UV-vis-NIR spectrophotometer attached to a Labsphere DRA-CA-5500 integrating sphere. X-ray photoelectron spectroscopy (XPS) was performed on a Kratos Axis x-ray photoelectron spectrometer with scanning step of 0.1 eV and dwell time of 2 seconds/step. The binding energy was calibrated using the C 1s photoelectron peak at 284.5 eV as a reference. The elemental percentages were calculated from XPS spectra using the CasaXPS computer program with specific relative sensitivity factors for the Kratos Axis XPS (Ti 2p: 2.001, O 1s: 0.78, and Ta 4f: 8.62).

Electrochemical and Photoelectrochemical (PEC) Characterizations. The PEC measurements were performed using a three-electrode electrochemical cell with the FTO supported nanowire arrays as the working electrode, a Ag/AgCl (saturated KCl) reference electrode, a platinum wire counter electrode, and 1 M KOH electrolyte (pH = 13.5). The working electrode with exposed area of 0.205 cm^2 was illuminated from the back side (through the FTO substrate – TiO_2, Ta:TiO_2, and N,Ta:TiO_2 nanowires interface) by a solar simulator (Newport, Model 9600, 150 W xenon lamp) equipped with an AM 1.5 G filter (Newport, Model 81094). The light intensity was measured as 100 mW/cm^2 using a thermopile detector with the spectrum response from 0.19 to 10.6 μm

(Newport, 818P-020-12). A CHI 660D electrochemical station was used for linear sweep voltammetry (I-V) and chronoamperometry (I-t) measurements.

Incident photon to current conversion efficiencies (IPCEs) were calculated from chronoamperometry measurements using a motorized monochrometer (Oriel Cornerstone 130 1/8 m). The monochrometer slit size was adjusted to 0.75 mm x 2 mm providing monochromatic wavelengths with a bandwidth of ~ 8 nm and a power density which could be adjusted from 197 to 705 $\mu W/cm^2$ for wavelengths from 320 to 600 nm. A typical light power density spectrum used for IPCE can be found in Figure 4.1. Light power was measured using a handheld optical power meter with a UV enhanced silicon photo-detector (Newport). IPCE values were calculated using the following equation:

$$IPCE(\lambda) = \frac{1240\, j_p(\lambda)}{\lambda\, E_\lambda(\lambda)}$$

where $j_p(\lambda)$ is the measured photocurrent density (mA/cm^2) and $E_\lambda(\lambda)$ is the incident light power density (mW/cm^2) for each wavelength, λ (nm).

The measured potentials *vs.* the Ag/AgCl were converted to the reversible hydrogen electrode (RHE) scale *via* the Nernst equation:

$$E_{RHE} = E_{Ag/AgCl} + 0.059\ pH + E^o_{Ag/AgCl}$$

where E_{RHE} is the converted potential vs. RHE, $E_{Ag/AgCl}$ is the experimental potential measured against the Ag/AgCl reference electrode, and $E^o_{Ag/AgCl} = 0.1976$ V at 25 ^oC.

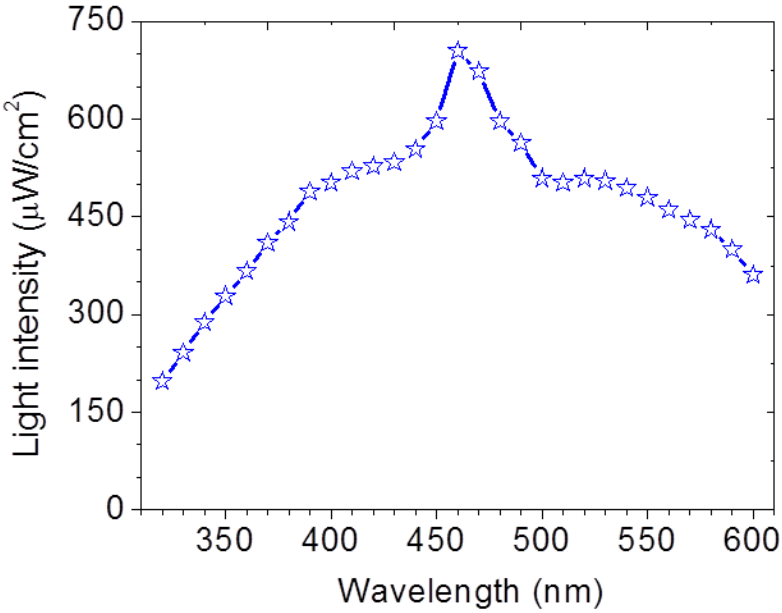

Figure 4.1. A typical incident light power density spectrum (from 320 nm - 600nm) used for the IPCE measurements.

RESULTS AND DISCUSIONS

Synthesis and Characterization of Ta-incorporated TiO_2 (Ta:TiO_2) Nanowire arrays.

The pristine TiO_2 NWs were grown on fluorine-doped tin oxide (FTO) glass substrate using a method reported elsewhere [21] with a slight change in the recipe; $TiCl_4$ was added to the reaction solution to enhance the NW arrays' adherence to the FTO substrate. The feature sizes of TiO_2 NW arrays obtained with the addition of $TiCl_4$ are almost the same , ~ 5 nm.[21] However, the new recipe results in much shorter TiO_2 NWs, ~ 1.4 μm compared to 4.4 μm obtained without $TiCl_4$. The Ta:TiO_2 NW arrays with various Ta incorporation levels are designated as Ta:TiO_2-xxx where xxx (xxx= 010-250) is the number of 10 μL volumes of 10% w/v Ta (V) isopropoxide in isopropanol/n-hexane solution added to the solvothermal reaction solution. Figure 4.2 shows the top-view Scanning Electron Microscopy (SEM) images of as-synthesized Ta:TiO_2 nanowire

arrays synthesized with various volumes of Ta precursor. The nanowire arrays consist of vertically aligned and densely packed nanowires with the feature sizes ranging from 5-20 nm. As mentioned above, the pristine TiO_2 nanowires have similar tetragonal shapes and sizes as reported previously (synthesized using the slightly different recipe) (Figure 4.2a).[21] Adding the Ta precursor solution significantly changes the morphology; the nanowires become bigger when we increase the amount of Ta precursor from 0.1 to 0.75 mL. However adding even more Ta precursor (1 mL – 2.5 mL) decreases the nanowire sizes and causes a change in the tetragonal cross-sectional shape. The length of the NWs (film thicknesses) are however unaffected with the addition of the Ta precursor. All of the samples have a thickness of ~ 1.4 μm.

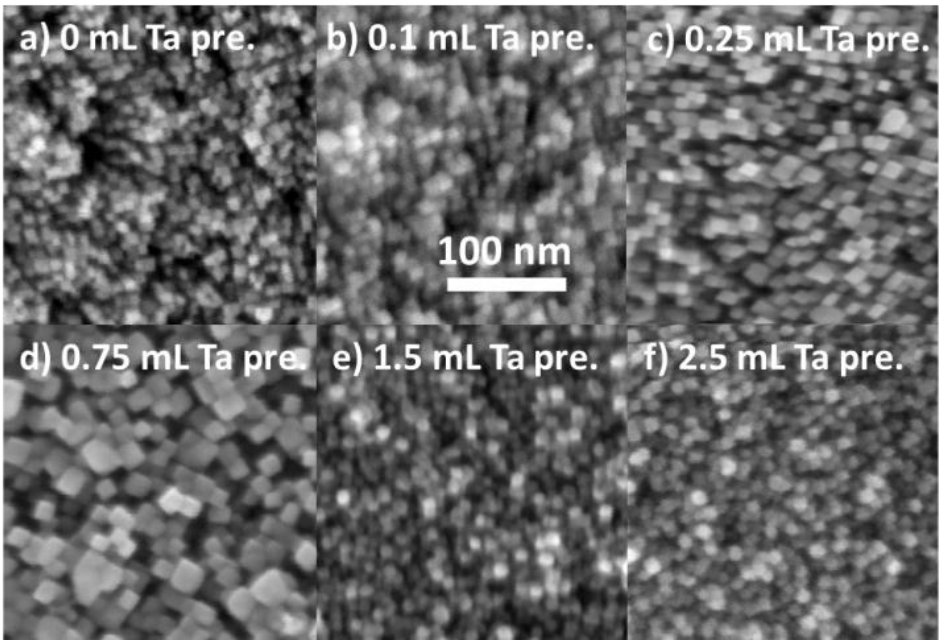

Figure 4.2. Top-view Scanning Electron Microscopy (SEM) images of Ta:TiO_2 nanowires synthesized with various amount of Ta precursor: (a) 0 mL (pristine TiO_2), (b) 0.1 mL, (c) 0.25 mL, (d) 0.75 mL, (e) 1.5 mL, and (f) 2.5 mL. The scale bar is applied for all the micrographs.

In order to investigate the effects of Ta (V) isopropoxide and isopropanol on the morphology of the nanowires, we performed control experiments via the addition of 0.125 mL, 0.375 mL, and 1.25 mL of pure isopropanol (equivalent to the amount of isopropanol in 0.25 mL, 0.75 mL, and 2.5 mL of the Ta precursor) to the solvothermal reaction solution to grow pristine TiO_2 nanowires. Interestingly, addition of isopropanol leads to the same vertically aligned nanowire morphology but with a bigger cross-sectional dimension ~ 10-15 nm (Figure 4.3). However, the feature size of the nanowires does not change with increasing amounts of isopropanol above 0.125 mL. Therefore, we believe that the interaction of Ta (V) isopropoxide and isopropanol contribute to the morphology changes as observed in Figure 4.2.

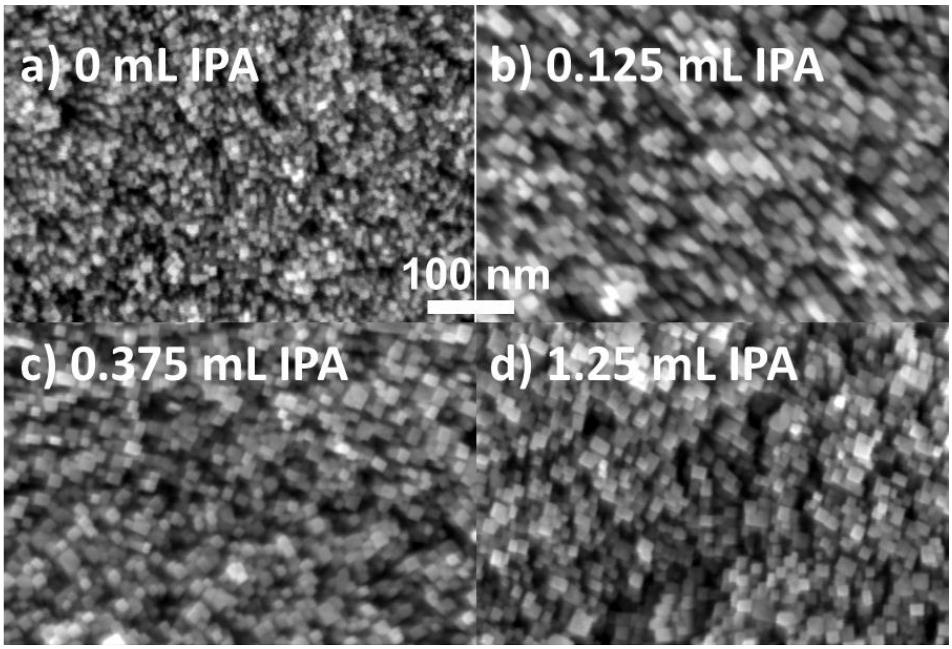

Figure 4.3. SEM images of TiO_2 nanowire arrays synthesized with addition of isopropanol (IPA): (a) 0 mL, (b) 0.125 mL, (c) 0.375 mL, and (d) 1.25 mL. The scale bar is applicable for all micrographs.

We employed X-ray Photoemission Spectroscopy (XPS) to investigate the chemical composition of the Ta:TiO_2 nanowires (Figure 4.4). As previously reported, TiO_2 NW arrays were solvothermally grown *via* nonpolar solvent/hydrophilic solid substrate interfacial reaction mechanism in which Ti (IV) isopropoxide was hydrolyzed forming TiO_2.[21,37] Hydrolyzation of Ta(V) isopropoxide forms Ta_2O_5, therefore we expect that Ta is incorporated into the TiO_2 lattice as Ta^{5+}. Indeed, the Ta 4f features at 26.2 eV and 28.3 eV (Figure 4.4a) of the Ta-modified TiO_2 samples have been assigned to Ta^{5+}, thus confirming our hypothesis.[30] Figure 4.4b shows the Ta atomic percentage determined by XPS in the Ta:TiO_2 nanowires synthesized with various amounts of Ta precursor. The Ta concentration increases with increasing Ta precursor as expected. The Ta concentration in the nanowires increases almost linearly from 0.11-0.29 atomic % with increasing Ta precursor from 0.25 mL to 0.75 mL, but increases much faster from 0.61-3.48 atomic % when increasing the Ta precursor amount from 1 mL to 2.5 mL. In order to investigate the variation of Ta content in the nanowires synthesized with the same recipe, the Ta content was measured for different samples synthesized under the same conditions. The Ta content measured for 5 samples synthesized with addition of 0.75 mL of Ta precursors (samples Ta:TiO_2-075) is 0.26 ± 0.048 at.%.

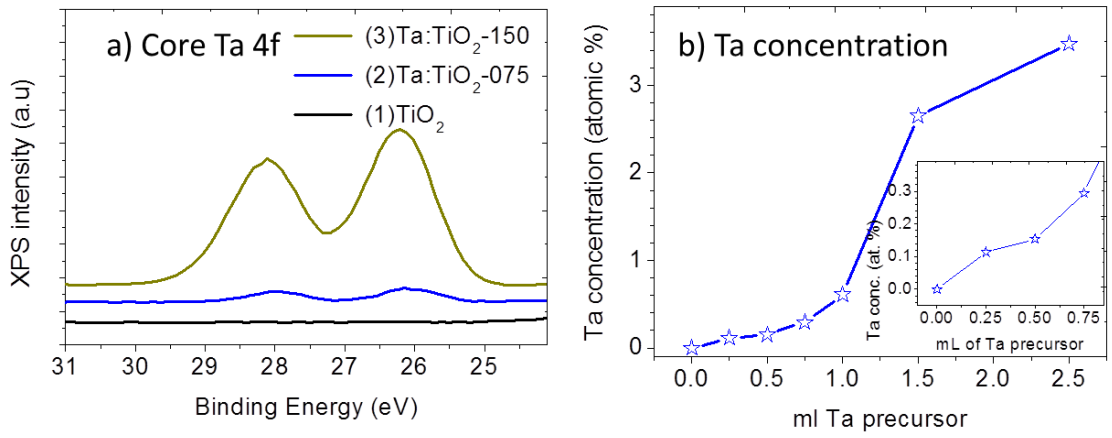

Figure 4.4. a) Core Ta 4f XPS spectra of Ta:TiO_2 nanowires synthesized with various amount of Ta precursor (1) TiO_2, (2) Ta:TiO_2-075 (0.75 mL Ta precursor), and (3) Ta:TiO_2-150 (1.50 mL Ta precursor) and (b) atomic percentage of Ta in the Ta:TiO_2 nanowires determined by XPS, the inset magnified the low Ta concentration region.

Figure 4.5a shows the grazing incidence angle X-ray diffraction (GIXRD) pattern of Ta:TiO_2 nanowires with various levels of Ta incorporation. Since the Ta:TiO_2 NWs were grown on an FTO substrate, we performed GIXRD measurements to avoid interference from the SnO_2 layer on the substrate. We did not observe any phase other than rutile (PDF#97-003-1323) in all samples, even in the sample with high Ta concentration (sample Ta:TiO_2-150 – 2.65 at. % of Ta). The XRD features of Ta:TiO_2 NWs are slightly narrower than that of pristine TiO_2 NWs, indicating that grain sizes of Ta:TiO_2 NWs are bigger than that of pristine TiO_2 NWs, which is in agreement with SEM measurements (Figure 4.1).

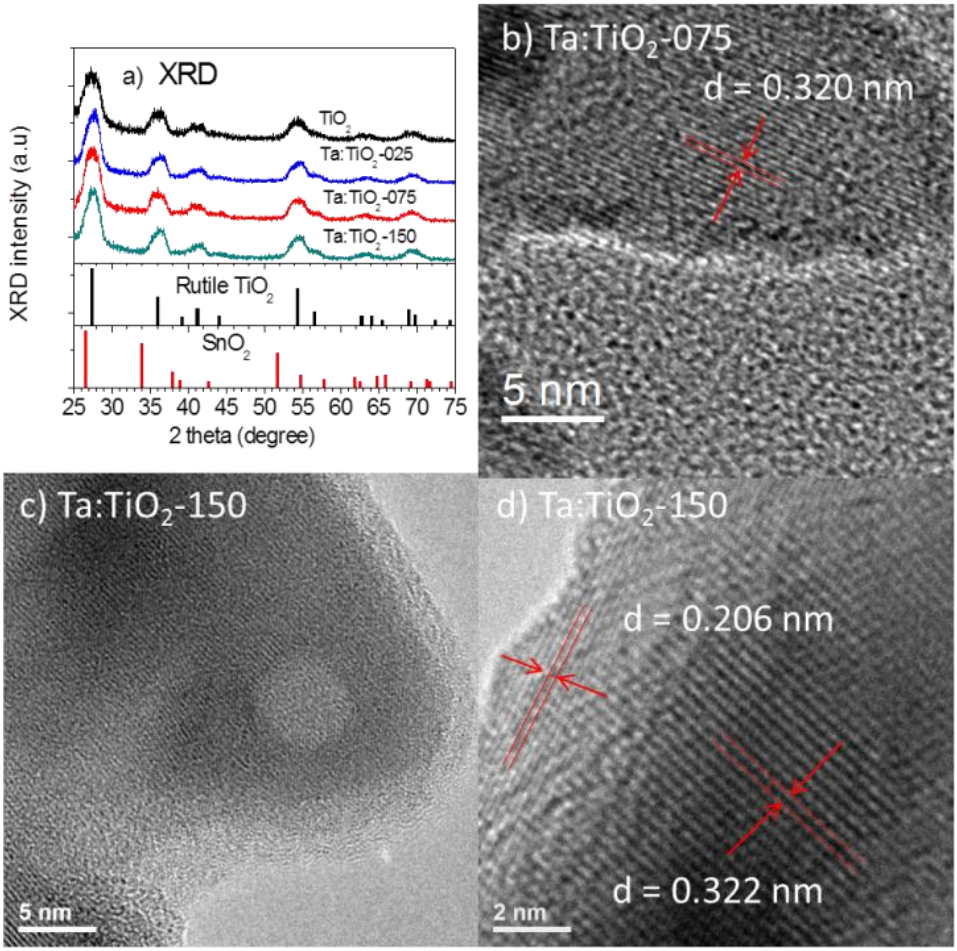

Figure 4.5. (a) Grazing incidence angle X-ray diffraction pattern of Ta:TiO_2 nanowires on F:SnO_2 coated substrates: TiO_2 (black), Ta:TiO_2-025 (blue), Ta:TiO_2-075 (red), and Ta:TiO_2-150 (cyan) and HRTEM images of (b) Ta:TiO_2-075, (c) and (d) Ta:TiO_2-150

High resolution transmission electron microscopy (HRTEM) was employed for further investigation of the structure of the Ta:TiO_2 nanowires. HRTEM of Ta:TiO_2-075 nanowires (figure 4.5b) did not show a core/shell structure, indicating homogeneous incorporation of Ta at this low doping level. No significant change in the lattice was found after Ta incorporation as expected due to the comparable ionic radii (with VI co-ordination) of Ti^{4+} (0.061 nm) and Ta^{5+} (0.064 nm) ions.[38] The interplanar d-spacing of

(110) planes for the Ta:TiO_2-075 determined from HRTEM is 0.320 nm, compared to 0.324 nm for that of the pristine TiO_2 NW. The Ta:TiO_2-150 NWs, however, displayed a core/shell structure as shown in figure 4.5c and 4.5d. The d-spacing for the outer shell is 0.206 nm, thus indexing for the (210) plane. The d-spacing for the core is 0.322 nm, indexing for the (110) plane. Arab *et al.* reported a solvothermal synthesis of branched Ta-incorporated TiO_2 using titanium butoxide as Ti precursor and tantalum butoxide as Ta precursor.[39] The authors reported changes in the surface roughness of the branches and believed that the differences in the rates of hydrolysis and condensation between Ti and Ta alkoxides would change the rate of nucleation of metal oxides, thus affecting the crystallinity and mechanism of growth of the nanowires. Feng *et al.* reported a solvothermal synthesis of homogenous Ta-doped TiO_2 nanowires using $TaCl_5$ as Ta precursor but did not report the Ta concentration.[40]

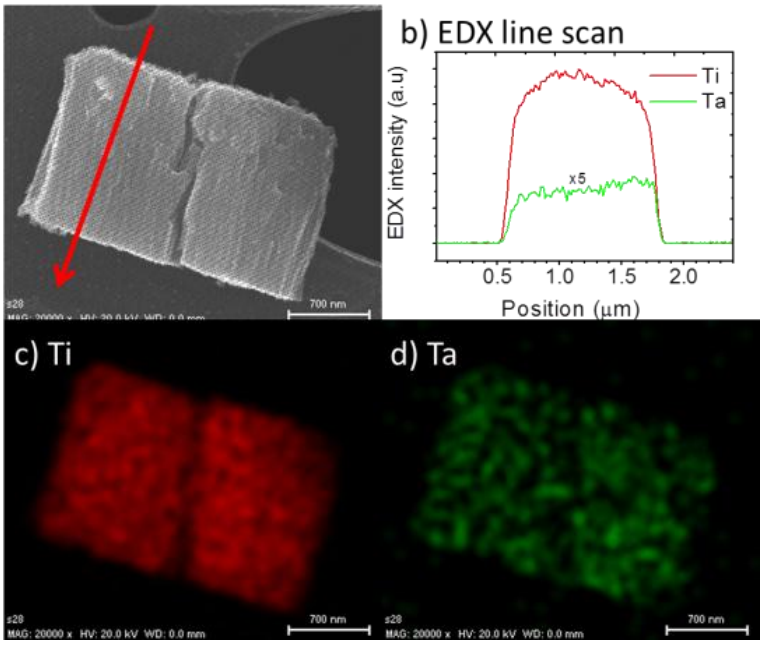

Figure 4.6. (a) SEM image of a chunk of Ta:TiO_2-150 nanowire arrays, (b) EDX line scan profile acquired along the NW arrays shown in Figure 4.4a, (c) and (d) Ti and Ta elemental mapping of the Ta:TiO_2-150 NW chunks shown in Figure 4.4a.

Figure 4.6b shows the energy-dispersive X-ray spectroscopy (EDX) line scan profile acquired along the length of a nanowire array as shown in Figure 4.6a, demonstrating that Ta is incorporated homogenously along the nanowire. Figure 4.6c and 4.6d show Ti and Ta elemental mapping of the nanowire array shown in Figure 4.6a, further confirming homogenous incorporation of Ta into the TiO_2 NW lattice.

Photoelectrochemical Water Oxidation Properties of Ta:TiO_2 Nanowires. The photoelectrochemical characterization of TiO_2 and Ta:TiO_2 NW samples was performed using a three-electrode electrochemical cell with the nanowire arrays as the working electrode, a Ag/AgCl reference electrode, a Pt wire counter electrode, and 1 M KOH electrolyte. A 150 W xenon lamp with an AM 1.5 G filter was used as the light source, providing a light intensity of 100 mW/cm^2 (more details can be found in the experimental section). Before testing, the as-synthesized films were annealed in air at 500 ^oC for 2 hours to remove contaminants and improve the adherence of the NW arrays to the substrate. Figure 4.7a shows the photocurrent density at 1.23 V_{RHE} of Ta:TiO_2 samples with Ta precursor volumes ranging from 0 to 2.5 mL (Ta incorporation levels ranging from 0 to 3.47 at. %). In the low Ta incorporation range from 0-0.61 at. % (*i.e.* Ta precursor ranging from 0-1 mL), the PEC performance increases as Ta concentration increases, reaching a maximum for a Ta concentration of 0.15 at. % (volume of Ta precursor- V_{Ta} = 0.5 mL); the PEC performance, however, decreases with increasing Ta concentration to 0.29 and 0.61 at. % (V_{Ta} = 0.75-1 mL). Figure 4.7b shows linear sweep voltammetry (LSV) measurements of the pristine TiO_2 and Ta:TiO_2-050 (0.15 at. % Ta) samples. The onset potentials of photocurrents of the pristine TiO_2 and Ta:TiO_2-50 NWs are almost the same at around, ~ 0.2 V_{RHE}, indicating that the flat band potential, thus the (quasi) Fermi level and the position of the conduction band (CB) edge does not shift with

the incorporation of Ta. Indeed, both IPCE and UV-vis transmittance spectra (Figure 4.7c and 7d) indicate no change in the band gap of pristine TiO_2 and Ta:TiO_2 NW samples, thus any shift of the CB edge would have to be complemented with a shift of the valence band edge, which is unlikely. The Ta:TiO_2-050 sample shows a significant improvement in the photoactivity with the photocurrent reaches 0.44 mA/cm^2 at 1.23 V vs. reversible hydrogen electrode (V_{RHE}), compared to that of 0.23 mA/cm^2 for the pristine TiO_2 sample. As mentioned previously, no band gap change in any Ta:TiO_2 NW sample was observed so we believe that the enhancement in the PEC performance of Ta:TiO_2 nanowires is likely due to (1) an improvement in charge transfer properties, (2) faster kinetics for surface water oxidation, and (3) an increase in the cross-sectional feature sizes. Incorporation of Ta^{5+} into the TiO_2 lattice can be considered as an n-type 'doping' method to improve the donor density and electron conductivity of TiO_2.[40] Indeed, n-type 'doping' TiO_2 NWs via Sn incorporation [41] or thermal treatment with hydrogen [42] has been demonstrated to significantly improve the PEC performance. Continued increasing of the Ta^{5+} incorporation (0.29-0.61 at. %) will reduce the depletion layer width due to the increase in donor density, thus lowering charge separation efficiency, which in turn reduces the photocurrent.

It is interesting that the photocurrent increases again at high Ta doping (2.65 and 3.47 at. %), probably as the result of an enhancement in charge collection efficiency due to the unique core/shell structure as observed in HRTEM in Figure 4.5c and 4.5d. Hwang *et al.* reported an enhancement in PEC performance in core/shell structured TiO_2 nanowires prepared by atomic layer deposition of a epitaxial rutile TiO_2 layer on hydrothermally grown rutile TiO_2 nanowires.[43] The authors proposed that the ALD coating passivates surface states and increases surface area, thus improving the charge collection efficiency.

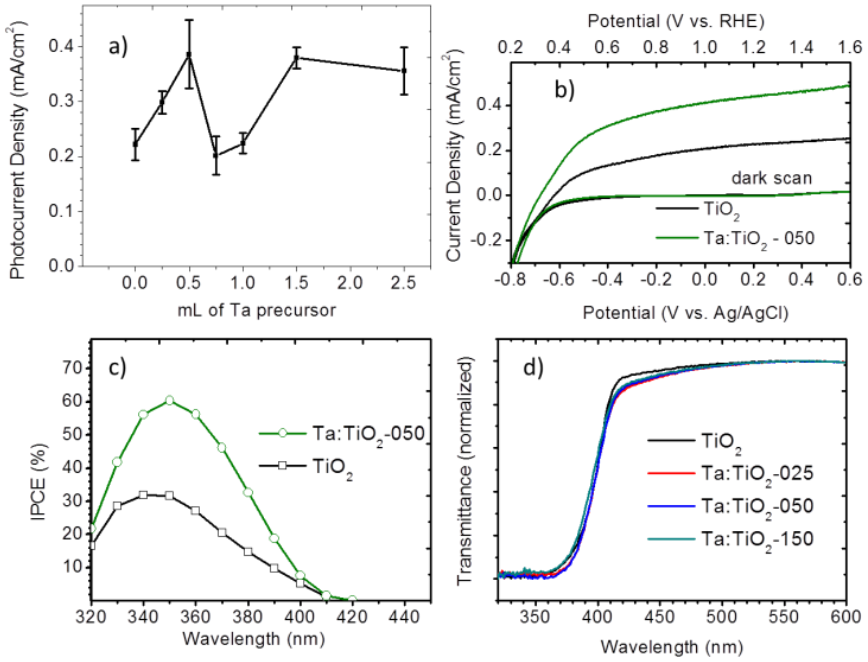

Figure 4.7. (a) Photocurrent density at 1.23 V_{RHE} of pristine TiO_2 NW sample and Ta:TiO_2 NW samples with various amount of Ta precursor, (b) linear sweep voltammetry (LSV) (scan rate of 25 mV/s) of TiO_2 (black) and Ta:TiO_2-050 (green) NW samples, (c) IPCE spectra measured at 1.23 V_{RHE} and (d) UV-vis transmittance spectra of TiO_2 NW sample and Ta:TiO_2 NW samples. All the PEC measurements were conducted using a three-electrode electrochemical cell with a Ag/AgCl reference electrode, a Pt wire counter electrode, and 1 M KOH electrolyte. A solar simulator (Oriel 96000) with an AM 1.5 G filter with a light intensity of 100 mW/cm^2 was employed as the light source.

Synthesis and Characterization of N and Ta co-incorporated TiO_2 (N, Ta:TiO_2) Nanowire arrays. N, Ta:TiO_2-xxx NWs were synthesized by annealing the corresponding Ta:TiO_2-xxx NWs at 500 ^oC in NH_3 flow (30 mL/min) for 2 hours. For comparison, N-modified TiO_2 (N:TiO_2) samples were prepared by annealing the pristine TiO_2 NW sample in NH_3 flow under the same conditions.

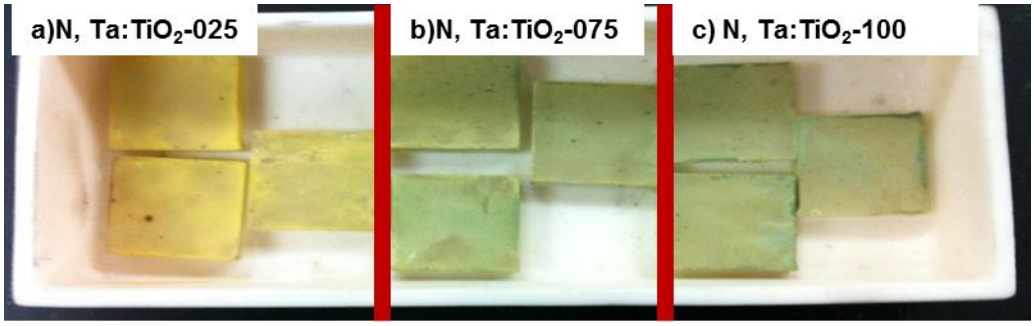

Figure 4.8. Digital images of N, Ta-coincorporated TiO_2 nanowire samples synthesized with various amount of Ta precursor (a) 0.25 mL, (b) 0.75 mL, and (c) 1.00 mL.

After nitridation, the white color of TiO_2 and Ta:TiO_2 samples turns to yellow for samples with Ta incorporation levels less than 0.15 at.% (volume of Ta precursor less than 0.5 mL) and green for samples with Ta incorporation levels greater than 0.15 at.% (volume of Ta precursor greater than 0.5 mL) (Figure 4.8). XRD indicated no crystal structure changes for any films; only the rutile phase was observed for all samples (Figure 4.9).

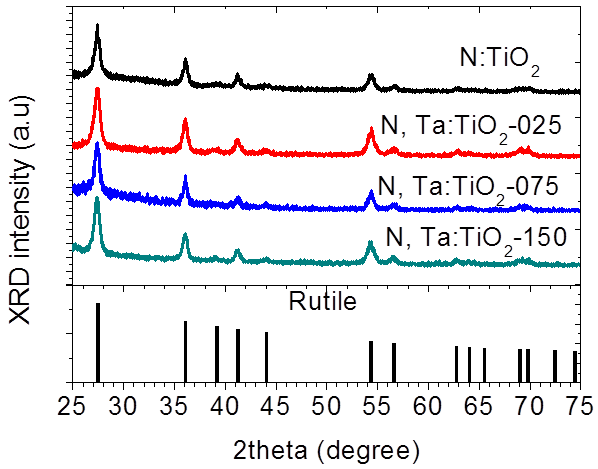

Figure 4.9. XRD of N:TiO_2 and N, Ta:TiO_2 nanowire samples

The cross section of the N:TiO_2 NWs (mono-incorporation of N) becomes larger and does not retain the sharp tetragonal shape (Figure 4.10a) of the as-synthesized pristine TiO_2 NWs. On the other hand, Figure4. 6c indicates no changes in the cross section of the N, Ta:TiO_2-075 sample (as well as other N, Ta-coincorporated samples – Figure 4.11) after nitridation.

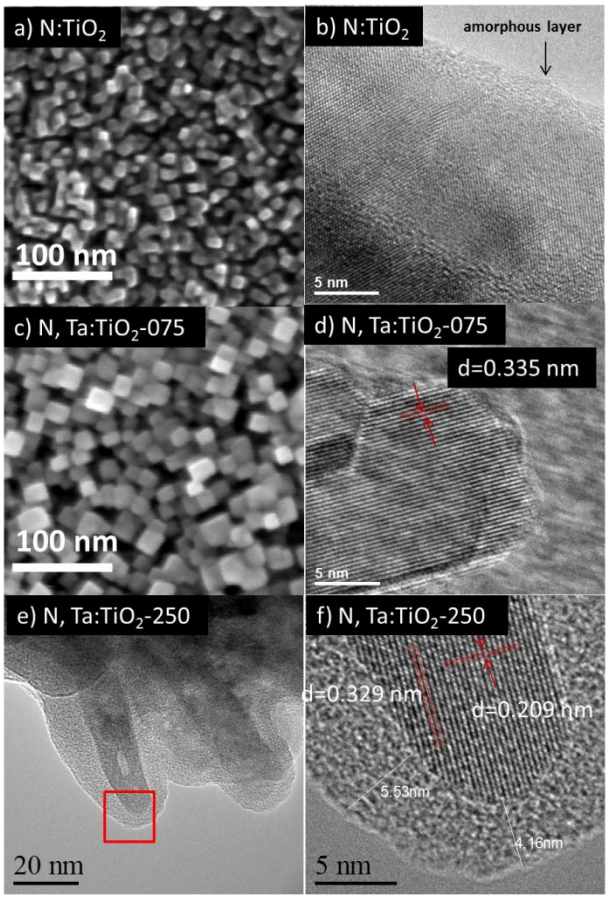

Figure 4.10. SEM images of (a) N:TiO_2 NW and (c) N,Ta:TiO_2-075 NW and HRTEM images of (b) N:TiO_2 NW, and (d) N,Ta:TiO_2-075 NW, (e) TEM images of N, Ta:TiO_2-250 (NW) and (f) HRTEM images of N, Ta:TiO_2-250 NW (the area on the red box on figure 10e)

HRTEM images of the N:TiO_2 NW (Figure 4.10a) indicates that an amorphous layer with a thickness of 1-2 nm (which probably causes the rounded shape of the nanowire) and a multi-domain structure were formed after nitriding the pristine TiO_2 NWs. On the other hand, we did not observe the formation of an amorphous layer or multi-domain structure on the HRTEM image of N, Ta:TiO_2-075 NWs (Figure 4.10d). The inter planar d-spacing of N, Ta:TiO_2-075 was measured as 0.335 nm, compared to 0.324 nm for pristine TiO_2 indicating a lattice expansion due to incorporation of Ta and N. This demonstrates that incorporating Ta^{5+} ions helps N inclusion into the TiO_2 lattice without damaging the structure. In fact, Yin *et al.* predicted that Ta and N would exhibit a high binding energy (1.92 eV), thus coincorporation of Ta and N overcomes the solubility of N in TiO_2 lattices as well as improving the material quality over mono-incorporation of N.[12] It is interesting to note that the amorphous layer with a thickness > 4.1 nm appears on N, Ta:TiO_2-250 nanowire sample (Figure 4.10e and 4.10f) which might explains for the low photoelectrochemical performance of this sample shown in a later section. We, however, have not figured out the reason for the formation of this amorphous layer.

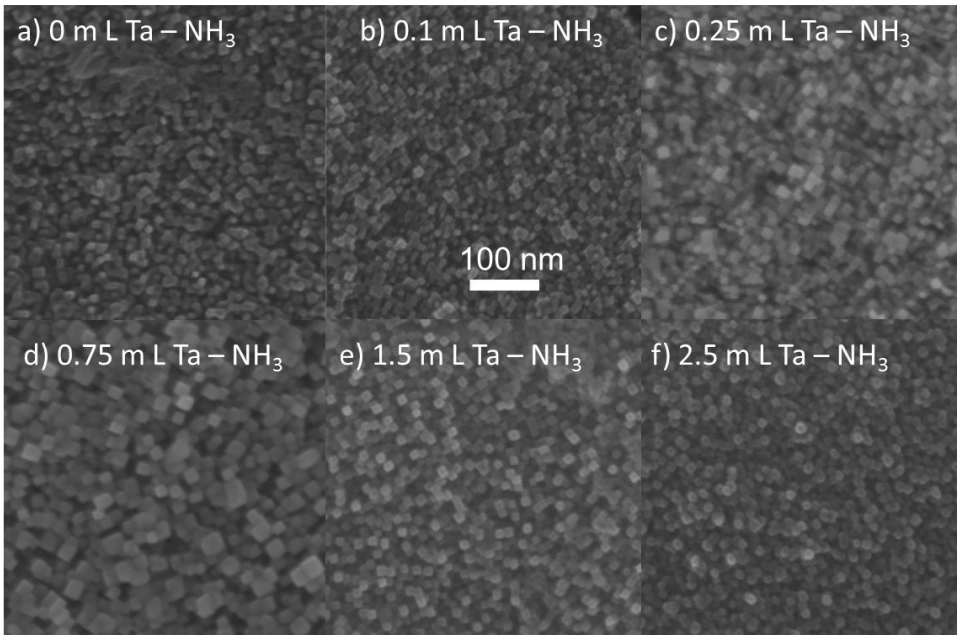

Figure 4.11. Top-view SEM images of N, Ta:TiO_2 nanowires synthesized with various amount of Ta precursor: (a) 0 mL (pure TiO_2), (b) 0.1 mL, (c) 0.25 mL, (d) 0.75 mL, (e) 1.5 mL, and (f) 2.5 mL. The scale bar is applicable for all the micrographs.

XPS was also employed to determine the surface N content in the N:TiO_2 and N, Ta:TiO_2 samples (Figure 4.12). We only observed an N feature at 400 eV (which is commonly assigned for molecular N_2 adsorbed on the surface) for all samples including the pristine TiO_2 nanowires.[10,21] We could not detect any N feature at ~ 396 eV which is assigned for substitutional N species,[10] probably due to the resolution limit of the XPS instrument in our experiment, thus we could not estimate the concentration of N incorporated into the TiO_2 lattice (note that the nitridation conditions used in the present work are less severe than that used in our previous reports [21,24]).

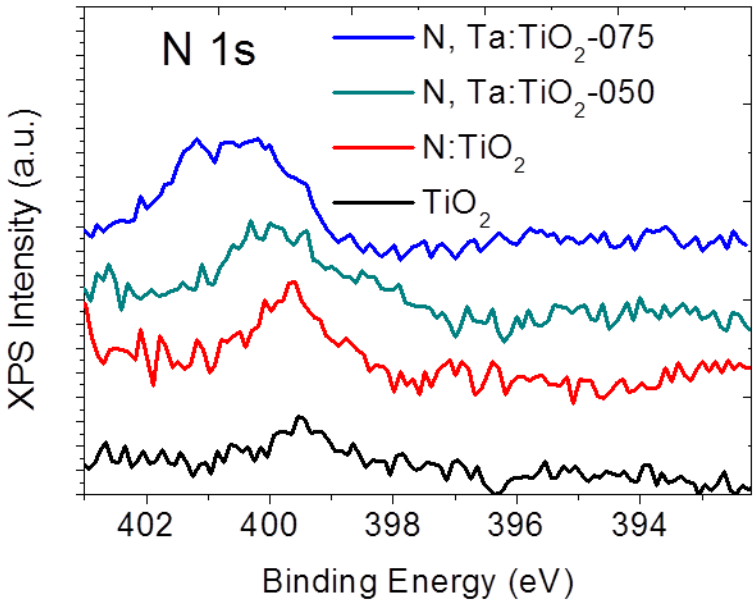

Figure 4.12. XPS spectra of core N 1s for TiO_2 (black), N:TiO_2 (red), N, Ta:TiO_2-050 (cyan), and N, Ta:TiO_2-075 (blue). The feature at ~ 400 eV is assigned for N species absorbed on the surface.

We, however, can observe the interaction of Ta and N in the core Ti 2p and core O 1s XPS spectra of TiO_2, N:TiO_2, and N, Ta:TiO_2 samples (figure 4.13). The Ti 2p feature at 458.85 eV of TiO_2 NWs shifted to 458.55 eV upon nitridation indicating an increase in the electron density around Ti^{4+} ions due to the substitution of O^{2-} ions by the more the negative N^{3-} ions. Cong et al. reported that the partial electron transformation from N to Ti causes an increase in the electron density around Ti, thus lowering the binding energy of Ti 2p.[44] The similar phenomena were also reported by several other authors including Chen et al., Li et al., and Sathish et al.[45-47] Increasing Ta^{5+} incorporation level shifts the Ti 2p feature back to higher binding energies of 458.75 eV for N, Ta:TiO_2-050 and 458.85 eV for N, Ta:TiO_2-075 samples, respectively. A similar

trend is observed for XPS core O 1s, confirming that Ta^{5+} acts as a charge compensation dopant for N^{3-}.

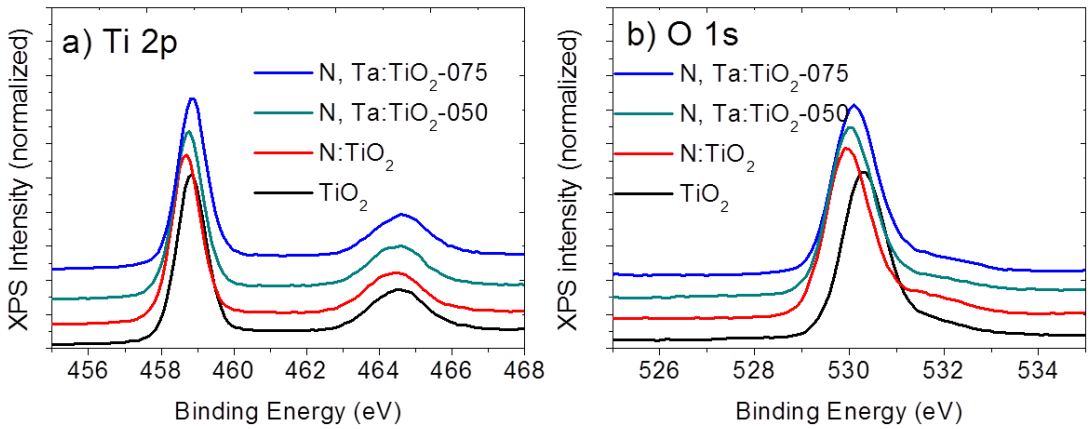

Figure 4.13. XPS spectra of (a) core Ti 2p and (b) core O 1s for TiO_2 (black), N:TiO_2 (red), N, Ta:TiO_2-050 (cyan), and N, Ta:TiO_2-075 (blue).

Figure 4.14a shows the AM 1.5 G photocurrent of N, Ta:TiO_2 samples with various Ta incorporation obtained by chronoamperometry measurements (CAM) at 1.23 V_{RHE}. The photocurrent increases with greater amounts of Ta precursor, reaching a maximum photocurrent of 0.55 mA/cm^2 with addition of 0.75 mL Ta precursor (corresponding to 0.3 at. % Ta), then decreases when more Ta precursor is added. Figure 4.8b shows the results of LSV measurements of N-TiO_2 and N, Ta:TiO_2-075 samples. The onset potentials of the photocurrents are shifted to 0.4 V_{RHE} for both samples, likely due to either a large band bending requirement for photogenerated electron and hole separation or slower surface kinetics as a result of incorporating N into the TiO_2 and Ta:TiO_2 lattice.[21] The N, Ta:TiO_2-075 sample shows significant enhancement in PEC performance compared with N:TiO_2 samples both the in UV and visible region. The photocurrent of the N, Ta:TiO_2-075 sample reaches 0.52 mA/cm^2 and 0.18 mA/cm^2 at

1.23 V_{RHE} under AM 1.5 G and visible light (>420 nm) illumination, compared with 0.26 mA/cm^2 and 0.13 mA/cm^2 for that of the N-TiO_2 sample. Figure 4.14c shows the IPCE spectra measured at 1.23 V_{RHE} for N, Ta:TiO_2-075 and N:TiO_2 samples. The photocurrents obtained by integrating the calculated IPCE multiplied by the whole and the visible light range (>420nm) of the AM 1.5 G solar energy flux [48] is 0.55 mA/cm^2 and 0.16 mA/cm^2 for N, Ta-TiO_2-075 sample, and 0.28 mA/cm^2 and 0.09 mA/cm^2 for the N-TiO_2 sample, respectively, which are in good agreement with the LSV and CAM measurements mentioned above. It is interesting to note that both the IPCE spectra and UV-vis transmittance spectra (figure 4.14d) demonstrate that the active spectra for N, Ta:TiO_2 extends to ~ 520 nm (corresponding to a photon energy of 2.38 eV), compared with ~ 540 nm (2.30 eV) for that of N:TiO_2. Yin *et al*. reported that since the atomic orbital energy of Ta 5d is higher than that of Ti 3d, the conduction band of the N, Ta co-incorporated anatase TiO_2 upshifts 0.05 eV compared to that of pristine anatase TiO_2.[12]

The enhancement in the PEC performance of the co-incorporated film compared to the mono-incorporated N:TiO_2 sample might not be due to better visible light absorption as demonstrated above but likely results from fewer recombination centers due to charge compensated co-incorporation.[12,25,29] In addition, co-incorporation of Ta and N into TiO_2 NWs suppresses the formation of the amorphous layer observed on the N:TiO_2 NWs, thus likely better promoting hole extraction to the electrolyte. We noted that nitridation of the TiO_2 nanowires that are highly incorporated with Ta (sample poor PEC N, Ta:TiO_2-250) lead to formation of a thick amorphous layer (Figure 4.10e-f) thus lowering the PEC performance (Figure 4.14a).

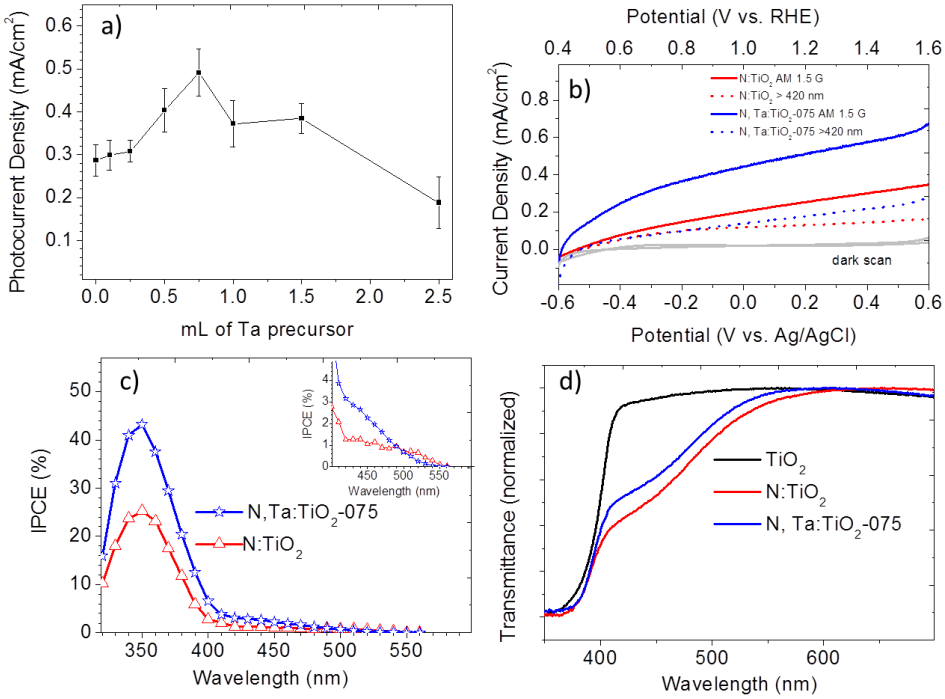

Figure 4.14. (a) Photocurrent density at 1.23 V_{RHE} of N:TiO_2 NW sample and N,Ta:TiO_2 NW samples with various amount of Ta precursor, (b) LSV (scan rate of 25 mV/s) of N:TiO_2 (red) and N,Ta:TiO_2-075 (blue) NW samples under AM 1.5 G (solid line) and visible light (> 420 nm) (dotted line), (c) IPCE spectra measured at 1.23 V_{RHE} and (d) UV-vis transmittance spectra of N:TiO_2 NW sample and N,Ta:TiO_2-075 NW samples. All the PEC measurements were conducted using a three-electrode electrochemical cell with a Ag/AgCl reference electrode, a Pt wire counter electrode, and 1 M KOH electrolyte. A solar simulator (Oriel 96000) with an AM 1.5 G filter with a light intensity of 100 mW/cm^2 was employed as the light source. A UV filter blocking all wavelengths <420 nm was used for visible light measurements.

The electrochemical impedance measurements on the pristine TiO_2, N:TiO_2, Ta:TiO_2-075 and N, Ta:TiO_2-075 nanowire samples (Figure 4.15) show that the slope of the Mott-Schottky plot for N, Ta:TiO_2 NW samples is substantially lower than that for other samples. However, due to the significant change in the morphology of the samples,

it is difficult to comment on the change in the donor density due to the monoincorporation of N, Ta and the coincorporation of Ta and N.

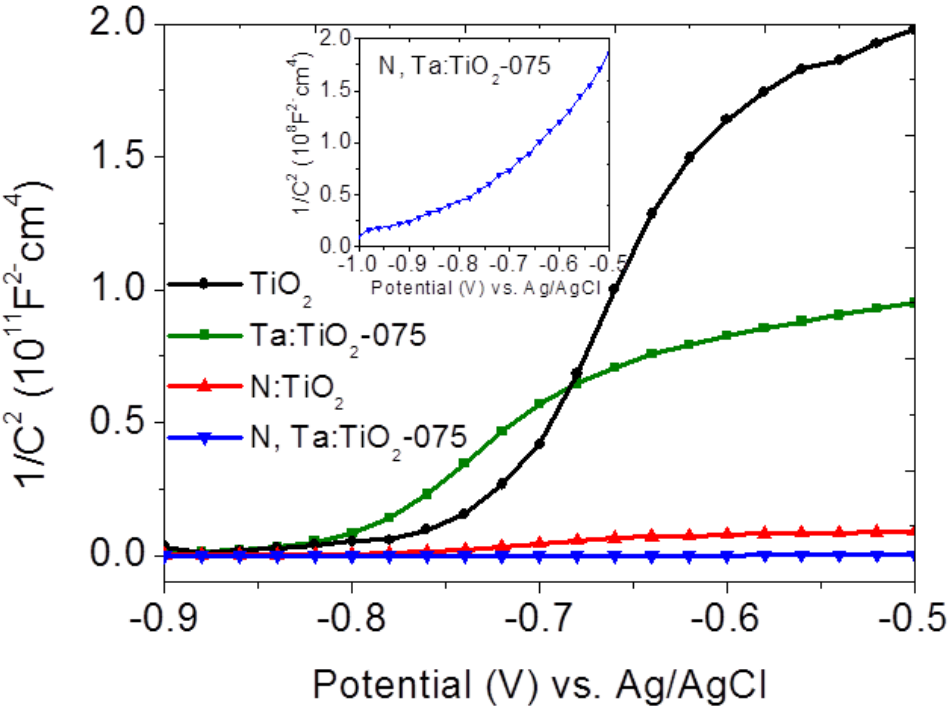

Figure 4.15. Mott-Schottky plots obtained at a frequency of 1 kHz in the dark in 1 M KOH electrolyte for the pristine TiO_2, Ta:TiO_2-075, N:TiO_2, and N, Ta:TiO_2-075 nanowires. The inset enlarges the Mott-Schottky plot for the N, Ta:TiO_2-075 nanowire samples.

CONCLUSIONS

In conclusion, we report the solvothermal synthesis of Ta-incorporated TiO_2 nanowire arrays. The Ta incorporation level can be tuned from 0.11 to 3.5 atomic % by adjusting the volume of the Ta precursor. For low Ta concentrations (<0.30 at %), Ta was incorporated homogenously into the TiO_2 nanowire. On the other hand, a core/shell structure was observed for high Ta incorporation levels (2.65 at. %). We also report the synthesis of N, Ta-coincorporated TiO_2 nanowires arrays by nitridation of the Ta-

incorporated TiO_2 NW arrays in NH_3 flow at the relatively low temperature of 500 ^oC. The IPCE and UV-vis transmittance spectra reveal that the active spectrum of N, Ta:TiO_2 samples extends to ~520 nm, compared with ~ 550 nm for the N-TiO_2 and ~ 420 nm for pristine TiO_2 and Ta:TiO_2 samples. The N,Ta:TiO_2 NW samples show significant enhancement in PEC performance both under AM 1.5 G and visible light (>420 nm) illumination. We speculate that coincorporation of Ta and N reduces charge recombination centers *via* charge compensation effects. In addition, coincorporation of Ta and N suppresses the formation of the amorphous layer during the nitridation process, thus improving hole extraction to the electrolyte and PEC performance.

REFERENCES

(1) Gai, Y.; Li, J.; Li, S.-S.; Xia, J.-B.; Wei, S.-H. Phys. Rev. Lett. 2009, 102, 036402.

(2) Chen, X.; Mao, S. S. Chem. Rev. 2007, 107, 2891.

(3) Fujishima, A.; Honda, K. Nature 1972, 238, 37.

(4) Fujishima, A.; Zhang, X.; Tryk, D. A. Surf. Sci. Rep. 2008, 63, 515.

(5) Chen, X.; Liu, L.; Yu, P. Y.; Mao, S. S. Science 2011, 331, 746.

(6) Linsebigler, A. L.; Lu, G.; Yates, J. T. Chem. Rev. 1995, 95, 735.

(7) Bolton, J. R. Solar Energy 1996, 57, 37.

(8) Bolton, J. R.; Strickler, S. J.; Connolly, J. S. Nature 1985, 316, 495.

(9) Murphy, A. B.; Barnes, P. R. F.; Randeniya, L. K.; Plumb, I. C.; Grey, I. E.; Horne, M. D.; Glasscock, J. A. Int. J. Hydrogen Energy 2006, 31, 1999.

(10) Asahi, R.; Morikawa, T.; Ohwaki, T.; Aoki, K.; Taga, Y. Science 2001, 293, 269.

(11) Khan, S. U. M.; Al-Shahry, M.; Ingler, W. B. Science 2002, 297, 2243.

(12) Yin, W.-J.; Tang, H.; Wei, S.-H.; Al-Jassim, M. M.; Turner, J.; Yan, Y. Phys. Rev. B 2010, 82, 045106.

(13) Choi, J.; Park, H.; Hoffmann, M. R. J. Mater. Res. 2010, 25, 149.

(14) Umebayashi, T.; Yamaki, T.; Itoh, H.; Asai, K. J. Phys. Chem. Solids 2002, 63, 1909.

(15) Ohno, T.; Tanigawa, F.; Fujihara, K.; Izumi, S.; Matsumura, M. J. Photochem. Photobiol., A 1998, 118, 41.

(16) Chen, X. B.; Lou, Y. B.; Dayal, S.; Qiu, X. F.; Krolicki, R.; Burda, C.; Zhao, C. F.; Becker, J. J. Nanosci. Nanotechnol. 2005, 5, 1408.

(17) Choi, W. Y.; Termin, A.; Hoffmann, M. R. J. Phys. Chem. 1994, 98, 13669.

(18) Janisch, R.; Gopal, P.; Spaldin, N. A. J. Phys: Condes. Matter 2005, 17, R657.

(19) Litter, M. I.; Navio, J. A. J. Photochem. Photobiol., A 1996, 98, 171.

(20) Dvoranova, D.; Brezova, V.; Mazur, M.; Malati, M. A. Appl. Catal., B 2002, 37, 91.

(21) Hoang, S.; Guo, S.; Hahn, N. T.; Bard, A. J.; Mullins, C. B. Nano Lett. 2012, 12, 26.

(22) Park, J. H.; Kim, S.; Bard, A. J. Nano Lett. 2005, 6, 24.

(23) Umebayashi, T.; Yamaki, T.; Itoh, H.; Asai, K. Appl. Phys. Lett. 2002, 81, 454.

(24) Hoang, S.; Berglund, S. P.; Hahn, N. T.; Bard, A. J.; Mullins, C. B. J. Am. Chem. Soc. 2012, 134, 3659.

(25) Long, R.; English, N. J. Chem. Phys. Lett. 2009, 478, 175.

(26) Zhu, W.; Qiu, X.; Iancu, V.; Chen, X.-Q.; Pan, H.; Wang, W.; Dimitrijevic, N. M.; Rajh, T.; Meyer, H. M.; Paranthaman, M. P.; Stocks, G. M.; Weitering, H. H.; Gu, B.; Eres, G.; Zhang, Z. Phys. Rev. Lett. 2009, 103, 226401.

(27) Breault, T. M.; Bartlett, B. M. J. Phys. Chem. C, 116, 5986.

(28) Gai, Y. Q.; Li, J. B.; Li, S. S.; Xia, J. B.; Yan, Y. F.; Wei, S. H. Phys. Rev. B 2009, 80.

(29) Ma, X. G.; Wu, Y.; Lu, Y. H.; Xu, J.; Wang, Y. J.; Zhu, Y. F. J. Phys. Chem. C 2011, 115, 16963.

(30) Obata, K.; Irie, H.; Hashimoto, K. Chem. Phys. 2007, 339, 124.

(31) Huang, J.; Wen, S.; Liu, J.; He, G. Journal of Natural Gas Chemistry 2012, 21, 302.

(32) Wang, W.; Lu, C.; Ni, Y.; Su, M.; Huang, W.; Xu, Z. Appl. Surf. Sci. 2012, 258, 8696.

(33) van de Krol, R.; Liang, Y. Q.; Schoonman, J. J. Mater. Chem. 2008, 18, 2311.

(34) Hahn, N. T.; Ye, H.; Flaherty, D. W.; Bard, A. J.; Mullins, C. B. ACS Nano 2010, 4, 1977.

(35) Mor, G. K.; Prakasam, H. E.; Varghese, O. K.; Shankar, K.; Grimes, C. A. Nano Lett. 2007, 7, 2356.

(36) Cho, I. S.; Chen, Z.; Forman, A. J.; Kim, D. R.; Rao, P. M.; Jaramillo, T. F.; Zheng, X. Nano Lett. 2011, 11, 4978.

(37) Feng, X.; Shankar, K.; Varghese, O. K.; Paulose, M.; Latempa, T. J.; Grimes, C. A. Nano Lett. 2008, 8, 3781.

(38) Shannon, R. D. Acta Crystallogr. Sect. A 1976, 32, 751.

(39) Arab, S.; Li, D. S.; Kinsinger, N.; Zaera, F.; Kisailus, D. J. Mater. Res. 2011, 26, 2653.

(40) Feng, X.; Shankar, K.; Paulose, M.; Grimes, C. A. Angew. Chem. Int. Ed. 2009, 48, 8095.

(41) Xu, M.; Da, P.; Wu, H.; Zhao, D.; Zheng, G. Nano Lett. 2012, 12, 1503.

(42) Wang, G.; Wang, H.; Ling, Y.; Tang, Y.; Yang, X.; Fitzmorris, R. C.; Wang, C.; Zhang, J. Z.; Li, Y. Nano Lett. 2011, 11, 3026.

(43) Hwang, Y. J.; Hahn, C.; Liu, B.; Yang, P. ACS Nano 2012, 6, 5060.

(44) Cong, Y.; Zhang, J.; Chen, F.; Anpo, M. J. Phys. Chem. C 2007, 111, 6976.

(45) Chen, X.; Burda, C. J. Phys. Chem. B 2004, 108, 15446.

(46) Li, H.; Li, J.; Huo, Y. J. Phys. Chem. B 2006, 110, 1559.

(47) Sathish, M.; Viswanathan, B.; Viswanath, R. P.; Gopinath, C. S. Chem. Mater. 2005, 17, 6349.

(48) http://rredc.nrel.gov/solar/spectra/am1.5/.

Chapter 5: Low Temperature Hydrothermal Synthesis of Vertically Aligned TiO_2 Nanoplatelet Arrays for Solar Energy Conversion Applications

INTRODUCTION

Titanium dioxide (TiO_2) is an abundant, low-cost, non-toxic, and photo-chemically stable metal oxide that has been widely used as a white pigment and sunscreen.[1-4] TiO_2 is also a promising semiconductor material for various applications in photoelectrochemical (PEC) water splitting cells, organic pollutant photodegradation, lithium-ion batteries, and dye sensitized solar cells (DSSCs).[1, 5-7] TiO_2 has a large band gap of 3.0 eV for rutile and 3.2 eV for anatase, therefore setting its theoretical maximum solar energy (AM 1.5 G conditions) conversion efficiency at 2.2 %.[8] Since Fujishima and Honda discovered the photoelectrolysis of water using an n-type rutile TiO_2 phoanode in 1972,[1] numerous efforts have focused on improving the solar energy conversion efficiency of TiO_2 materials via (1) reducing the band gap of TiO_2 or sensitizing TiO_2 with dye molecules to absorb visible light and (2) fabricating nanostructures of TiO_2 to improve charge transport properties and to increase surface area for dye adsorption.[5, 6, 9-15] Incorporating TiO_2 with nonmetal ions such as C,[16] N,[5, 12] etc., and coincorporating TiO_2 with metal and nonmetal ions[17-19] have shown some successes in extending the optical absorption edge to the visible light region. Sensitization of TiO_2 photoelectrodes with dye molecules for application in DSSCs has proven very efficient to convert visible light into electricity and has been the subject of extensive research since the discovery of O'Regan and Gräzel in 2001.[6]

Besides enhancing optical absorption, it is equally important to improve the charge transport properties of TiO_2.[11, 20-22] In a PEC water splitting cell, holes

photogenerated in TiO_2 must diffuse to the electrode/electrolyte interface to participate in water oxidation, while photogenerated electrons must diffuse to the electrical contact then transport to the cathode to participate in water reduction. The hole diffusion length of TiO_2 is ~ 10 nm,[23] significantly smaller than the optical path length required for light absorption (on order of 1 μm), therefore most photogenerated holes recombine before reaching electrolyte in a dense film of a sufficient thickness for light absorption. Recent work has focused on one dimensional nanostructures of TiO_2 such as nanotubes, nanorods, nanowires etc., since these structures provide equivalent optical penetration depth to planar dense films but with less distance required for holes to diffuse to the interface (holes only need to diffuse across the radius of nanowires or the wall thickness of the nanotubes).[11-14, 20] In addition to rapid charge transport properties, these nanostructures offer high surface area for dye adsorption which is essential for improving solar conversion efficiency in DSSCs.[24, 25]

In the present study, we report a simple, scalable, low temperature hydrothermal synthesis of nanoplatelet arrays of rutile TiO_2 with lengths of ~ 130 nm, widths of ~ 5 nm, and heights (film thicknesses) of ~ 1μm on fluorine doped tin oxide (FTO) coated glass substrates for photoanodes in PEC water oxidation and DSSC applications. We also demonstrate that this method can be applied for growing nanoplatelet arrays on various substrates including but not limited to Ti foil, glass, polyethylene terephthalate (PET) plastic, Si wafers, etc. The scalability, ease of synthesis, low cost (using low cost precursors $TiCl_3$, HCl, and H_2O), and low reaction temperature (~ 80 ^oC) are ideal for various applications, especially solar energy conversion.

EXPERIMENTAL SECTION

Materials. All chemicals were purchased and used without further purification including $TiCl_3$ (20 % in 3% HCl acid, Alfa Aesar), HCl (ACS Reagent Grade 36.5-38%, MP), Di-tetrabutylammonium cis-bis(isothiocyanato)bis(2,2′-bipyridyl-4,4′-dicarboxylato)ruthenium(II) aka. N719 dye (Sigma Aldrich), Idolyte AN-50 (Solaronix).

Hydrothermal Synthesis of TiO_2 Nanoplatelet Arrays. Fluorine doped-Tin Oxide (FTO) coated glass substrates (with size of up to 3 cm x 3 cm) and other substrates were first cleaned by sonication in a mixture of ethanol and water for 30 min, subsequently rinsed with deionized water, dried in an air stream and placed on the bottom of the 50 mL Pyrex glass vial reactor. In a typical hydrothermal growth procedure, the reaction solutions containing 10 mL of deionized water, 0.05-2.5 mL of $TiCl_3$ solution (20 % in 3% hydrochloric acid, Alfa Aesar), and 0-0.4 mL of HCl (ACS reagent grade 36.5-38%, MP) were magnetically stirred for 30 minutes before being transferred into the Pyrex glass reactor. The hydrothermal growth was conducted at 80 ^oC for 2 to 10 hours in a box furnace. After the reaction was complete and the reactor was cooled down, the TiO_2 nanoplatelet films were taken out and rinsed with copious amount of water. The TiO_2 film deposited on the glass side of the FTO substrate was scraped off using a razor blade prior to further experimentation.

Post-treatments. The TiO_2 nanoplatelets were then kept at 30 ^oC in a vacuum oven overnight, followed by ultraviolet/ozone treatment for 30 minutes to remove contaminants. Some of the samples were annealed in air at 450-550 ^oC in a box furnace for 30 minutes.

Material Characterizations. SEM was performed on a Zeiss field-emission SEM using a 10 kV focus voltage. TEM and HRTEM were performed on a JEOL 2010F field-emission TEM using a 200 kV focus voltage. Grazing incidence X-ray diffraction

(GIXRD) patterns were collected with a Bruker D8 diffractometer. The transmittance spectra were collected using a Cary 5000 UV-vis-NIR spectrophotometer. Photoluminescence spectra were acquired at room temperature using a FluoroLog 3 (Horiba Scientific) spectrofluorimeter. X-ray photoelectron spectroscopy (XPS) was performed on a Kratos Axis x-ray photoelectron spectrometer with a scanning step of 0.1 eV and a dwell time of 0.4 seconds/step. The binding energy was calibrated using the C 1s photoelectron peak at 284.5 eV as a reference.

Electrochemical and Photoelectrochemical (PEC) Characterizations. The PEC measurements were performed using a three-electrode electrochemical cell with the FTO supported nanoplatelet array as the working electrode, a Ag/AgCl (saturated KCl) reference electrode, a platinum wire counter electrode, and 1 M KOH electrolyte (pH = 13.5). The working electrode with exposed area of 0.205 cm^2 was illuminated from the back side (through the FTO substrate – TiO_2 nanoplatelet interface) by a solar simulator (Newport, Model 9600, 150 W xenon lamp) equipped with an AM 1.5 G filter (Newport, Model 81094). The light intensity was measured as 100 mW/cm^2 using a thermopile detector with a spectrum response from 0.19 to 10.6 μm (Newport, 818P-020-12). A CHI 660D electrochemical station was used for linear sweep voltammetry (I-V) and chronoamperometry (I-t) measurements.

Incident photon to current conversion efficiencies (IPCEs) were calculated from chronoamperometry measurements using a motorized monochromator (Oriel Cornerstone 130 1/8 m). The monochromator slit size was adjusted to 0.75 mm x 2 mm providing monochromatic wavelengths with a bandwidth of ~ 8 nm and a power density which could be adjusted from 197 to 705 $\mu W/cm^2$ for wavelengths from 320 to 800 nm. A typical light power density spectrum used for IPCE can be found in Figure 5.1. Light

power was measured using a handheld optical power meter with a UV enhanced silicon photo-detector (Newport). IPCE values were calculated using the following equation:

$$IPCE(\lambda) = \frac{1240\, j_p(\lambda)}{\lambda\, E_\lambda(\lambda)}$$

where $j_p(\lambda)$ is the measured photocurrent density (mA/cm^2) and $E_\lambda(\lambda)$ is the incident light power density (mW/cm^2) for each wavelength, λ (nm).

The measured potentials *vs.* the Ag/AgCl were converted to the reversible hydrogen electrode (RHE) scale *via* the Nernst equation

$$E_{RHE} = E_{Ag/AgCl} + 0.059\ pH + E^o_{Ag/AgCl}$$

where E_{RHE} is the converted potential vs. RHE, $E_{Ag/AgCl}$ is the experimental potential measured against the Ag/AgCl reference electrode, and $E^o_{Ag/AgCl}$ = 0.1976 V at 25 ^{o}C.

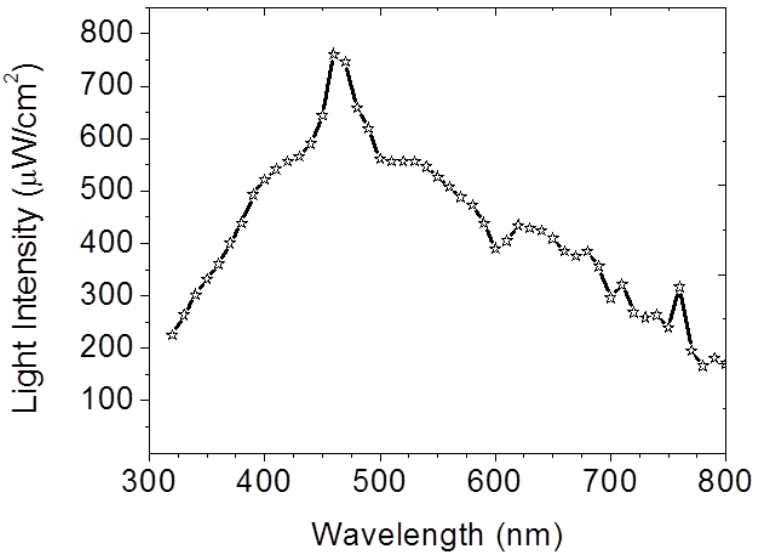

Figure 5.1. Typical light intensity for IPCE and EQE measurements

Dye sensitized solar cell (DSSC) fabrication. The TiO_2 nanoplatelet samples were immersed overnight in an ethanol solution containing 0.5 mM N719 dye (di-tetrabutylammonium cis-bis (isothiocyanato) bis (2,2′-bipyridyl-4,4′-dicarboxylato) ruthenium(II), Sigma Aldrich) for dye adsorption. Dye-sensitized TiO_2 nanoplatelet arrays with an active area of ~ 0.25-0.64 cm^2 were assembled in a sandwich-type configuration with a Pt-coated FTO glass counter electrode (Solaronix) and a 25 μm thick SX-1170 (Solaronix) spacer. The cells were filled with a commercial iodine/tri-iodine in acetonitrile based electrolyte (Iodolyte AN-50, Solaronix).

Dye sensitized solar cell characterizations. J-V measurements were obtained using a CHI 660D chemical station by independently applying external voltage to the cell and measuring the photocurrent. The electrochemical impedance spectroscopy of the DSSCs were obtained under AM 1.5 G illumination at open circuit potentials.

RESULTS AND DISCUSSION

Characterization of TiO_2 Nanoplatelet Arrays. Figure 5.2a and b show the cross sectional view and top view scanning electron microscopy (SEM) images of a typical as-synthesized TiO_2 nanoplatelet arrays on a FTO substrate, which were deposited at 80 ^oC for 3 h in 8 mM $TiCl_3$ solution with pH of 0.85. The TiO_2 arrays consist of vertically aligned nanoplatelets with heights (film thicknesses) of ~ 1 μm, lengths of ~ 130 nm, and widths < 5 nm. The TiO_2 nanoplatelet arrays can be classified as rutile TiO_2 (JCPDS #88-1875) with an enhancement in the exposure of the (101) facet, indicating that the nanoplatelets are well crystallized. The high resolution transmission electron microscopy (HRTEM) in Figure 5.1c indicates that the as-synthesized nanoplatelet is single crystalline, has a (110) interplanar d-spacing of 3.22 Å, and preferentially grows along the [001] direction.

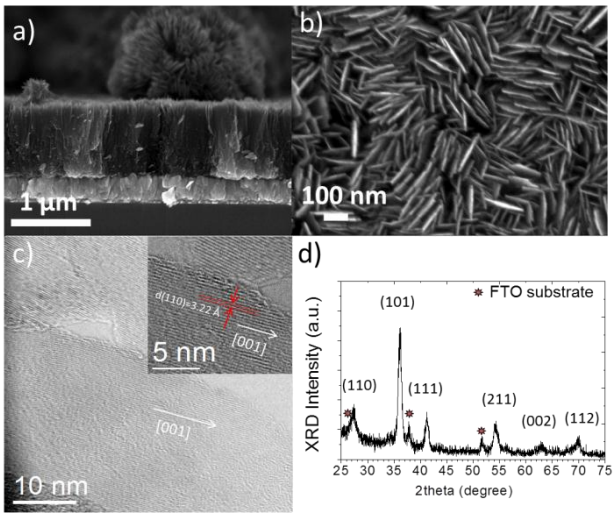

Figure 5.2. Single crystalline rutile TiO_2 nanoplatelet arrays on FTO glass: (a) cross-sectional and (b) top view SEM images, (c) HRTEM image; the inset shows lattice resolved HRTEM image, and (d) X-ray diffraction (XRD) pattern.

Figure 5.3a shows the XPS spectrum for core Ti 2p electrons from the TiO_2 nanoplatelet sample. The Ti 2p3/2 and 2p1/2 XPS features at 458.4 eV and 464.1 eV respectively are assigned to Ti^{4+}. Although, the Ti precursor is Ti^{3+} (in $TiCl_3$), we observed only Ti^{4+} in the nanoplatelets. Figure 5.2b shows the XPS spectrum of core O 1s which can be fitted by 2 curves peaking at 529.6 eV and 531.3 eV which can be assigned for surface O in Ti-O and in –OH bonds respectively.[26]

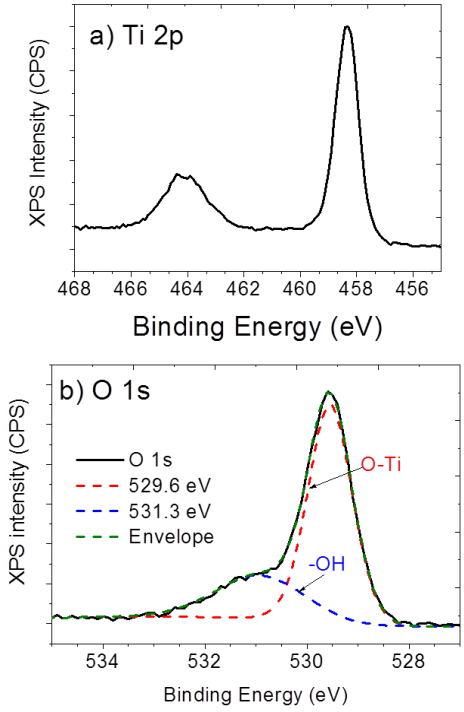

Figure 5.3. XPS spectra of (a) core Ti 2p and (b) core O 1s and its fitting curves for TiO_2 nanoplatelet arrays.

The morphology of the TiO_2 films significantly changes with the acidity (pH) of the reaction solution. Figure 5.4 shows the top-view SEM image of the TiO_2 films obtained at different pH ranging from 1.2 to 0.66 (pH of the solution was adjusted by adding 0.05-0.3 mL of HCl solution to 10 mL of the reaction solution). We did not obtain any TiO_2 deposition on the FTO substrate when the pH was out of this pH range. The TiO_2 nanoplatelet morphology can only be obtained for pH in the range of 0.71-0.85 (with addition of 0.2-0.25 mL of HCl solution). We observed an increase in the formation of a needle-like morphology when the pH was decreased to a value lower than 0.71. In order to exclude the effect of changing the concentration of Cl^- ions due to addition of different amounts of HCl, we provided supplemental Cl^- ion by adding various amounts of NaCl to the reaction solutions until the reaction solution is saturated with NaCl. There

is no change in the morphology of the TiO_2 films with the addition of different amounts of NaCl, thus confirming that the nanostructure of TiO_2 films strongly depends on pH of the reaction solution but not on Cl^- from the HCl solution.

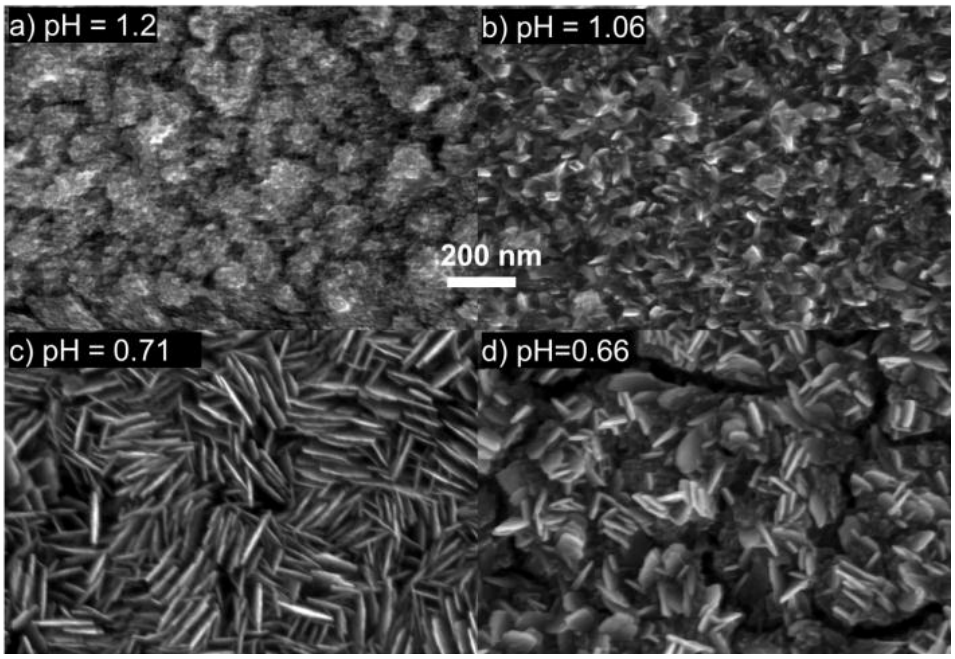

Figure 5.4. Top-view SEM images of TiO_2 films obtained at various pH of the precursor solution: (a) pH=1.2, (b) pH=1.06, (c) pH=0.71, and (d) pH=0.66. The scale bar applies to all micrographs. We note that there is no TiO_2 film obtained when pH of the precursor solution is smaller than 0.6 or larger than 1.2.

Hydrothermal/solvothermal grown one dimensional (1D) nanostructures of rutile TiO_2 have received much attention since it demonstrates good performance for water photo-oxidation and DSSC applications.[12-14] Typically the TiO_2 nanowire arrays are hydrothermally/solvothermally grown using a Ti (IV) alkoxide such as titanium (IV) isopropoxide and titanium (IV) butoxide with or without $TiCl_4$ as the titanium precursors. The growth of oriented TiO_2 nanowires requires (1) slow hydrolysis of Ti precursors

acquired by using a strong acidic medium and (2) capping agents/surfactants.[14] Generally, the growth of 2D morphologies of rutile is not easy since it requires even slower reaction rates.[27] Controlling the oxidation and hydrolysis of the Ti(III) precursor (such as $TiCl_3$) is the key to obtaining the nanoplatelet morphology. Aoyama et al.[27] investigated a 9-day chemical bath deposition of TiO_2 nanosheets on glass substrates at room temperature using 0.1M $TiCl_3$ as the Ti precursor, reporting that the initial deposition started after 4 days, and then nanorod assembly started forming on the surface after 6 days. Finally, the formation of nanosheets from the nanorods started after 7 days.[27] During TiO_2 crystal growth, Ti^{III} species were gradually oxidized by dissolved O_2 to Ti^{IV} species which were then hydrolyzed to form TiO_2. Aoyama et al. also reported that when the initial pH was changed from 0.7 to 2 or the reaction temperature was increased from 25 ^oC to 40 ^oC to increase the reaction rate, needle-like morphologies or random aggregates were formed.

In our study, the growing process was facilitated by increasing reaction temperature to 80 ^oC but utilizing a much lower $TiCl_3$ concentration (8-40 mM) and low pH (0.60-1.2). Figure 5.5 shows the time-evolution growth of the TiO_2 nanoplatelet arrays. The SEM image of the FTO substrate was included in Figure 5.5a for reference. We observed a TiO_2 nanoplatelet crystal growth process similar to that reported by Aoyama and coworkers [27] but on a much faster time scale. Initially, a TiO_2 nuclei layer is slowly deposited on FTO substrate in the first 135 minutes (Figure 5.5b). After 150 minutes, TiO_2 nano-needles were formed (Figure 5.5c) and quickly converted to nanoplatelets after 165 minutes as shown in Figure 5.4d (thickness of the film is ~ 290 nm). The TiO_2 nanoplatelets are then quickly grown, reaching a thickness of ~ 1 μm after 180 minutes (Figure 5.2a).

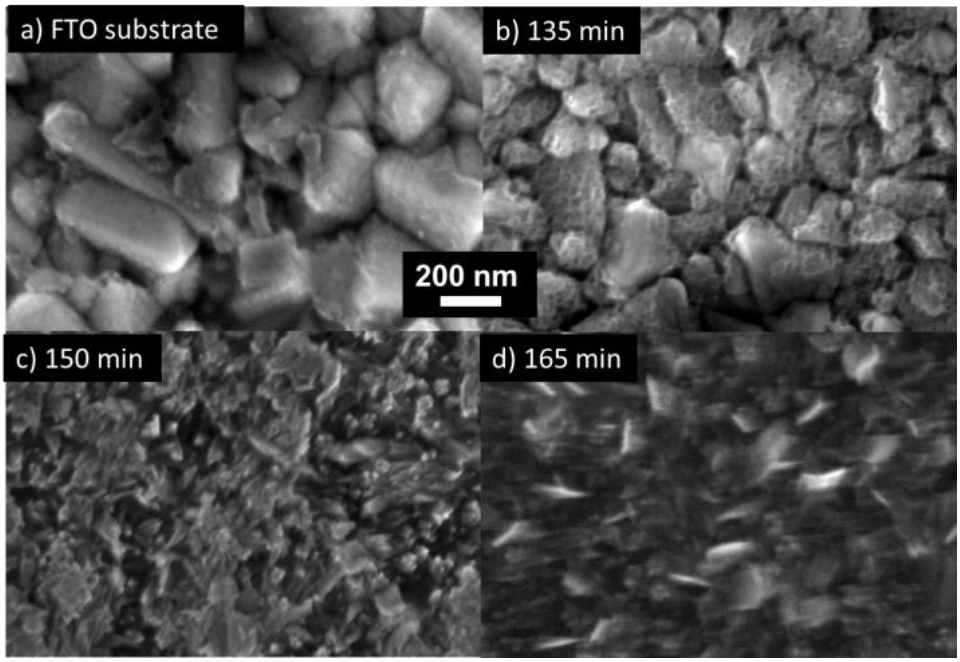

Figure 5.5. Top view SEM image of (a) FTO-coated glass substrate and time-evolution of TiO_2 nanoplatelet growth: (b) after 135 min, (c) after 150 min, and (d) after 165 min. The scale bar applies for all micrograph. See Figure 5.1b for the SEM image of the TiO_2 film grown for 180 min.

Prolonging the reaction duration from 3 hours to up to 10 hours does not increase the film thickness, but produces micron-size particles which consist of many nanoplaletlets (Figure 5.6) aggregating on the bottom of the reactor or on top of the films.

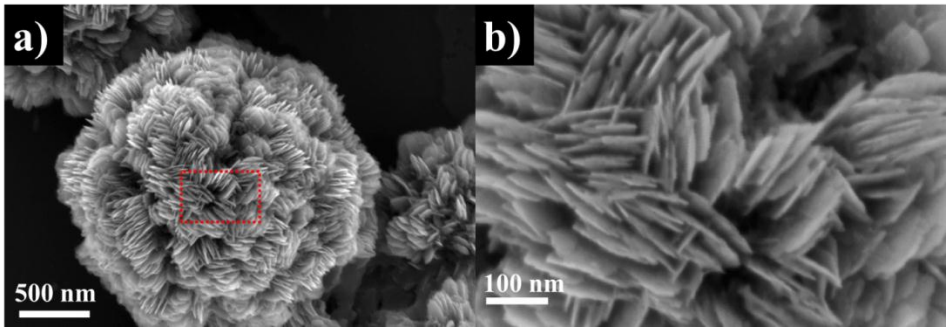

Figure 5.6. (a) SEM image of micron-size powder aggregating on the bottom of the reactor and (b) Higher magnification image of the area in the red box

We did not observe a split of the nanosheets to nanofibers when prolonging the growing time of TiO_2 nanosheet-arrays as reported by Zhu et al. when titanium (IV) isopropoxide was used as the Ti precursor.[28] Zhu et al. explained that this split is due to the increase in elastic strain stemming from the lattice mismatch between rutile TiO_2 and the FTO substrate when the size of the TiO_2 nanosheets increases. We have succeeded growing TiO_2 nanoplatelet films on various substrates with different roughness and crystal structure such as glass, Ti foil, PET plastic, Si wafers etc. using the same recipe (Figure 5.7). We, therefore, believe that employing $TiCl_3$ as the Ti precursor is the key in obtaining the nanoplatelet structure.

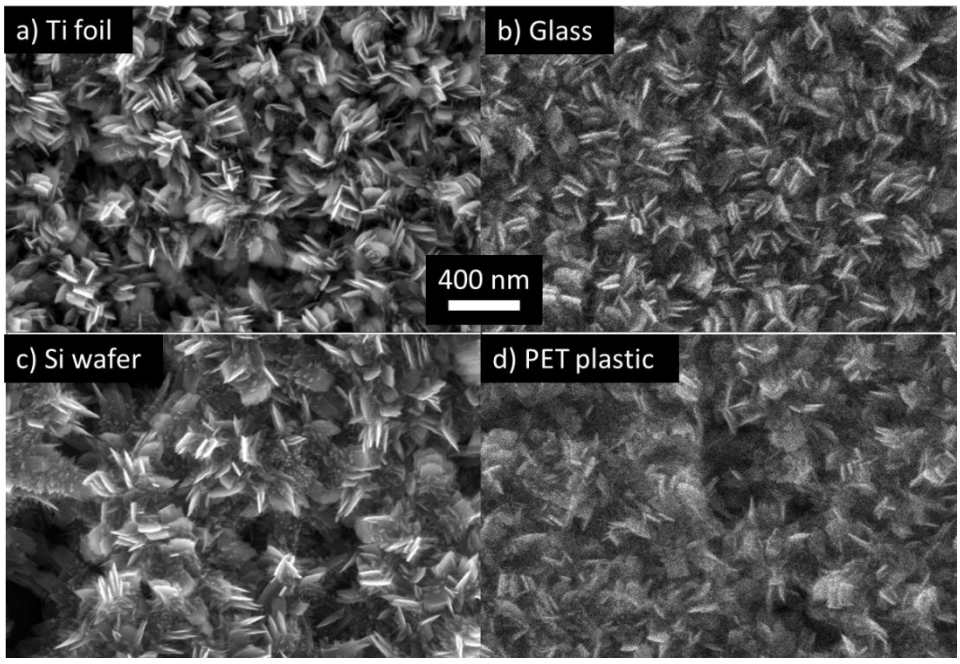

Figure 5.7. SEM images of TiO_2 nanoplatelet grown on various substrates: (a) Ti foil, (b) glass, (c) Si wafer, and (d) polyethylene terephthalate (PET) plastic.

In order to investigate the effects of $TiCl_3$ concentration, we prepared various TiO_2 nanoplatelet arrays by adding 0.05-0.25 mL of $TiCl_3$ solution to a reaction solution

containing 10 mL of DI water and 0.2 mL of HCl to obtain concentrations of $TiCl_3$ of from 8 to 40 mM. The pH of the reaction solution changes slightly when adding different volumes of $TiCl_3$, reaching a pH of 0.91 with addition of 0.05 mL of $TiCl_3$ solution and a pH of 0.70 with the addition of 0.25 mL of $TiCl_3$ solution. As shown in figure 5.8, the density of the nanoplatelets increases with the $TiCl_3$ concentration. It is interesting to note that the thickness of the nanoplatelet arrays (the heights of the nanoplatelets) is almost the same although the shape of the nanoplatelets changes slightly with $TiCl_3$ concentration which is probably due to the slight changes in pH of the precursor solution with the addition of different volumes of $TiCl_3$ solution.

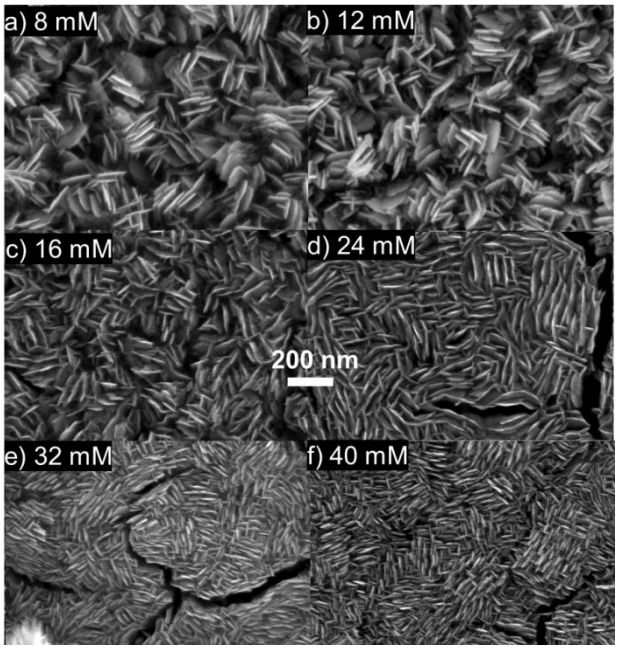

Figure 5.8. Top-view SEM images of TiO_2 nanoplatelet arrays grown with various concentrations of $TiCl_3$ solution: (a) 8 mM, (b) 12 mM, (c) 16 mM, (d) 24 mM, (e) 32 mM, and (f) 40 mM. The scale bar is applied for all micrographs. Note that the pH of the reaction solution is slightly changed with the addition of different amounts of $TiCl_3$ solution.

Figure 5.9a shows the UV-vis absorbance spectra of a typical TiO_2 nanoplatelet array with the absorption edge at ~ 415 nm, corresponding to a band gap of 3.0 eV, in agreement with the reported band gap value for rutile.[2] Figure 5.9b shows the photoluminescence (PL) spectra obtained using an excitation wavelength of 320 nm (3.88 eV) at room temperature of a typical TiO_2 nanoplatelet array. The PL from a semiconductor is a result of charge carrier recombination.[29] Previous studies have shown that due to the indirect transition nature of TiO_2, the PL response of bulk TiO_2 is difficult to observe at room temperature (note that TiO_2 has a direct band gap but is subjected to dipole-forbidden transitions[26, 30]). We however observed a clear room temperature PL spectrum which can be fit by 3 Gaussian peaks at 402 nm (3.08 eV), 440 nm (2.82 eV), and 486 nm (2.55 eV). Interestingly, the PL peak at 402 nm with a full width at half maximum (FWHM) of 50 nm coincides well with the band edge absorption shown in figure 5.9a and can thus be assigned as a band-to-band recombination. This band edge emission is very difficult to observe for indirect band gap semiconductors such as GaP and TiO_2. There have been only few studies demonstrating the band-to-band emission for TiO_2 ultrafine nanoparticles (~ 2 nm).[31] The PL band centered at 440 nm is attributed to surface trap states.[32] Finally the small peak at 486 nm is associated with surface oxygen vacancies since it originates from the charge transfer transition from Ti^{3+} to the oxygen anion in TiO_6^{8-}.[33]

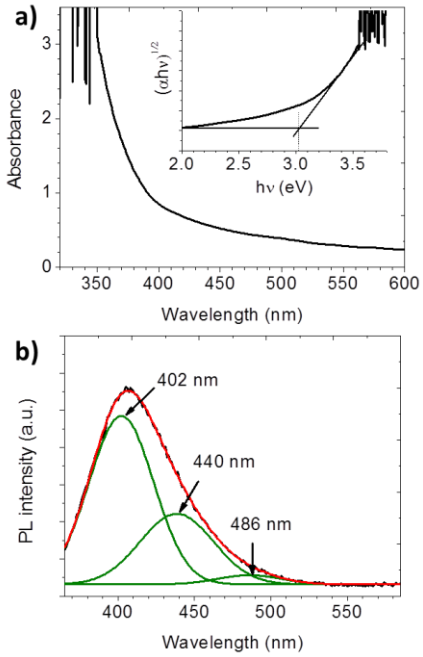

Figure 5.9. (a) UV-vis absorbance spectra of typical TiO_2 nanoplatelet arrays. The inset shows the Tauc plot created for the absorbance values and (b) Photoluminescence emission spectrum (the black curve under the red curve which is the sum of the Gaussian fitted curves shown in green) from a typical TiO_2 nanoplatelet film obtained at room temperature. The excitation wavelength is at 320 nm (3.88 eV).

Photoelectrochemical Water Oxidation Performance of TiO_2 Nanoplatelet Arrays. The PEC performance of the TiO_2 films on FTO was measured using a three-electrode electrochemical cell with the FTO supported TiO_2 nanoplatelet array as the working electrode with exposed area of 0.2 cm^2, a Ag/AgCl reference electrode, a Pt wire counter electrode, and 1 M KOH electrolyte (pH=13.5). A solar simulator (Oriel 96000) coupled with an AM 1.5 G filter was used as the light source with light intensity of 100 mW/cm^2 measured by a thermopile detector (Newport 818 P-020-12). Incident photon to current conversion efficiencies (IPCEs) were calculated from chronoamperometry measurements using a motorized monochromator (Oriel Cornerstone 130 1/8 m). The monochromator slit size was adjusted to 0.75 mm x 2 mm providing monochromatic

wavelengths with a bandwidth of ~ 5 nm and a power density which could be adjusted from 165 to 760 μW/cm^2 for wavelengths from 320 to 800 nm. Light power was measured using a handheld optical power meter with a UV enhanced silicon photo-detector (Newport). IPCE values were calculated using the following equation:

$$IPCE(\lambda) = \frac{1240\, j_p(\lambda)}{\lambda\, E_\lambda(\lambda)} \quad (1)$$

where $j_p(\lambda)$ is the measured photocurrent density (mA/cm^2) and $E_\lambda(\lambda)$ is the incident light power density (mW/cm^2) for each wavelength, λ (nm).

The measured potentials *vs.* saturated Ag/AgCl were converted to the reversible hydrogen electrode (RHE) scale *via* the Nernst equation:

$$E_{RHE} = E_{Ag/AgCl} + 0.059\ pH + E^o_{Ag/AgCl} \quad (2)$$

where E_{RHE} is the converted potential vs. RHE, $E_{Ag/AgCl}$ is the experimental potential measured against Ag/AgCl reference electrode, and $E^o_{Ag/AgCl}$ = 0.1976 V at 25 ^{o}C.

Before testing, the as-synthesized films were annealed in air at 550 ^{o}C for 30 minutes to improve crystallinity and adherence of the TiO_2 nanoplatelet array to the SnO_2 layer. Figure 5.11a shows the linear sweep voltammetry under intermittent illumination for a typical TiO_2 nanoplatelet array synthesized with a 16 mM $TiCl_3$ precursor solution at pH of 0.71. The onset potential is at -0.8 V vs Ag/AgCl (0.2 V_{RHE}), in good agreement with the flat band potential determined from the Mott-Schottky plot (Figure 5.10).

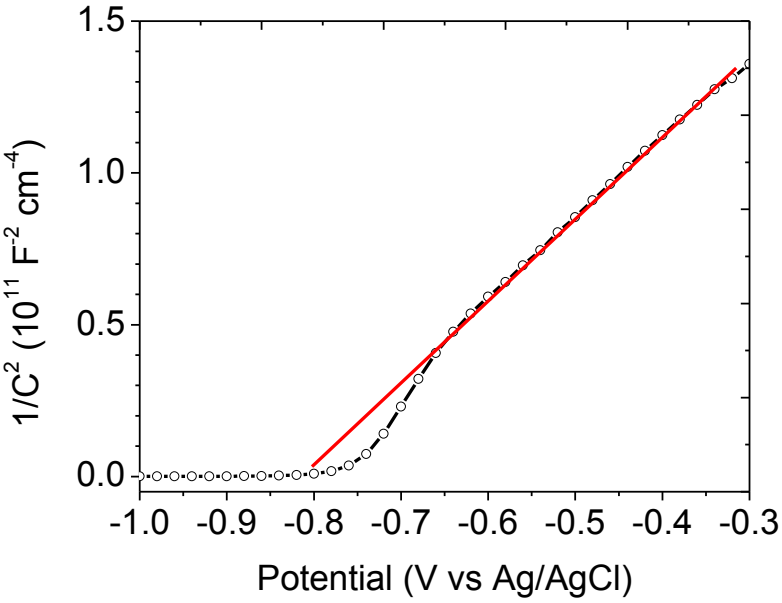

Figure 5.10. Mott-Schottky plot obtained in the dark in 1 M KOH electrolyte for a typical TiO_2 nanoplatelet sample.

It is interesting that the photocurrent increases sharply with applied bias, reaching the saturated photocurrent at an exceptionally low potential of -0.6 V vs Ag/AgCl (0.4 V vs RHE), compared to -0.25 V vs. Ag/AgCl for the single crystalline TiO_2 rutile nanowire array photoanode reported by Feng et al.[13] and compared to 0.5-1 V vs Ag/AgCl for nanoparticle-based TiO_2 photoanodes.[34] This indicates excellent charge separation characteristics resulting from a high degree of crystallinity and a unique morphology that enables vectorial charge transfer (photo-generated holes just need to diffuse one-half of the lateral dimension of the nanoplatelet and photo-generated electrons can transport to the back contact without scattering at grain boundaries [21]). Figure 5.11b shows the IPCE spectrum for the TiO_2 nanoplatelet photoanode in 1 M KOH at 1.2 V_{RHE}. The IPCE onset is at ~410 nm, in good agreement with a band gap of ~ 3.0 eV as measured above. The IPCE values are high (≥ 40 %) over a range of 330-380

nm, reaching a maximum of 57 % at 350 nm indicative high light absorption and good charge separation characteristics.

Figure 5.11c shows the PEC performance at 1.2 V_{RHE} for the TiO_2 nanoplatelet films grown at various values of pH. The TiO_2 films obtained at pH of 0.6 and pH $\geq$ 1.06 are very thin, thus showing very poor PEC performance due to poor light absorption. The average thickness of TiO_2 films obtained at pH of 0.66 is ~ 600 nm, compared to ~ 1 μm for the films obtained at pH of 0.71 and 0.85, thus absorbing fewer photons and exhibiting lower photocurrents. The TiO_2 nanoplatelet films obtained at pH of 0.71 demonstrates better PEC performance than the films grown at pH of 0.85, although both films have quite similar morphology and thickness. We are unable to obtain exclusive evidence to explain this phenomenon. We hypothesize that changing pH might affect the initial nucleation rate and affect the aggregation at the base of the nanoplatelets which inhibits the diffusion of electrolyte deep into the TiO_2 nanoplatelet array (which cannot be observed by conventional SEM).

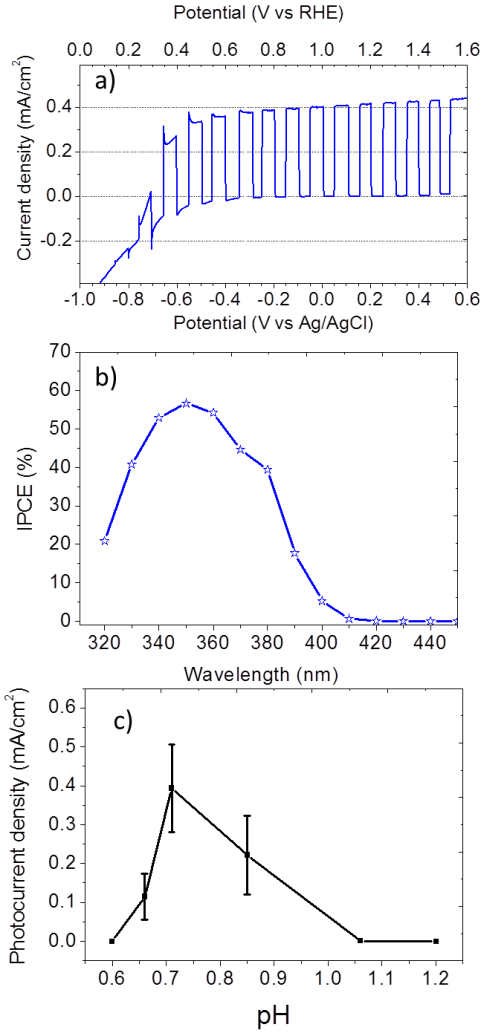

Figure 5.11. (a) Linear sweep voltammetry under intermittent AM 1.5 G illumination and (b) IPCE spectrum at 1.2 V_{RHE} for a typical TiO_2 nanoplatelet film synthesized with a 16 mM $TiCl_3$ precursor solution at pH of 0.71. (c) PEC performance at 1.2 V_{RHE} of TiO_2 films synthesized at various pH. All measurements were conducted using 3-electrode electrochemical cell with a Ag/AgCl reference electrode, a Pt wire counter electrode, and 1 M KOH electrolyte.

Dye sensitized solar cell performance of TiO_2 nanoplatelet arrays. Prior to testing the performance for dye sensitized solar cell (DSSC), the as-hydrothermally synthesized TiO_2 nanoplatelet samples were kept at 30 ^oC in a vacuum oven overnight to

evaporate residue water, followed by UV/ozone treatment for 30 minutes to remove contaminants. Some of the films denoted as annealed-TiO_2 nanoplatelets were annealed in air at 450 ^oC for 30 minutes. The TiO_2 nanoplatelet arrays were then immersed overnight in an ethanol solution of 0.5 mM N719 dye (di-tetrabutylammonium cis-bis (isothiocyanato) bis (2,2′-bipyridyl-4,4′-dicarboxylato) ruthenium(II), Sigma Aldrich) for dye adsorption. Dye-sensitized TiO_2 nanoplatelet arrays with an active area of ~ 0.25-0.64 cm^2 were assembled in a sandwich-type configuration with a Pt-coated FTO glass counter electrode (Solaronix) and a 25 μm thick SX-1170 (Solaronix) spacer. The cells were filled with a commercial iodine/tri-iodine in acetonitrile based electrolyte (Iodolyte AN-50, Solaronix).

Figure 5.12a shows the J-V characteristics and photoconversion efficiency of a typical dye sensitized, "as-hydrothermally synthesized" TiO_2 nanoplatelet sample (no thermal post-treatment) under AM 1.5 G illumination. The photoconversion efficiency is 1.28% with an open circuit potential (V_{oc}) of 0.68 V, short circuit current density (J_{sc}) of 2.92 mA cm^{-2}, and a fill factor (FF) of 64%. This is quite promising performance for a TiO_2 film that does not require thermal post-treatment. As we mentioned in the previous section, we were able to grow the nanoplatelet arrays on various types of substrates (including PET plastic). The as-synthesized TiO_2 nanoplatelets are already crystallized and are thus ready to be used for DSSC application. This ability is especially useful for DSSC applications requiring flexible substrates which are normally polymer based materials and cannot handle the high temperatures that might be required in post-treatment processes.

The annealed-TiO_2 nanoplatelets show significant improvement in DSSC performance (Figure 5.12a) with an overall photoconversion efficiency of 3.7%, V_{oc} of 0.76 V, J_{sc} of 7.66 mA cm^{-2}, and FF of 64%. Figure 5.12b shows the external quantum

efficiencies (EQE) of the annealed TiO_2 nanoplatelet sample measured under short-circuit conditions. The photocurrent obtained by integrating the calculated EQE multiplied by AM 1.5 G solar energy flux is 7.55 mA/cm^2 which is in good agreement with the measured J_{sc} value (7.66 mA cm^{-2}).

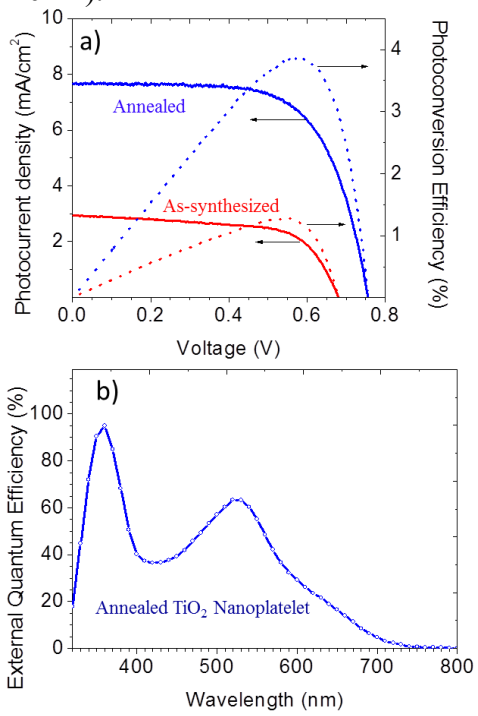

Figure 5.12. (a) Photocurrent density (solid line) and photoconversion efficiency (dotted line) of the DSSCs made of as-synthesized TiO_2 nanoplatelets (red) and annealed TiO_2 nanoplatelets (blue) under AM 1.5 G illumination (100 mW/cm^2); (b) External quantum efficiency of the DSSC made of annealed TiO_2 nanoplatelets.

Figure 5.13 shows the electrochemical impedance spectroscopy (EIS) spectra obtained under AM 1.5 G illumination at V_{oc} of the DSSCs made of as-synthesized (red) and annealed (blue) TiO_2 nanoplatelet samples. Both spectra show 2 semi-circles, of which the smaller and larger semicircles are attributed to the charge transfer at the counter electrode (CE)/electrolyte interface and the TiO_2/dye/electrolyte interface,

respectively. The sheet resistance (Rs) of the substrates and the electrolyte, charge transfer resistance of the CE (R1), resistance at the TiO_2/dye/electrolyte interface (R2), and constant phase elements (CPE 1 and CPE 2) were analyzed using Z-view software with an equivalent circuit shown in the inset of Figure 5.13. Both cells have similar Rs of ~ 11.5 Ω and R1 of ~ 1.8 Ω as expected due to the use of the same counter electrode and electrolyte. It is interesting that the cell made of as-synthesized TiO_2 nanoplatelets exhibits a higher value for R2 of ~ 43 Ω compared to R2 of ~ 17 Ω for the annealed TiO_2 nanoplatelets. Normally, the increase in R2 indicates a better barrier for the back-transferring of electrons from TiO_2 to the electrolyte, thus improving the DSSC performance.[35] However, we observed lower performance for the as-synthesized TiO_2 nanoplatelets cell. We propose that since the as-synthesized TiO_2 film did not undergo thermal treatment, there are still some hydroxyl (-OH) groups on the TiO_2 nanoplatelet surfaces and probably moisture and oxygen trapped into the nanoplatelet arrays that could introduce adverse effects regarding N719 dye adsorption and/or degrade the N719 dye. The products of N719 dye degradation might be pyridine derivatives which are not effective for photon conversion but could absorb on the TiO_2 surface thus inhibiting electron back transfer from TiO_2 to the electrolyte. Jo et al. reported similar phenomena with the performance of their DSSCs decreasing with increasing the N719 dye coating temperature.[35] The authors explained that the degradation of N719 dye at high temperature produces pyridine derivatives which act as a barrier for electron back scattering.

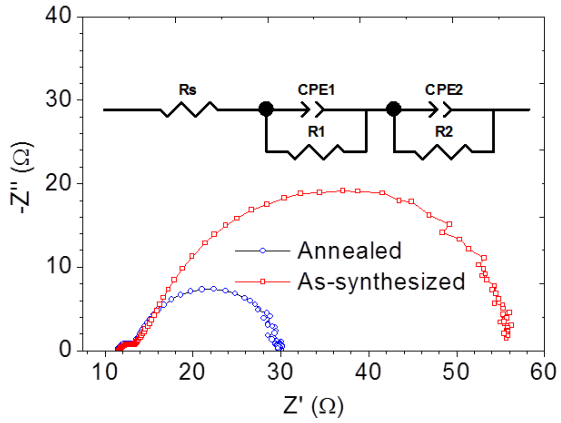

Figure 5.13. Electrical impedance spectroscopy (EIS) for DSSCs made of as-synthesized (red line) and annealed (blue line) TiO_2 nanoplatelets. The inset demonstrates the equivalent circuit of the cell consisting of the counter electrode (CE)/redox electrolyte interface and the TiO_2/dye/redox electrolyte interface, where R1 and R2 are the respective resistances, CPE1 and CPE2 are the respective constant phase elements, and Rs is the sheet resistance of FTO, Pt-coated FTO substrates and the resistance of electrolyte.

CONCLUSIONS

In conclusion, we report a facile, scalable, low cost, and low temperature (80 ^{o}C) hydrothermal synthesis of single crystalline TiO_2 rutile nanoplatelet arrays on FTO and various substrates including Ti foil, glass, PET plastic, and Si substrates. The nanoplatelet arrays consist of vertically aligned nanoplatelets with heights (film thicknesses) of up to 1 μm, lengths up to 130 nm, and widths ≤ 5 nm. The growth of the nanoplatelet arrays is sensitive to the acidity and $TiCl_3$ concentration of the precursor solution. We believe that controlling the oxidation and hydrolysis of Ti^{3+} by using a low $TiCl_3$ concentration (8-40 mM) and low pH (0.71-0.85) is the key to obtaining the nanoplatelet morphology. We also demonstrate the application of TiO_2 nanoplatelet arrays for water photo-oxidation and DSSC applications. As a photoanode for PEC water photo-oxidation, the TiO_2

nanoplatelet sample demonstrated excellent charge separation characteristics with a saturated photocurrent under AM 1.5 G illumination of ~ 0.4 mA/cm^2 was reached at an exceptionally low bias of -0.6 V vs Ag/AgCl (0.4 V_{RHE}), compared to -0.25 V vs. Ag/AgCl for a single crystalline TiO_2 rutile nanowire array photoanode.[13] Dye sensitized solar cells assembled using N719 dye sensitized-TiO_2 nanoplatelet arrays show promising performance with photoconversion efficiencies of 1.28 % for as-synthesized and 3.7 % for annealed TiO_2 nanoplatelets.

REFERENCES

1. Fujishima, A.; Honda, K., Electrochemical Photolysis of Water at a Semiconductor Electrode. *Nature* **1972,** 238, (5358), 37-38.

2. Chen, X.; Mao, S. S., Titanium Dioxide Nanomaterials: Synthesis, Properties, Modifications, and Applications. *Chem. Rev.* **2007,** 107, (7), 2891-2959.

3. Fujishima, A.; Zhang, X.; Tryk, D. A., TiO_2 photocatalysis and related surface phenomena. *Surf. Sci. Rep.* **2008,** 63, (12), 515-582.

4. Linsebigler, A. L.; Lu, G.; Yates, J. T., Photocatalysis on TiO_2 Surfaces: Principles, Mechanisms, and Selected Results. *Chem. Rev.* **1995,** 95, (3), 735-758.

5. Asahi, R.; Morikawa, T.; Ohwaki, T.; Aoki, K.; Taga, Y., Visible-light photocatalysis in nitrogen-doped titanium oxides. *Science* **2001,** 293, (5528), 269-271.

6. O'Regan, B.; Gratzel, M., A low-cost, high-efficiency solar cell based on dye-sensitized colloidal TiO_2 films. *Nature* **1991,** 353, 737.

7. Lin, Y.-M.; Abel, P. R.; Flaherty, D. W.; Wu, J.; Stevenson, K. J.; Heller, A.; Mullins, C. B., Morphology Dependence of the Lithium Storage Capability and Rate Performance of Amorphous TiO_2 Electrodes. *J. Phys. Chem. C* **2011,** 115, (5), 2585-2591.

8. Murphy, A. B.; Barnes, P. R. F.; Randeniya, L. K.; Plumb, I. C.; Grey, I. E.; Horne, M. D.; Glasscock, J. A., Efficiency of solar water splitting using semiconductor electrodes. *Int. J. Hydrogen Energy* **2006,** 31, (14), 1999-2017.

9. Cho, I. S.; Chen, Z.; Forman, A. J.; Kim, D. R.; Rao, P. M.; Jaramillo, T. F.; Zheng, X., Branched TiO_2 Nanorods for Photoelectrochemical Hydrogen Production. *Nano Lett.* **2011,** 11, (11), 4978-4984.

10. Hoang, S.; Berglund, S. P.; Hahn, N. T.; Bard, A. J.; Mullins, C. B., Enhancing Visible Light Photo-oxidation of Water with TiO_2 Nanowire Arrays via Cotreatment with H_2 and NH_3: Synergistic Effects between Ti^{3+} and N. *J. Am. Chem. Soc.* **2012,** 134, (8), 3659-3662.

11. Mor, G. K.; Shankar, K.; Paulose, M.; Varghese, O. K.; Grimes, C. A., Enhanced photocleavage of water using titania nanotube arrays. *Nano Lett.* **2005,** 5, (1), 191-195.

12. Hoang, S.; Guo, S.; Hahn, N. T.; Bard, A. J.; Mullins, C. B., Visible Light Driven Photoelectrochemical Water Oxidation on Nitrogen-Modified TiO_2 Nanowires. *Nano Lett.* **2012,** 12, (1), 26-32.

13. Feng, X.; Shankar, K.; Varghese, O. K.; Paulose, M.; Latempa, T. J.; Grimes, C. A., Vertically Aligned Single Crystal TiO_2 Nanowire Arrays Grown Directly on Transparent Conducting Oxide Coated Glass: Synthesis Details and Applications. *Nano Lett.* **2008,** 8, (11), 3781-3786.

14. Liu, B.; Aydil, E. S., Growth of Oriented Single-Crystalline Rutile TiO2 Nanorods on Transparent Conducting Substrates for Dye-Sensitized Solar Cells. *J. Am. Chem. Soc.* **2009,** 131, (11), 3985-3990.

15. Ye, M.; Xin, X.; Lin, C.; Lin, Z., High Efficiency Dye-Sensitized Solar Cells Based on Hierarchically Structured Nanotubes. *Nano Lett.* **2011,** 11, (8), 3214-3220.

16. Park, J. H.; Kim, S.; Bard, A. J., Novel carbon-doped TiO2 nanotube arrays with high aspect ratios for efficient solar water splitting. *Nano Lett.* **2006,** 6, (1), 24-28.

17. Hoang, S.; Guo, S.; Mullins, C. B., Co-incorporation of N and Ta into TiO_2 Nanowires for Visible-light Driven Photoelectrochemical Water Oxidation. *J. Phys. Chem. C* **2012,** 116, (44), 23283-23290.

18. Yin, W.-J.; Tang, H.; Wei, S.-H.; Al-Jassim, M. M.; Turner, J.; Yan, Y., Band structure engineering of semiconductors for enhanced photoelectrochemical water splitting: The case of TiO_2. *Phys. Rev. B* **2010,** 82, (4), 045106.

19. Gai, Y.; Li, J.; Li, S.-S.; Xia, J.-B.; Wei, S.-H., Design of Narrow-Gap TiO_2: A Passivated Codoping Approach for Enhanced Photoelectrochemical Activity. *Phys. Rev. Lett.* **2009,** 102, (3), 036402.

20. van de Krol, R.; Liang, Y. Q.; Schoonman, J., Solar hydrogen production with nanostructured metal oxides. *J. Mater. Chem.* **2008,** 18, (20), 2311-2320.

21. Kamat, P. V., Meeting the Clean Energy Demand: Nanostructure Architectures for Solar Energy Conversion. *J. Phys. Chem. C* **2007,** 111, (7), 2834-2860.

22. Wang, G.; Wang, H.; Ling, Y.; Tang, Y.; Yang, X.; Fitzmorris, R. C.; Wang, C.; Zhang, J. Z.; Li, Y., Hydrogen-Treated TiO_2 Nanowire Arrays for Photoelectrochemical Water Splitting. *Nano Lett.* **2011,** 11, (7), 3026-3033.

23. Salvador, P., Hole diffusion length in n-TiO_2 single crystals and sintered electrodes: Photoelectrochemical determination and comparative analysis. *J. Appl. Phys.* **1984,** 55, (8), 2977-2985.

24. Feng, X.; Zhu, K.; Frank, A. J.; Grimes, C. A.; Mallouk, T. E., Rapid Charge Transport in Dye-Sensitized Solar Cells Made from Vertically Aligned Single-Crystal Rutile TiO_2 Nanowires. *Angew. Chem. Int. Ed.* **2012,** 51, (11), 2727-2730.

25. Zhu, K.; Frank, A. J., Converting light to electrons in oriented nanotube arrays used in sensitized solar cells. *MRS Bull.* **2011,** 36, (6), 446-452.

26. Yu, J.-G.; Yu, H.-G.; Cheng, B.; Zhao, X.-J.; Yu, J. C.; Ho, W.-K., The Effect of Calcination Temperature on the Surface Microstructure and Photocatalytic Activity of TiO_2 Thin Films Prepared by Liquid Phase Deposition. *J. Phys. Chem. B* **2003,** 107, (50), 13871-13879.

27. Aoyama, Y.; Oaki, Y.; Ise, R.; Imai, H., Mesocrystal nanosheet of rutile TiO2 and its reaction selectivity as a photocatalyst. *CrystEngComm* **2012,** 14, (4), 1405-1411.

28. Zhu, H.; Yang, J.; Feng, S.; Liu, M.; Zhang, J.; Li, G., Growth of TiO_2 nanosheet-array thin films by quick chemical bath deposition for dye-sensitized solar cells. *Appl. Phys. A* **2011,** 105, (3), 769-774.

29. Liqiang, J.; Yichun, Q.; Baiqi, W.; Shudan, L.; Baojiang, J.; Libin, Y.; Wei, F.; Honggang, F.; Jiazhong, S., Review of photoluminescence performance of nano-sized semiconductor materials and its relationships with photocatalytic activity. *Sol. Energy Mater. Sol. Cells* **2006,** 90, (12), 1773-1787.

30. Daude, N.; Gout, C.; Jouanin, C., Electronic band structure of titanium dioxide. *Phys. Rev. B* **1977,** 15, (6), 3229-3235.

31. Pan, D.; Zhao, N.; Wang, Q.; Jiang, S.; Ji, X.; An, L., Facile Synthesis and Characterization of Luminescent TiO_2 Nanocrystals. *Adv. Mater.* **2005,** 17, (16), 1991-1995.

32. Liu, J.; Li, J.; Sedhain, A.; Lin, J.; Jiang, H., Structure and Photoluminescence Study of TiO2 Nanoneedle Texture along Vertically Aligned Carbon Nanofiber Arrays. *J. Phys. Chem. C* **2008,** 112, (44), 17127-17132.

33. Yu, J. C.; Yu; Ho; Jiang; Zhang, Effects of F- Doping on the Photocatalytic Activity and Microstructures of Nanocrystalline TiO2 Powders. *Chem. Mater.* **2002,** 14, (9), 3808-3816.

34. Oliva, F. Y.; Avalle, L. a. B.; Santos, E.; Cámara, O. R., Photoelectrochemical characterization of nanocrystalline TiO_2 films on titanium substrates. *J. Photochem. Photobiol., A* **2002,** 146, (3), 175-188.

35. Jo, Y.; Jung, C.-l.; Lim, J.; Kim, B. H.; Han, C.-H.; Kim, J.; Kim, S.; Kim, D.; Jun, Y., A novel dye coating method for N719 dye-sensitized solar cells. *Electrochim. Acta* **2012,** 66, (0), 121-125.

Chapter 6: Concluding Remarks and Future Research

OVERVIEW OF COMPLETED WORK

In the previous chapters, we have discussed the solvo/hydrothermal synthesis methods and characterizations of single crystalline TiO_2 nanowires and nanoplatelets on fluorine-doped tin oxide (FTO) coated glass substrates for photoelectrochemical (PEC) applications. These solvo/hydrothermal synthesis methods employ low cost precursors, simple set-up and provide high yield and high quality materials, thus are amenable to large-scale applications. These nanostructured TiO_2 materials have shown excellent charge transport properties and thus PEC performance. We have also demonstrated a number of strategies to further improve the PEC performance of TiO_2 including optimization of charge transport properties and light absorption via controlling the material compositions and employing water oxidation co-catalysts.

In chapter 2, we employed a solvothermal synthesis to grow single crystalline TiO_2 nanowires on FTO with exceptionally small feature sizes of only ~ 5 nm. The morphology of the film can be controlled by manipulating synthesis parameters such as reaction temperature, Ti precursors and solvents, seeding methods etc. We have shown that the small feature sizes of the nanowires promote N diffusion into TiO_2 lattice, thus allowing significant amount of N incorporating into TiO_2 nanowires via nitridation in NH_3 flow at a relatively low temperature. The active spectra of N-incorporated TiO_2 nanowires extends to ~ 520 nm (2.4 eV), compared to 420 nm for the pristine TiO_2 nanowires, the PEC performance however decreases with N incorporation probably due to a decreased oxidative power of photogenerated holes. Employing cobalt water oxidation catalyst systems facilitates water oxidation and passivates surface states on the N-modified TiO_2 nanowires, thus enhancing the PEC performance.

In chapter 3, we demonstrated a novel strategy to improve visible light photo-oxidation properties of TiO_2 nanowires involving hydrogenation and nitridation cotreatment. The active spectrum of the cotreated-TiO_2 nanowires extends to 570 nm, compared to 550 nm for the nitrided TiO_2 nanowires and 420 nm for the pristine TiO_2 nanowires. Employing electron paramagnetic resonance spectroscopy and X-ray photon emission spectroscopy, we revealed the concentration of Ti^{3+} species in the bulk of the TiO_2 following hydrogenation and nitridation cotreatment (H, N:TiO_2) is considerably higher than that of the sample treated solely with ammonia. We proposed that the reversible electron transfer from Ti^{3+} to N dopant increases the electron density around N dopant, thus increasing Coulombic repulsion between N states and O states in the valence band of the H, N:TiO_2 sample. Due to the greater Coulombic repulsion, the N states in the H, N:TiO_2 sample have higher energy than that of the N-modified TiO_2 sample, thus enabling excitation with photons of longer wavelength.

In chapter 4, we presented a solvothermal synthesis route to incorporate Ta with concentration ranging from 0.11 to 3.47 atomic % into TiO_2 nanowires. High resolution transmission electron microscopy (HRTEM) indicate homogeneous incorporation of Ta at low doping level (~ 0.61 atomic %). However, we observed a core/shell structure at high doping level (~ 2.65 atomic %). N and Ta coincorporated TiO_2 nanowires (N, Ta:TiO_2) were prepared via nitridation of Ta-incorporated TiO_2 nanowires at a relatively low temperature (500 ^{o}C). The N, Ta:TiO_2 samples demonstrate an enhanced PEC performance compared to the N-incorporated TiO_2 sample both in the UV and visible light region. We believe that the enhancement shown by the N, Ta:TiO_2 samples is due to fewer recombination centers from charge compensation effects and suppression of the formation of an amorphous layer on the nanowires during the nitridation process.

In chapter 5, we demonstrated a hydrothermal synthesis of vertically aligned TiO_2 nanoplatelet arrays on fluorine-doped tin oxide coated glass substrates and their applications for photoelectrochemical (PEC) water splitting and dye sensitized solar cells. The TiO_2 arrays consisting of single crystal rutile nanoplatelets with heights (film thicknesses) of up to 1 μm, lengths of up to 130 nm, and widths of ~ 5 nm were grown via controlling oxidation and hydrolysis of $TiCl_3$ at low pH (0.71-0.85) and low $TiCl_3$ concentration (8-40 mM). The morphology of the TiO_2 nanoplatelet arrays can be controlled by manipulating reaction parameters such as reaction time, pH of solution, and Ti precursor concentration. As a photoanode for water oxidation in a PEC water splitting cell, the TiO_2 nanoplatelets show excellent charge separation characteristics with a saturated photocurrent in 1 M KOH electrolyte under AM 1.5 G illumination of ~ 0.4 mA/cm^2 reached at an exceptionally low bias of -0.6 V vs Ag/AgCl (0.4 V vs. reversible hydrogen electrode). Dye sensitized solar cells assembled using N719 dye sensitized-TiO_2 nanoplatelet arrays also show promising performance with photoconversion efficiencies of 1.28 % for as-synthesized (no thermal post-treatment) and 3.7 % for annealed TiO_2 nanoplatelets. We also demonstrated that the TiO_2 nanoplatelet arrays can be grown on various substrates including but not limited to Ti foil, glass, Si, and polyethylene terephthalate plastic. The synthesis method requires only low cost precursors ($TiCl_3$, HCl), low reaction temperature (80 ^oC), and easily scales up, thus ideal for various applications, especially for solar energy conversions.

ONGOING AND FUTURE WORK

As we discussed, an efficient photocatalyst semiconducting material for the PEC water splitting must satisfy stringent requirements such as a narrow band gap and high optical absorption coefficient to absorb a large fraction of the sunlight spectrum, an

appropriate electronic band structure with band edges straddling the water redox potential, efficient charge transport properties, high photo-stability in an aqueous environment, and low cost. Unfortunately, no known single material has been discovered that satisfies all of these requirements. Figure 6.1 demonstrates various strategies to improve the PEC water splitting activity.[1] To design materials, improving light absorbance and charge transport properties are two of the main approaches.

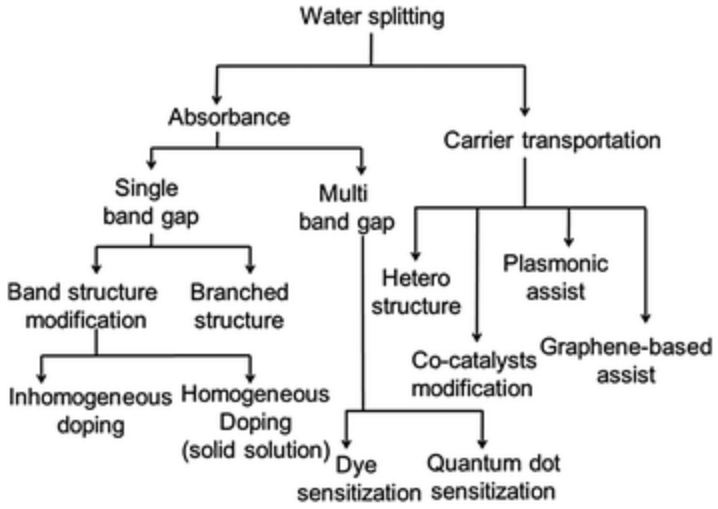

Figure 6.1. Various approaches for material design for water splitting application.

We are continuing studies on optimization the PEC performance of TiO_2 materials via improving both absorbance and charge transport properties. In particular, we are currently working on the synthesis and characterizations of Nb-incorporated TiO_2 hierarchical microspheres which consist of many nanowires for water photo-oxidation and dye sensitized solar cell applications. The incident-photon-to-current conversion efficiency (IPCE) spectra of dye sensitized solar cells employing the TiO_2 hierarchical microspheres (Figure 6.2) indicates efficient light harvesting properties probably due to light scattering and light trapping by the unique morphology.

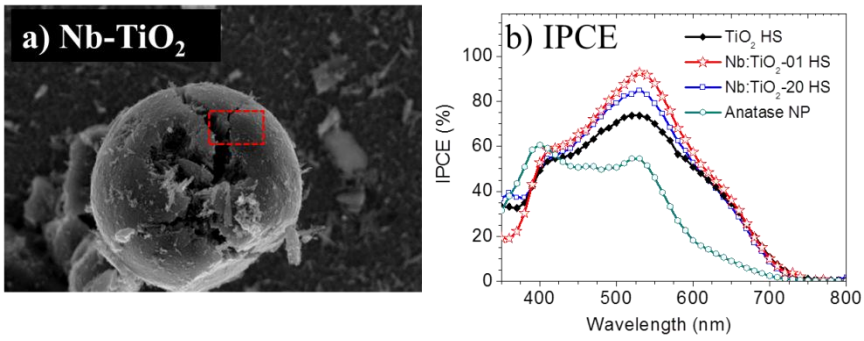

Figure 6.2. (a) Scanning electron micrograph of a Nb-incorporated TiO_2 hierarchical microsphere (HS), (b) incident-photon-to-current conversion efficiency (IPCE) spectra of dye sensitized solar cells employing TiO_2 anatase nanoparticles (cyan), TiO_2 HS (black) and Nb-incorporated TiO_2 materials (blue and red).

We have recently initiated a project involving preparation of TiO_2 and reduced graphene oxide nanocomposites for water splitting application. Employing solvol/hydrothermal synthesis, nanostructured TiO_2 or transitional metal (Ta, Nb, W etc.) incorporated TiO_2 materials will be deposited on to a reduced graphene oxide arrays grown on fluorine-doped tin oxide (FTO) coated glass substrate. The nanocomposites will be further annealed in NH_3 or C_2H_4 flow at an elevated temperature for incorporation of N or C that allow enhanced visible light excitations. The reduced graphene oxide scaffold acts as the electron channels, thus enabling faster electron transfer and minimizing photogenerated electron-hole recombination.[2] We believe that the nanocomposites are also promising for dye sensitized solar cell applications.

In addition, we would like to propose some other directions for design TiO_2 materials including (1) development of a 'soft' method for inclusion of N, C, etc, (2) development of titanate-based nanostructured photocatlysts emplying our reported TiO_2 nanostructures.

Develop a 'soft' method for incorporation of anion such as N, C, S etc. Anion incorporation seems to be more effective that cation incorporation in enhancing the visible light absorbance of TiO_2. However, the general method for anion incorporation is annealed TiO_2 materials in the anion-containing environment (for example NH_3 for N incorporation). This method normally creates nonhomogeneous 'doping' and defects. Employing the anion-containing precursor in solvo/hydrothermal growth might provide milder conditions to modify TiO_2 materials.

Develop titanate-based nanostructured photocatalysts which have a lower band gap than TiO_2 such as bismuth titanium oxides (e.g$Bi_{12}TiO_{20}$[3]). The energy level of Bi 6s is close to but higher than O 2p, thus allowing hybridization between Bi 6s and O 2p orbitals to form a new valence band and narrow the band gap. Bismuth titanates can be prepared via hydrothermal reactions of our TiO_2 nanowires, nanoplatelets, and hierarchical microspheres with Bi precursors.

REFERENCES

(1) Chen, H. M.; Chen, C. K.; Liu, R.-S.; Zhang, L.; Zhang, J.; Wilkinson, D. P. *Chem. Soc. Rev.* **2012**, *41*, 5654.

(2) Williams, G.; Seger, B.; Kamat, P. V. *ACS Nano* **2008**, *2*, 1487.

(3) Murugesan, S.; Smith, Y. R.; Subramanian, V. *J. Phys. Chem. Lett.* **2010**, *1*, 1631.

Bibliography

1. http://rredc.nrel.gov/solar/spectra/am1.5/.
2. Abe, R.; Higashi, M.; Domen, K., Facile Fabrication of an Efficient Oxynitride TaON Photoanode for Overall Water Splitting into H_2 and O_2 under Visible Light Irradiation. *J. Am. Chem. Soc.* **2010,** 132, (34), 11828-11829.
3. Anpo, M.; Che, M.; Fubini, B.; Garrone, E.; Giamello, E.; Paganini, M., Generation of superoxide ions at oxide surfaces. *Top. Catal.* **1999,** 8, (3), 189-198.
4. Arab, S.; Li, D. S.; Kinsinger, N.; Zaera, F.; Kisailus, D., Solvothermal synthesis of a highly branched Ta-doped TiO_2. *J. Mater. Res.* **2011,** 26, (20), 2653-2659.
5. Asahi, R.; Morikawa, T.; Ohwaki, T.; Aoki, K.; Taga, Y., Visible-light photocatalysis in nitrogen-doped titanium oxides. *Science* **2001,** 293, (5528), 269-271.
6. Asahi, R.; Taga, Y.; Mannstadt, W.; Freeman, A. J., Electronic and optical properties of anatase TiO_2. *Phys. Rev. B* **2000,** 61, (11), 7459.
7. Bard, A. J.; Fox, M. A., Artificial Photosynthesis-Solar Splitting of Water to Hydrogen and Oxygen. *Acc. Chem. Res.* **1995,** 28, (3), 141-145.
8. Batzill, M.; Morales, E. H.; Diebold, U., Influence of Nitrogen Doping on the Defect Formation and Surface Properties of TiO_2 Rutile and Anatase. *Phys. Rev. Lett.* **2006,** 96, (2), 026103.
9. Beranek, R.; Neumann, B.; Sakthivel, S.; Janczarek, M.; Dittrich, T.; Tributsch, H.; Kisch, H., Exploring the electronic structure of nitrogen-modified TiO_2 photocatalysts through photocurrent and surface photovoltage studies. *Chem. Phys.* **2007,** 339, (1-3), 11-19.
10. Bolton, J. R., Solar photoproduction of hydrogen: A review. *Solar Energy* **1996,** 57, (1), 37-50.
11. Bolton, J. R.; Strickler, S. J.; Connolly, J. S., Limiting and realizable efficiencies of solar photolysis of water. *Nature* **1985,** 316, (6028), 495-500.
12. Breault, T. M.; Bartlett, B. M., Lowering the Band Gap of Anatase-Structured TiO_2 by Coalloying with Nb and N: Electronic Structure and Photocatalytic Degradation of Methylene Blue Dye. *J. Phys. Chem. C* 116, (10), 5986-5994.
13. Burda, C.; Lou, Y.; Chen, X.; Samia, A. C. S.; Stout, J.; Gole, J. L., Enhanced Nitrogen Doping in TiO2 Nanoparticles. *Nano Lett.* **2003,** 3, (8), 1049-1051.
14. Chen, H. M.; Chen, C. K.; Liu, R.-S.; Zhang, L.; Zhang, J.; Wilkinson, D. P., Nano-architecture and material designs for water splitting photoelectrodes. *Chem. Soc. Rev.* **2012,** 41, (17), 5654-5671.

15. Chen, X.; Burda, C., Photoelectron Spectroscopic Investigation of Nitrogen-Doped Titania Nanoparticles. *J. Phys. Chem. B* **2004,** 108, (40), 15446-15449.

16. Chen, X.; Burda, C., The Electronic Origin of the Visible-Light Absorption Properties of C-, N- and S-Doped TiO_2 Nanomaterials. *J. Am. Chem. Soc.* **2008,** 130, (15), 5018-5019.

17. Chen, X.; Liu, L.; Yu, P. Y.; Mao, S. S., Increasing Solar Absorption for Photocatalysis with Black Hydrogenated Titanium Dioxide Nanocrystals. *Science* **2011,** 331, (6018), 746-750.

18. Chen, X.; Mao, S. S., Titanium Dioxide Nanomaterials: Synthesis, Properties, Modifications, and Applications. *Chem. Rev.* **2007,** 107, (7), 2891-2959.

19. Chen, X. B.; Lou, Y. B.; Dayal, S.; Qiu, X. F.; Krolicki, R.; Burda, C.; Zhao, C. F.; Becker, J., Doped semiconductor nanomaterials. *J. Nanosci. Nanotechnol.* **2005,** 5, (9), 1408-1420.

20. Cho, I. S.; Chen, Z.; Forman, A. J.; Kim, D. R.; Rao, P. M.; Jaramillo, T. F.; Zheng, X., Branched TiO_2 Nanorods for Photoelectrochemical Hydrogen Production. *Nano Lett.* **2011,** 11, (11), 4978-4984.

21. Choi, J.; Park, H.; Hoffmann, M. R., Combinatorial doping of TiO_2 with platinum (Pt), chromium (Cr), vanadium (V), and nickel (Ni) to achieve enhanced photocatalytic activity with visible light irradiation. *J. Mater. Res.* **2010,** 25, (1), 149-158.

22. Choi, W. Y.; Termin, A.; Hoffmann, M. R., The role of metal-ion dopants in quantum-sized TiO_2 - Correlation between photoreactivity and charge carrier recombination dynamics. *J. Phys. Chem.* **1994,** 98, (51), 13669-13679.

23. Cong, Y.; Zhang, J.; Chen, F.; Anpo, M., Synthesis and Characterization of Nitrogen-Doped TiO2 Nanophotocatalyst with High Visible Light Activity. *J. Phys. Chem. C* **2007,** 111, (19), 6976-6982.

24. Di Valentin, C.; Finazzi, E.; Pacchioni, G.; Selloni, A.; Livraghi, S.; Czoska, A. M.; Paganini, M. C.; Giamello, E., Density Functional Theory and Electron Paramagnetic Resonance Study on the Effect of Nâˆ’F Codoping of TiO2. *Chem. Mater.* **2008,** 20, (11), 3706-3714.

25. Diwald, O.; Thompson, T. L.; Zubkov, T.; Walck, S. D.; Yates, J. T., Photochemical Activity of Nitrogen-Doped Rutile TiO_2(110) in Visible Light. *J. Phys. Chem. B* **2004,** 108, (19), 6004-6008.

26. Dvoranova, D.; Brezova, V.; Mazur, M.; Malati, M. A., Investigations of metal-doped titanium dioxide photocatalysts. *Appl. Cat. B* **2002,** 37, (2), 91-105.

27. Emeline, A. V.; Sheremetyeva, N. V.; Khomchenko, N. V.; Ryabchuk, V. K.; Serpone, N., Photoinduced Formation of Defects and Nitrogen Stabilization of

Color Centers in N-Doped Titanium Dioxide. *J. Phys. Chem. C* **2007,** 111, (30), 11456-11462.

28. Feng, X.; Shankar, K.; Paulose, M.; Grimes, C. A., Tantalum-Doped Titanium Dioxide Nanowire Arrays for Dye-Sensitized Solar Cells with High Open-Circuit Voltage. *Angew. Chem. Int. Ed.* **2009,** 48, (43), 8095-8098.

29. Feng, X.; Shankar, K.; Varghese, O. K.; Paulose, M.; Latempa, T. J.; Grimes, C. A., Vertically Aligned Single Crystal TiO_2 Nanowire Arrays Grown Directly on Transparent Conducting Oxide Coated Glass: Synthesis Details and Applications. *Nano Lett.* **2008,** 8, (11), 3781-3786.

30. Fujishima, A.; Honda, K., Electrochemical Photolysis of Water at a Semiconductor Electrode. *Nature* **1972,** 238, (5358), 37-38.

31. Fujishima, A.; Zhang, X. T.; Tryk, D. A., TiO_2 photocatalysis and related surface phenomena. *Surf. Sci. Rep.* **2008,** 63, (12), 515-582.

32. Gai, Y.; Li, J.; Li, S.-S.; Xia, J.-B.; Wei, S.-H., Design of Narrow-Gap TiO_2: A Passivated Codoping Approach for Enhanced Photoelectrochemical Activity. *Phys. Rev. Lett.* **2009,** 102, (3), 036402.

33. Gai, Y. Q.; Li, J. B.; Li, S. S.; Xia, J. B.; Yan, Y. F.; Wei, S. H., Design of shallow acceptors in ZnO through compensated donor-acceptor complexes: A density functional calculation. *Phys. Rev. B* **2009,** 80, (15).

34. Hahn, N. T.; Ye, H.; Flaherty, D. W.; Bard, A. J.; Mullins, C. B., Reactive Ballistic Deposition of □-Fe_2O_3 Thin Films for Photoelectrochemical Water Oxidation. *ACS Nano* **2010,** 4, (4), 1977-1986.

35. Hoang, S.; Berglund, S. P.; Hahn, N. T.; Bard, A. J.; Mullins, C. B., Enhancing Visible Light Photo-oxidation of Water with TiO_2 Nanowire Arrays via Cotreatment with H_2 and NH_3: Synergistic Effects between Ti^{3+} and N. *J. Am. Chem. Soc.* **2012,** 134, (8), 3659-3662.

36. Hoang, S.; Guo, S.; Hahn, N. T.; Bard, A. J.; Mullins, C. B., Visible Light Driven Photoelectrochemical Water Oxidation on Nitrogen-Modified TiO_2 Nanowires. *Nano Lett.* **2012,** 12, (1), 26-32.

37. Huang, J.; Wen, S.; Liu, J.; He, G., Band gap narrowing of TiO2 by compensated codoping for enhanced photocatalytic activity. *J. Nat. Gas Chem.* **2012,** 21, (3), 302-307.

38. Hwang, Y. J.; Hahn, C.; Liu, B.; Yang, P., Photoelectrochemical Properties of TiO_2 Nanowire Arrays: A Study of the Dependence on Length and Atomic Layer Deposition Coating. *ACS Nano* **2012,** 6, (6), 5060-5069.

39. Irie, H.; Washizuka, S.; Yoshino, N.; Hashimoto, K., Visible-light induced hydrophilicity on nitrogen-substituted titanium dioxide films. *Chem. Commun.* **2003**, (11), 1298-1299.

40. Irie, H.; Watanabe, Y.; Hashimoto, K., Nitrogen-Concentration Dependence on Photocatalytic Activity of TiO_2-xN_x Powders. *J. Phys. Chem. B* **2003,** 107, (23), 5483-5486.

41. Janisch, R.; Gopal, P.; Spaldin, N. A., Transition metal-doped TiO_2 and ZnO - present status of the field. *J. Phys.: Condens. Matter* **2005,** 17, (27), R657-R689.

42. Kanan, M. W.; Nocera, D. G., In Situ Formation of an Oxygen-Evolving Catalyst in Neutral Water Containing Phosphate and Co^{2+}. *Science* **2008,** 321, (5892), 1072-1075.

43. Kay, A.; Cesar, I.; Grätzel, M., New Benchmark for Water Photooxidation by Nanostructured □-Fe_2O_3 Films. *J. Am. Chem. Soc.* **2006,** 128, (49), 15714-15721.

44. Khan, S. U. M.; Al-Shahry, M.; Ingler, W. B., Efficient photochemical water splitting by a chemically modified n-TiO_2 *Science* **2002,** 297, (5590), 2243-2245.

45. Lan, M.; Peng, X.; Hong, S.; Pei-Nan, W.; Weidian, S., First-principles calculation of N:H codoping effect on energy gap narrowing of TiO_2. *Appl. Phys. Lett.* **2007,** 90, 171909.

46. Leary, R.; Westwood, A., Carbonaceous nanomaterials for the enhancement of TiO_2 photocatalysis. *Carbon* **2011,** 49, (3), 741-772.

47. Li, H.; Li, J.; Huo, Y., Highly Active TiO_2N Photocatalysts Prepared by Treating TiO_2 Precursors in NH_3/Ethanol Fluid under Supercritical Conditions. *J. Phys. Chem. B* **2006,** 110, (4), 1559-1565.

48. Lindgren, T.; Lu, J.; Hoel, A.; Granqvist, C. G.; Torres, G. R.; Lindquist, S. E., Photo electrochemical study of sputtered nitrogen-doped titanium dioxide thin films in aqueous electrolyte. *Sol. Energy Mater. Sol. Cells* **2004,** 84, (1-4), 145-157.

49. Linsebigler, A. L.; Lu, G.; Yates, J. T., Photocatalysis on TiO_2 Surfaces: Principles, Mechanisms, and Selected Results. *Chem. Rev.* **1995,** 95, (3), 735-758.

50. Litter, M. I.; Navio, J. A., Photocatalytic properties of iron-doped titania semiconductors. *J. Photochem. Photobiol. A* **1996,** 98, (3), 171-181.

51. Livraghi, S.; Paganini, M. C.; Giamello, E.; Selloni, A.; Di Valentin, C.; Pacchioni, G., Origin of Photoactivity of Nitrogen-Doped Titanium Dioxide under Visible Light. *J. Am. Chem. Soc.* **2006,** 128, (49), 15666-15671.

52. Long, R.; English, N. J., Band gap engineering of (N, Ta)-codoped TiO_2: A first-principles calculation. *Chem. Phys. Lett.* **2009,** 478, (4-6), 175-179.

53. Ma, X. G.; Wu, Y.; Lu, Y. H.; Xu, J.; Wang, Y. J.; Zhu, Y. F., Effect of Compensated Codoping on the Photoelectrochemical Properties of Anatase TiO_2 Photocatalyst. *J. Phys. Chem. C* **2011,** 115, (34), 16963-16969.

54. Meinan, L.; Hongxia, W.; Cheng, Y.; Geoffrey, W.; John, B., One-step synthesis of titanium oxide with trilayer structure for dye-sensitized solar cells. *Appl. Phys. Lett.* **2011,** 98, 133113.

55. Mi, L.; Zhang, Y.; Wang, P.-N., First-principles study of the hydrogen doping influence on the geometric and electronic structures of N-doped TiO2. *Chem. Phys. Lett.* **2008,** 458, (4-6), 341-345.

56. Miyauchi, M.; Ikezawa, A.; Tobimatsu, H.; Irie, H.; Hashimoto, K., Zeta potential and photocatalytic activity of nitrogen doped TiO_2 thin films. *PCCP* **2004,** 6, (4), 865-870.

57. Mor, G. K.; Prakasam, H. E.; Varghese, O. K.; Shankar, K.; Grimes, C. A., Vertically oriented Ti-Fe-O nanotube array films: Toward a useful material architecture for solar spectrum water photoelectrolysis. *Nano Lett.* **2007,** 7, (8), 2356-2364.

58. Murphy, A. B.; Barnes, P. R. F.; Randeniya, L. K.; Plumb, I. C.; Grey, I. E.; Horne, M. D.; Glasscock, J. A., Efficiency of solar water splitting using semiconductor electrodes. *Int. J. Hydrogen Energy* **2006,** 31, (14), 1999-2017.

59. Murugesan, S.; Smith, Y. R.; Subramanian, V., Hydrothermal Synthesis of $Bi_{12}TiO_{20}$ Nanostrucutures Using Anodized TiO_2 Nanotubes and Its Application in Photovoltaics. *J. Phys. Chem. Lett.* **2010,** 1, (10), 1631-1636.

60. Nakamura, R.; Tanaka, T.; Nakato, Y., Mechanism for visible light responses in anodic photocurrents at N-doped TiO_2 film electrodes. *J. Phys. Chem. B* **2004,** 108, (30), 10617-10620.

61. Napoli, F.; Chiesa, M.; Livraghi, S.; Giamello, E.; Agnoli, S.; Granozzi, G.; Pacchioni, G.; Di Valentin, C., The nitrogen photoactive centre in N-doped titanium dioxide formed via interaction of N atoms with the solid. Nature and energy level of the species. *Chem. Phys. Lett.* **2009,** 477, (1â€“3), 135-138.

62. Obata, K.; Irie, H.; Hashimoto, K., Enhanced photocatalytic activities of Ta, N co-doped TiO_2 thin films under visible light. *Chem. Phys.* **2007,** 339, (1-3), 124-132.

63. Ohno, T.; Tanigawa, F.; Fujihara, K.; Izumi, S.; Matsumura, M., Photocatalytic oxidation of water on TiO_2-coated WO_3 particles by visible light using Iron(III) ions as electron acceptor. *J. Photochem. Photobiol. A* **1998,** 118, (1), 41-44.

64. Ohsawa, T.; Henderson, M. A.; Chambers, S. A., Epitaxial Growth and Orientational Dependence of Surface Photochemistry in Crystalline TiO_2 Rutile Films Doped with Nitrogen. *J. Phys. Chem. C* **2010,** 114, (14), 6595-6601.

65. Pan, H.; Zhang, Y.-W.; Shenoy, V. B.; Gao, H., Effects of H-, N-, and (H, N)-Doping on the Photocatalytic Activity of TiO_2. *J. Phys. Chem. C* **2011,** 115, (24), 12224-12231.

66. Park, J. H.; Kim, S.; Bard, A. J., Novel carbon-doped TiO_2 nanotube arrays with high aspect ratios for efficient solar water splitting. *Nano Lett.* **2006,** 6, (1), 24-28.

67. Russo, S. P.; Grey, I. E.; Wilson, N. C., Nitrogen/hydrogen codoping of anatase: A DFT study. *J. Phys. Chem. C* **2008,** 112, (20), 7653-7664.

68. Salvador, P., Hole diffusion length in n-TiO_2 single crystals and sintered electrodes: Photoelectrochemical determination and comparative analysis. *J. Appl. Phys.* **1984,** 55, (8), 2977-2985.

69. Sathish, M.; Viswanathan, B.; Viswanath, R. P.; Gopinath, C. S., Synthesis, Characterization, Electronic Structure, and Photocatalytic Activity of Nitrogen-Doped TiO_2 Nanocatalyst. *Chem. Mater.* **2005,** 17, (25), 6349-6353.

70. Serpone, N., Is the Band Gap of Pristine TiO_2 Narrowed by Anion- and Cation-Doping of Titanium Dioxide in Second-Generation Photocatalysts? *J. Phys. Chem. B* **2006,** 110, (48), 24287-24293.

71. Shannon, R. D., Revised effective ionic-radii and systematic studies of interatomic distances in halides and chalcogenides. *Acta Crystallographica Section A* **1976,** 32, 751-767.

72. Shao, F.; Sun, J.; Gao, L.; Yang, S.; Luo, J., Template-Free Synthesis of Hierarchical TiO_2 Structures and Their Application in Dye-Sensitized Solar Cells. *ACS Appl. Mater. Interfaces* **2011,** 3, (6), 2148-2153.

73. Takahashi, I.; Payne, D. J.; Palgrave, R. G.; Egdell, R. G., High resolution X-ray photoemission study of nitrogen doped TiO_2 rutile single crystals. *Chem. Phys. Lett.* **2008,** 454, (4-6), 314-317.

74. Tang, J.; Cowan, A. J.; Durrant, J. R.; Klug, D. R., Mechanism of O_2 Production from Water Splitting: Nature of Charge Carriers in Nitrogen Doped Nanocrystalline TiO_2 Films and Factors Limiting O_2 Production. *J. Phys. Chem. C* **2011,** 115, (7), 3143-3150.

75. Teleki, A.; Pratsinis, S. E., Blue nano titania made in diffusion flames. *PCCP* **2009,** 11, (19), 3742-3747.

76. Torres, G. R.; Lindgren, T.; Lu, J.; Granqvist, C. G.; Lindquist, S. E., Photoelectrochemical study of nitrogen-doped titanium dioxide for water oxidation. *J. Phys. Chem. B* **2004,** 108, (19), 5995-6003.

77. Umebayashi, T.; Yamaki, T.; Itoh, H.; Asai, K., Band gap narrowing of titanium dioxide by sulfur doping. *Appl. Phys. Lett.* **2002,** 81, (3), 454-456.

78. Umebayashi, T.; Yamaki, T.; Itoh, H.; Asai, K., Analysis of electronic structures of 3d transition metal-doped TiO_2 based on band calculations. *J. Phys. Chem. Solids* **2002,** 63, (10), 1909-1920.

79. van de Krol, R.; Liang, Y. Q.; Schoonman, J., Solar hydrogen production with nanostructured metal oxides. *J. Mater. Chem.* **2008,** 18, (20), 2311-2320.

80. Wang, G.; Wang, H.; Ling, Y.; Tang, Y.; Yang, X.; Fitzmorris, R. C.; Wang, C.; Zhang, J. Z.; Li, Y., Hydrogen-Treated TiO_2 Nanowire Arrays for Photoelectrochemical Water Splitting. *Nano Lett.* **2011,** 11, (7), 3026-3033.

81. Wang, J.; Tafen, D. N.; Lewis, J. P.; Hong, Z.; Manivannan, A.; Zhi, M.; Li, M.; Wu, N., Origin of Photocatalytic Activity of Nitrogen-Doped TiO_2 Nanobelts. *J. Am. Chem. Soc.* **2009,** 131, (34), 12290-12297.

82. Wang, W.; Lu, C.; Ni, Y.; Su, M.; Huang, W.; Xu, Z., Preparation and characterization of visible-light-driven N-F-Ta tri-doped TiO_2 photocatalysts. *Appl. Surf. Sci.* **2012,** 258, (22), 8696-8703.

83. Williams, G.; Seger, B.; Kamat, P. V., TiO_2-Graphene Nanocomposites. UV-Assisted Photocatalytic Reduction of Graphene Oxide. *ACS Nano* **2008,** 2, (7), 1487-1491.

84. Xu, M.; Da, P.; Wu, H.; Zhao, D.; Zheng, G., Controlled Sn-Doping in TiO_2 Nanowire Photoanodes with Enhanced Photoelectrochemical Conversion. *Nano Lett.* **2012,** 12, (3), 1503–1508.

85. Ye, H.; Park, H. S.; Bard, A. J., Screening of Electrocatalysts for Photoelectrochemical Water Oxidation on W-Doped $BiVO_4$ Photocatalysts by Scanning Electrochemical Microscopy. *J. Phys. Chem. C* **2011,** 115, (25), 12464-12470.

86. Yin, W.-J.; Tang, H.; Wei, S.-H.; Al-Jassim, M. M.; Turner, J.; Yan, Y., Band structure engineering of semiconductors for enhanced photoelectrochemical water splitting: The case of TiO_2. *Phys. Rev. B* **2010,** 82, (4), 045106.

87. Zhu, W.; Qiu, X.; Iancu, V.; Chen, X.-Q.; Pan, H.; Wang, W.; Dimitrijevic, N. M.; Rajh, T.; Meyer, H. M.; Paranthaman, M. P.; Stocks, G. M.; Weitering, H. H.; Gu, B.; Eres, G.; Zhang, Z., Band Gap Narrowing of Titanium Oxide Semiconductors by Noncompensated Anion-Cation Codoping for Enhanced Visible-Light Photoactivity. *Phys. Rev. Lett.* **2009,** 103, (22), 226401.

Vita

Son Thanh Hoang was born in Bac Giang, Vietnam. In 2001, he graduated from HUS High School for Gifted Students in Chemistry in Hanoi, Vietnam, and enrolled in the Honor Program for Talented Students at the Hanoi University of Science (HUS) with a major in Chemistry. While attending HUS, Son conducted undergraduate research under the guidance of Professor Ha Cao The. Son finished his undergraduate work and was awarded his Bachelor of Science degree in Chemistry in May 2005. In 2007, Son received Vietnam Education Foundation's fellowship and enrolled in the Chemical Engineering doctoral program at the University of Texas at Austin where he began his graduate research under the guidance of Professor C. Buddie Mullins.

Email address: hson83@gmail.com

This dissertation was typed by the author.